2015

Large Eddy Simulations with a Tabulated Conditional Moment Closure Moment Closure Model for Turbulent Premixed Combustion with Heat Loss

Carlos Velez
University of Central Florida

LARGE EDDY SIMULATIONS WITH A TABULATED CONDITIONAL MOMENT CLOSURE MODEL FOR TURBULENT PREMIXED COMBUSTION WITH HEATLOSS

by

CARLOS ALBERTO VELEZ BUSTO
M.S. University of Central Florida, 2011
B.S. University of Central Florida, 2010

A dissertation submitted in partial fulfilment of the requirements
for the degree of Doctor of Philosophy
in the Department of Mechanical and Aerospace Engineering
in the College of Engineering and Computer Science
at the University of Central Florida
Orlando, Florida

Summer Term
2015

Major Professor: Subith Vasu

ABSTRACT

The Tabulated Premixed Conditional Moment Closure (T-PCMC) method has been shown to provide the capability to predict turbulent, premixed methane flames with detailed chemistry and reasonable run times in a RANS/URANS adiabatic environment [39]. Here the premixed T-PCMC method is extended in a Large Eddy Simulation (LES) framework for non-adiabatic premixed flames, allowing heat loss to occur in the mixture before, during and after combustion. It is proposed that the LES framework is a more suitable representation for both chemical and turbulent scales in premixed combustion [47]. By resolving the high energy turbulent scales and modeling the small scale turbulence, it is expected that the resolution of the turbulence and transient effects are better captured in a LES framework leading to better predictions of the mixing rate and consequently the reaction rate, which is the main focus and source of error in combustion modeling [69]. The LES T-PCMC model is implemented using the open source CFD software OpenFOAM [68] for its open access to C++ source code and large library of turbulence and thermo-physical models. The proposed model validated with PIV and Raman measurements of a turbulent, enclosed reacting flame of a single jet [35] and backward facing step geometry [24]. The DLR data sets provide both unity (E.g.Methane) and non-unity (E.g. Hydrogen) Lewis number fuels, allowing for the proposed numerical model to be validated against both unity and non-unity Lewis # flames. Velocity, temperature and major/minor species are compared to the experimental data. Once validated, this model is intended to be useful for designing lean premixed combustors for gas turbines which operate primarily in the corrugated premixed combustion regime [38], where chemical and turbulent time scales are of the same order requiring adequate models for their interaction. LES results with heat loss match the experimental data better than the adiabatic Reynolds Averaged Navier Stokes (RANS/URANS) solution [39] and is able to better resolve the transient features of the flame with an increase in run time of only 50%, when compared to URANS.

ACKNOWLEDGMENTS

I would like to express my sincere gratitude for the help and guidance offered to me by my technical advisors and committee members. I would especially like to thank Dr. Scott Martin for his invaluable insight and experience that he has shared with me while collaborating on this research work. Long and complex theoretical discussions on turbulent combustion with Dr. Martin were crucial to my success and are a most cherished memory. A special thanks is due to Dr. Subith Vasu for his constant push, motivation and experiences that he has shared with me, which truly involved me in the gas turbine industry. I would like to thank Dr. Aleksander Jemcov for his technical discussions and educational support. Thanks are due to Dr. Marcel Ilie, who introduced me to OpenFOAM and turbulence modeling.

The McKnight graduate fellowship along with the Department of Mechanical and Aerospace Engineering are acknowledged for providing financial support through graduate teaching and research assistantships.

Endless gratitude is deserved to my family, friends, colleagues, professors and loved ones. In particular I would like to thank my parents for their endless support and guidance in both successful and unsuccessful times.

TABLE OF CONTENTS

LIST OF FIGURES

CHAPTER 1: INTRODUCTION

Mankind's desire to harness and store energy dates back to the beginning of history. Through all of this time, combustion has been the main source of energy generation. From its elementary start in fire pits, fueled by wood, man-made combustion has evolved to the use of richer and stronger fuels. Higher energy fuels have lead to larger capacity systems to extract the chemical energy from combustion. One of the largest, most used, and portable fuel powered engines are gas turbine engines (GTE). The GTE works by mixing the fuel and oxidizer, under high pressure, igniting the mixture under ideal conditions and harnessing the exhaust energy by means of a multi-stage turbine. Rapid development of GTE systems in industry has played a large part in an industrial revolution which accelerated transportation, fossil fuel and energy technology to the current state of the art. Unfortunately, fossil fuels are not a renewable energy source and have a negative impact on the environment due to major products from the combustion process such as carbon dioxide (CO_2) and water (H_2O), better known as greenhouse gases [70]. It is theorized that these gases trap the thermal energy in the earth's atmosphere and effectively increase the global temperature of the earth. Other products, of fossil fuels, such as sulfur dioxide (S02) and Nitric Oxides (NOx) can mix in the upper layer of the atmosphere and return to the ground in the form of acid rain, which is hazardous to all organic matter [36]. To combat these negative effects legislation has been implemented by several governments to minimize the environmental impact of ground based GTE. The most recent legislation, the 1990 amendment to the US Clean Air Act forced ground based GTE manufacturers to use Lean Pre$-$Mixed (LPM) combustion systems to satisfy the more stringent exhaust emission levels [1]. LPM fuels are more efficient and produce less emissions by simply premixing the fuel uniformly with the oxidizer before ignition. This uniform mixture produces a more efficient combustion process with less radicals in the products due to a more complete combustion of the fuel when compared to traditional non-premixed systems, which mix the oxidizer and fuel during the ignition process. LPM fuels have the potential to satisfy the environmental demands without compromising efficiency by reducing peak combustion temperature [2]. How-

ever LPM flames are sensitive to flame oscillations and extinction issues, which require a much narrower range of stable combustion when compared to non-premixed combustors. These stability problems result in combustion, thermal and acoustic problems such as thermal acoustics, flashback and blow off of the flame [2]. Before addressing these design issues a better understanding of the combustion process and interaction with the fluid dynamics is needed. To resolve these physical phenomenon and help reduce the experimental costs, numerical modeling of turbulent premixed flames has become more important in the past two decades [47].

Computational Fluid Dynamics (CFD) is identified as the main tool, coupled with combustion models, to predict the behavior of turbulent flames. Although research in the modeling of turbulent flames began over 50 years ago, a precise and robust theoretical description of turbulent flames has not been reached. This is due to the complexity of the subject [42] which must be well resolved if used rigorously by industry in the design of combustion chambers. LPM turbulent flames are considerably more challenging to model due the strong interactions between the turbulence and chemical reactions. Depending on the combustion regime the length scales for turbulence and combustion may be of the same order, generally chemical timescales are lower than those of turbulence. Although the prediction of the turbulent scales is well established, a combustion process has a range of length and time scales (due to multiple species in the flame) which must be determined over all reaction rates. In premixed flames both time and length scales are generally of the same order of magnitude and the interaction between combustion and fluid must be accounted for, this is the main challenge in the modeling of premixed turbulent flames. Models which address these fluid/combustion interactions can more accurately predict the emissions in order to design, through CFD, the next generation of LPM combustors. This requirement encourages the research in modeling of LPM turbulent flames.

Turbulent flows (independent of combustion) are simulated using three general methods [48, 51]; direct numeric simulation (DNS), large-eddy simulation (LES), and unsteady/steady Reynolds Averaged Navier Stokes Simulation (URANS/RANS). DNS resolves (without modeling) all of the

turbulent length and time scales. To do this requires a mesh size which can capture even the smallest length scales which are influential; this length is known as the Kolmogorov Scale (KS). Since the smallest cells must have a width comparable to the KS, the computational demands for industrial flows are unrealistic and too costly for DNS solutions. LES splits the length and time scales by resolving the large scale turbulent eddies and modeling the effect of the small scale turbulence [66, 44]. In effect, the required mesh size and computational cost is reduced significantly with little loss in accuracy for a large range of Reynolds number. In LES the small scale turbulence is modeled within a sub-grid scale (SGS); the same scale at which chemical reactions and scalar dissipation occur! This requires suitable SGS models for both the fluid and combustion turbulent fluctuations; a matter which has yet to be resolved.

In RANS or URANS both the large and small scale turbulent fluctuations are modeled and the entire flow field is time averaged. In the case of URANS a local averaging is used on the flow field. RANS/URANS is the least computationally expensive of the three options and accordingly the least accurate for highly time dependent flows, such as those seen in turbulent flame structures and non-aerodynamic shapes. Flames are inherently unstable and require the flow field to stabilize the flame structure. In experiments and industrial combustion chambers sudden expansion of the combustion chamber is used to create a three dimensional re-circulation zone. This re-circulation zone performs two tasks. The large vorticies within the re-circulation region stabilize the flame and help transfer the fluid momentum in the desired direction. Secondly, vorticies which shed off the flame tip help to recirculate the hot gas back upstream towards the ignition area producing a higher temperature at the inlet of the combustion chamber [47]. This is a desirable design feature, which is not optimized due to the numerical challenges present in predicting the interaction between the re-circulation zone turbulent fluctuations and the scalar transport of burnt and unburnt species. Correct modeling of the transient behavior of the scalar transport is vital in the prediction of emissions, for this reason time averaged techniques (URANS/RANS) are considered inadequate since the transient information is lost producing a dissipative solution.

With regards to turbulent combustion modeling, the largest hurdle is providing closure for the mean reaction rate of each species ($\dot{\omega}_i$) [2]. This reaction rate acts as the source term in the species transport equation which must be solved for ns species, where ns is the number of species in the mixture. The reaction rate is a non-linear function of temperature and species concentration, thus averaging the reaction rate based on mean values of temperature and scalar concentrations is proven to be inadequate [69]. The most common closure for such a problem in premixed flame is the use of flamelet based methods which consider the flame to be constructed by various layers of laminar flames. This is an acceptable approximation for thin flames in which the flame scales are much smaller than the turbulent scales, effectively decoupling the fluid-combustion interactions. Once the scales of combustion and turbulence are of the same order of magnitude the assumption becomes invalid as small turbulent eddies will influence the scalar transport. This interaction between turbulence and combustion must be adequately captured to accurately predict the species or emissions of a combustion process such as NOx and NO. Alternative closures have been developed such as the conditional moment closure (CMC), G Equation, and transported probability density function (T-PDF). These methods are described in detail in the background section with emphasis on the CMC model which is employed in this research work. The CMC model has been successfully developed for various non-premixed combustion systems such as bagasse-fired boiler, hood fires [18], bluff-body stabilized , spray auto-ignition [71] and soot formation [72]. Its application, for both RANS and LES, with premixed flames is not fully tested and validated.

The outline of this research proposal is as follows. A literature review of premixed combustion models is performed and detailed. Then the conditional moment closure model (model of choice) is presented and past work described. Implementation and results are documented and analyzed before concluding with the completed research objectives, publications and time line.

CHAPTER 2: BACKGROUND

This chapter provides a comprehensive overview of turbulent premixed combustion modeling that appears in the previous literature [5, 6, 43, 67]. First, a background of the characteristic physics associated with premixed flames and combustion is presented to analyze the participating variables and physical phenomenon which must be modeled or resolved in any premixed combustion model.

In comparison to non−premixed or diffusion flames, in premixed flames the oxidizer and fuel are homogeneously mixed to desired proportions before being ignited to initiate the combustion. This homogeneous mixture provides higher flame temperatures, thinner flames and strong exothermic reactions. Except, if the mixture is lean ($\phi < 1$) premixed combustion can be sustained at lower peak temperatures then those of non-premixed combustion. Exothermic reactions discharge energy in the local vicinity of the flame front which spreads downstream consuming the reactant mixture with a flame propagation speed (S_l^o). Premixed laminar flames produce thinner flame fronts which separate the burnt and unburnt gases, this thickness (δ_l^0) is in the order of 0.1 to 1 mm [2]. To illustrate the differences in reactions across a flame front, figures 2.1 and 2.2 show the behavior of the fuel, oxidizer and temperature across the flame front for a typical non−premixed and premixed flame.

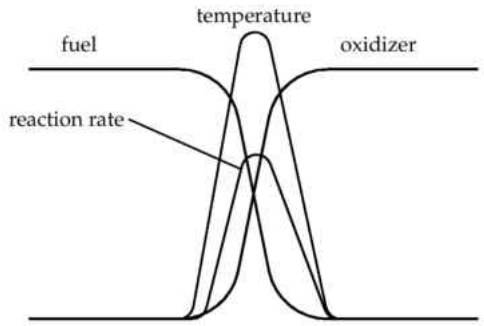

Figure 2.1: Structure of a laminar non-premixed flame

It can be seen that in premixed flames, the oxidizer, fuel and temperature change locally before the flame front or reaction zone. Since the mixture is well mixed, information of the ignition travels upstream altering these values before and during the reaction. Such ”mixing information” can be propagated through laminar diffusion or large eddies created by the combustion process.

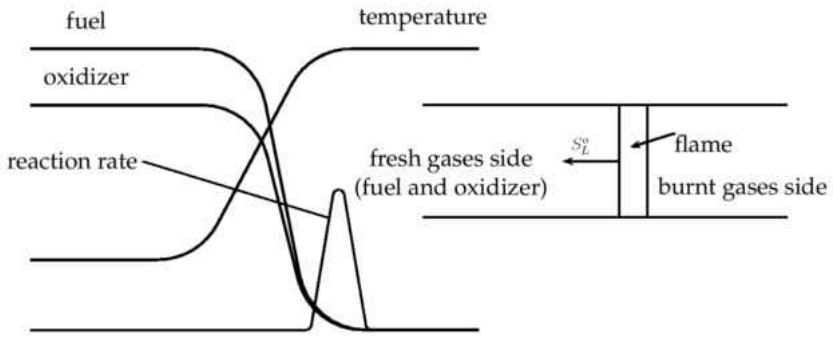

Figure 2.2: Structure of a laminar premixed flame

In the case of non−premixed combustion, the temperature, fuel and oxidizer change only within the reaction zone and enter/exit the reaction zone close to their respective unburnt and burnt values. It is worth noting that in many practical combustion devices the fuel occurs in a mixed or partially−premixed state showing characteristics of both premixed or non−premixed flames.

In many industrial applications mixing is important to sustain combustion or improve mixing of reactants and the oxizer. At these mixing rates the effects of turbulence on the reaction and species

transport are strong and can not be negated. Small and large scale turbulent eddies effectively wrinkle the flame front. By wrinkling the flame front, the flame may fall into itself and allow for partially unburnt products to enter the reaction zone to complete combustion. This recursive combustion is highly desirable for industrial applications because stable flames may be sustained at high mass flow rates since the intense mixing allows for more opportunities for the mixture to react within the given combustion chamber residence time. It will be shown that the effect of small or large scale eddies are more prominent in different combustion regimes. If the chemical reaction time or chemical time scale (τ_c) is order of magnitude lower then those of turbulence then turbulence can not effect the reaction rate. In many cases the flame front is sufficiently wide that small scale turbulent eddies can be engulfed within the flame and alter the flame structure.

In all premixed turbulent combustion models, the interaction between turbulence and chemistry must be adequately resolved or modeled. This has been the focus of past work in turbulent premixed modeling which will be detailed in the rest of this chapter. The background (chapter 2) is prepared as follows. Starting with the governing equations for fluid flow and the scalars associated with combustion. The three CFD paradigms are then briefly described and the advantages and disadvantages of each methodology emphasized. Since LES is used in this research work, section 2.2.3 will describe in detail the modeling assumptions and representation of the ns equations in the LES context. Lastly, in section 2.3, the literature review of turbulent premixed combustion modeling is discussed in detail and the existing models are concisely described.

2.1 Governing Equations

The fluid flow equations consist of the conservation of mass, momentum, energy and species mass fractions which define the reacting system with N species and I reactions [67]. These equations are listed below with a term by term physical description and modeling requirements. All

listed equations are discretized respectively in a Eulerian type control volume.

- Conservation of Mass

$$\frac{\partial \rho}{\partial t} + \frac{\partial \rho u_i}{\partial x_i} = 0 \tag{2.1}$$

The first term in Eq. 2.1 represents the temporal changes in density, followed by the second term which represents the convective transport of mass. For incompressible or steady state flow conditions the first term is negligible.

- Conservation of Momentum

The conservation of momentum states that the fluid acceleration through a control volume is equal to the sum of external forces acting on the boundaries of the control volume.

$$\frac{\partial \rho u_i}{\partial t} + \frac{\partial \rho u_i u_j}{\partial x_j} = -\frac{\partial p}{\partial x_i} + \frac{\partial \tau_{ij}}{\partial x_j} + F_i \tag{2.2}$$

The first two terms on the LHS of Eq 2.2 are the unsteady and convective terms of momentum, respectively. On the RHS, the first and last terms come from changes in momentum by pressure gradients and body forces. The second term on the RHS is the viscous force, where τ_{ij} is written as,

$$\tau_{ij} = \mu_t \Big(\frac{\partial u_i}{\partial x_j} + \frac{\partial u_j}{\partial x_i} \Big) - \frac{2}{3} \mu_t \frac{\partial u_k}{\partial x_k} \delta_{ij}, \tag{2.3}$$

where μ is the dynamic viscosity [Pa-s] and δ_{ij} is the Kronecker delta which is equal to one when $i = j$ and is zero when $i \neq j$. Where i, j and k are the x, y and z spatial components of the viscous stress tensor.

- Conservation of Energy

The total energy is represented by the enthalpy of the mixture. The enthalpy of a reactive mixture is the sum of the specific enthalpies, h_i, of all the species i in the mixture times their mass fraction

(Y_i).

$$h = \sum_{i=1}^{n} sY_i h_i \tag{2.4}$$

The total enthalpy, h_i, is equal to the sum of the enthalpies of formation, h°_{fi}, of species i and the sensible enthalpy, h^s_i. Such that,

$$h_i = h^{\circ}_{f,i} + h^s_i. \tag{2.5}$$

Where the sensible enthalpy is equal to the integral of specific heat at constant pressure with respect to a change in temperature.

$$h^s_i = \int_{T_{ref}}^{T} C_{p_i}(T)\,\mathrm{d}T \tag{2.6}$$

In assuming a low Mach number flow, the compressibility effects are small and a simplified form of the enthalpy conservation equation can be written as

$$\frac{\partial(\rho h)}{\partial t} + \frac{\partial(\rho u_i h)}{\partial x_i} = -\frac{\partial p}{\partial t} + \frac{\partial}{\partial x_i}\Big(\frac{\lambda}{C_p}\frac{\partial h}{\partial x_i}\Big) + S_R. \tag{2.7}$$

The LHS represents the temporal and convective flux of the enthalpy. The first term on the RHS of Eq 2.7 is the contribution to enthalpy by means of a pressure gradient. The second term on the RHS is the diffusion of enthalpy, assuming that the diffusion is represented by a gradient approximation (Fick's Law), this can be thought of as the conduction heat transfer, with the fluid as a still medium. λ is the specific thermal conductivity of the gas, defined as $\lambda = k/\rho$, and acts as the thermal diffusivity ($D_h = \dfrac{\lambda}{C_p} = i$) when divided by C_p. The last term S_R on the RHS is the source term which is used to represent the effect of radiative heat exchange or heat loss to the environment.

- Conservation of Mass Fraction of Species i

$$\frac{\partial(\rho Y_i)}{\partial t} + \frac{\partial \rho u_i Y_i}{\partial x_i} = -\frac{\partial J^i_i}{\partial x_i} + \dot{\omega}_i \qquad (i = 1, 2, ..., N) \tag{2.8}$$

The first two terms on the RHS of Eq 2.8 represent the temporal and convective changes in the

species mass fraction. On the RHS, the first term represents molecular diffusion of species i in the ith direction. The diffusion flux is represented by Fick's law as

$$\frac{\partial J_i^i}{\partial x_i} = -\frac{\partial}{\partial x_i}\Big(\rho D_i \frac{\partial Y_i}{\partial x_i}\Big) = -\frac{\partial}{\partial x_i}\Big(\frac{\mu}{Sc_i}\frac{\partial Y_i}{\partial x_i}\Big), \tag{2.9}$$

where D_i is the molecular diffusivity for each species i and Sc_i is the Schmidt number of species i.

- State Equation

The state equation, also known as the Ideal Gas Law (IGL), is used to find the pressure, p. The IGL is a theoretical gas which behaves with the following relation.

$$P = \frac{Z\rho\Re T}{m}\sum_{i=1}^{n}\frac{Y_a}{W_a} \tag{2.10}$$

In Eq. 2.10 ρ is the density, $\Re$ is the universal gas constant, T is the temperature, m the mass, and Z is the compressibility factor which accounts for the effects of compressibility in the fluid. The mass fraction is obtained through the ratio of the fluids mass, Y_a, and its molar mass, W_a. In the majority of methods an additional equation is solved for the reaction progress variable (RPV). This equation is presented next and its relation to premixed combustion modeling.

- Reaction Progress Variable

The RPV, c, is used often in turbulent premixed combustion models to measure the progress of the reaction from the unburnt (c=0) to burnt (c=1) state. Thus, any ratio of burnt/unburnt quantities, such as temperature

$$c = \frac{T - T_u}{T_b - T_u} \tag{2.11}$$

can be used to define the progress variable. If Lewis number is equal to unity then the ratio of thermal diffusivity is equal to that of mass diffusivity, allowing temperature to be replaced with mass fraction in Eq. 2.11. The subscripts u and b signify the unburnt and burnt state. Alternatively,

the sensible enthalpy can be used in the definition of c [38]:

$$c = \frac{(h^s - 2h) - (h^s_u - 2h_u)}{h^s_e - h^s_u - 2h_e + 2h_u}, \tag{2.12}$$

where h^s is the sensible enthalpy and h is the total enthalpy. Although the definition of c is somewhat arbitrary, Eq. 2.12 is chosen to represent c in this work. The subscript e represents the exit conditions, note that for adiabatic flames these two terms cancel out leaving solely sensible enthalpy as the dependent variable of the RPV (c). This form of c was chosen since the representation of c has useful characteristics for modeling the combustion process with heat loss. c is a monotonically increasing function allowing for values of c greater then unity. This regime, $c > 1$, represents the post flame gases where non-adiabatic heat transfer occurs and certain chemical reactions (NO_x) continue to form during cooling. The denominator in Eq. 2.12 is fixed for a given kinetic mechanism and initial conditions. When Eq. 2.12 is substituted into 2.7 and rearranged one arrives at the conservation equation for RPV, also known as the c equation.

$$\frac{\partial(\rho c)}{\partial t} + \frac{\partial \rho u_i c}{\partial x_i} - \frac{\partial}{\partial x_i}\Big(\rho D_c \frac{\partial c}{\partial x_i}\Big) = \rho \dot{\omega}_c \tag{2.13}$$

where,

$$\dot{\omega}_c = \frac{\sum_i^{ns} \dot{\omega}_i h_f}{h_{s,e} - h_{s,u} + 2h_e - 2h_u} \tag{2.14}$$

The terms on the LHS of Eq.2.13 represent the temporal change, convective change and diffusion of the RPV in physical space, x_i, and time, t. The sole term on the RHS is the reaction rate. These terms will be discussed in more detail in section 2.3. The RPV (c) is used in table look up methods as the primary index to the table which stores the kinematic information from the reaction. These models assume that the majority of scalar fluctuations are representable by the fluctuations in RPV. The fluctuations away from the RPV are modeled by use of a variance equation for the RPV and the scalar dissipation, these will be discussed in detail in sections 2.4 and 2.2.3. The variance is performed on a filtered transport equation of c and requires sub-grid scale modeling for the terms

which appear after Favre averaging the conservation equation of c and computing its variance. The interaction between the RPV and its variance plays an important role in the modeling of scalar fluctuations and will be described in detail in section 2.4. Ultimately, the RPV and other conserved transport equations are solved and the resulting values from the solution are used to index the look up table at every cell in the fluid domain.

2.1.1 Reaction Rates

Correct representation of the total reaction rate of a reacting mixture is difficult in that it depends on a high number of species (ns) mass fractions, turbulent scalar dissipation effects, temperature, pressure, and density and is non-linear in its relations. For this reason, the reaction rate has been the focus of numerical modeling efforts . To introduce reaction rate models a brief overview of the fundamental form of the reaction rate is presented. Considering a set of I elementary reactions, which are represented symbolically in the following form.

$$\sum_{i=1}^{N} \nu_i' M_i \approx \sum_{i=1}^{N} \nu_i'' M_i \tag{2.15}$$

The $\approx$ is exactly $=$ when the reaction reaches a chemical equilibrium. Then one can define the net rate of chemical reaction ,k, as

$$\dot{\omega}_k = k_{fk} \prod_{i=1}^{N} \left(\frac{\rho Y_i}{W_i}\right)^{\nu_{ik}'} - k_{bk} \prod_{i=1}^{N} \left(\frac{\rho Y_i}{W_i}\right)^{\nu_{ik}''}, \tag{2.16}$$

where k_{fk} and k_{bk} are the forward and backward rate coefficients and W_i is the molecular weight of species i. The exponents ν_{ik}' and ν_{ik}'' represent the forward and backward stoichiometric coefficients respectively. In order to resolve the forward and backward stoichiometric coefficients, they are represented by Arrhenius form as

$$k = AT^n exp(-E_a/RT), \tag{2.17}$$

where A is the pre-exponential factor and E_a is the activation energy required to initiate the chemical reaction for species i. Now one can write the chemical reaction rate, on a mass basis, for species i as

$$\dot{\omega}_i = W_i \sum_{k=1}^{I} \dot{\omega}_k (\nu_i'' - \nu_i'). \tag{2.18}$$

2.2 Turbulent Simulation Paradigms

In the simulation of turbulent premixed flames, the above conservation equations can be solved in three different fashions depending on the turbulence modeling methodology used. Depending on the method, certain terms in the conservation equations will be modeled or resolved depending on their turbulent length and time scales. As noted in the introduction, the three methods used commonly are DNS, LES and RANS/URANS turbulence models. The key characteristics, advantages and disadvantages of these methodologies are briefly discussed below. More detail is given to the LES methodology since this is the adopted turbulence model for this research.

2.2.1 DNS

In DNS, each term in the N-S equations is solved without the use of any turbulence models for unclosed or second moment terms (i.e $\overline{a''b''}$). In order to resolve all of the temporal and spatial scales the grid size must be of the same order as the spatial and temporal length scales. The integral length scale, Λ, and the Kolmogorov length, η_k, were derived by Kolmogorov [66] as requirements for DNS, symbolically written as

$$L = N \triangle x \geq \Lambda \quad and \quad \triangle x = \frac{L}{N} \geq \eta_k \tag{2.19}$$

, where L is the domain size, $\triangle$ x is the grid spacing and N is the number of grid points required in each direction of the control volume. The turbulent Reynolds number is related to the turbulent

length scales by

$$Re_t^{3/4} = \frac{\Lambda}{\eta_k}. \tag{2.20}$$

Therefore the maximum number of grid points used in DNS simulation must obey the condition that $N > Re_t^{3/4}$. This shows how expensive DNS simulation are, since most realistic reactive flows occur at Reynolds number of order 10^6 then the grid size must be of order 31,000 in each dimension! The computational costs increase additionally when considering reacting flow, since the chemical reactions of each species introduce their own length and time scales which may be greater, equal to or less then the turbulence scales. Usually, DNS of turbulent combustion is simplified by a single global chemical reaction or limited sets of global reactions, this is done to reduce the computational cost. Normally the chemical scales are smaller requiring even higher resolution from the DNS grid to fully resolve. Consequently, the majority of DNS usage is in laboratory experiments for research purposes in the study of combustion physics or for flow with low Reynolds number.

2.2.2 RANS/URANS

In RANS/URANS modeling the instantaneous governing equations are first averaged and then solved. Additional unknown terms arise since the governing equations are non-linear. To illustrate the averaging procedure the conservation of mass Eq. 2.1 is decomposed and time averaged. The following decomposition of an instantaneous quantity ϕ is performed to separate the quantity into the mean and fluctuating components.

$$\phi(x,t) = \bar{\phi}(x,t) + \phi'(x,t) \tag{2.21}$$

Decomposing Eq. 2.1 in a similar fashion results in

$$\frac{\partial \bar{\rho}}{\partial t} + \frac{\partial}{\partial x_i}(\overline{\rho u_i} + \overline{\rho' u_i'}) = 0. \tag{2.22}$$

The over bar symbolizes an averaging procedure. It is worth noting, that these averages can be spatial or temporal. Notice in Eq. 2.22 that the averaging produces an additional term $\overline{\rho' u_i'}$, which emanates from the correlations between the velocity and density fluctuations and requires modeling. The same procedure is performed on all of the conservation equations resulting in correlation terms which also require modeling.

2.2.3 LES

LES is considered a compromise between DNS and RANS. In LES only the large scale turbulence is solved and the remaining small scaled turbulence is modeled [**?**, 53, **?**]. In order to separate the scales a filter $\triangle$ is used such that scales of $\triangle x > \triangle$ are resolved. The removed and modeled small scale turbulence exist in the sub-grid scale (SGS). In order to avoid the problems in modeling the correlation terms involving density fluctuations (see Eq. 2.22), Favre or density weight averaging is used for flows with large density gradients, such as those found in combustion. The Favre decomposition is written below as

$$\phi(x,t) = \tilde{\phi}(x,t) + \phi''(x,t), \tag{2.23}$$

where $\tilde{\phi} = \dfrac{\overline{\rho\phi}}{\rho}$ and $\tilde{\rho''} = 0$. Even without the density fluctuation correlation terms new terms arise such as $\widetilde{u_i'' u_j''}$ and $\widetilde{u_i'' Y_i''}$. Applying the Favre averaging to the instantaneous governing equations listed above give.

- Conservation of Mass

$$\frac{\partial \bar{\rho}}{\partial t} + \frac{\partial \bar{\rho}\tilde{u}_i}{\partial x_i} = 0 \tag{2.24}$$

• Conservation of Momentum

$$\frac{\partial \bar{\rho}\tilde{u}_i}{\partial t} + \frac{\partial \bar{\rho}\tilde{u}_i\tilde{u}_j}{\partial x_j} = -\frac{\partial \bar{p}}{\partial x_i} + \frac{\partial}{\partial x_j}(\tau_{ij} - \overline{\rho u_i'' u_j''}) + \bar{F}_i \tag{2.25}$$

where, $\overline{\rho u_i'' u_j''}$ is known as the Reynolds Stress Tensor which requires closure, in LES closure of this term occurs at the sub-grid scale, where $l_{grid} < l_{LES,filter}$. The Reynolds stress is modeled using the turbulent viscosity hypothesis which states the Reynolds stress is proportional to the mean rate of strain [44].

$$\overline{\rho u_i'' u_j''} = -\mu_t\Big(\frac{\partial \tilde{u}_i}{\partial x_j} + \frac{\partial \tilde{u}_j}{\partial x_i} - \frac{2}{3}\frac{\partial \tilde{u}_k}{\partial x_k}\delta_{ij}\Big) + \frac{2}{3}\bar{\rho}\tilde{k}\delta_{ij} \tag{2.26}$$

The turbulent/eddy viscosity μ_t is modeled and many approaches have been proposed in the past. In its simplest form proposed by Prandtl, the eddy viscosity is given by $\mu_t = \bar{\rho} l_{min}^2 |\tilde{S}|$ where $\tilde{S}$ is the mean stress tensor defined by $\tilde{S}_{ij} = \Big(\frac{\partial \tilde{u}_i}{\partial x_j} + \frac{\partial \tilde{u}_j}{\partial x_i}\Big)/2$. A popular approach in RANS/URANS models is to model the eddy viscosity as $\mu_t = \rho C_\mu l_m \tilde{k}^{1/2}$, where k is the turbulent kinetic energy obtained from the solution of its transport equation, l_m is the mixing length and C_μ is a model parameter. In the case of LES, most often the standard Smagorinsky-Lilly model [66] is used where the turbulent viscosity is modeled as,

$$\mu_t = \bar{\rho}(C_s \triangle)^2 ||\tilde{S}_{ij}||, \tag{2.27}$$

where $\triangle$ is the filter width, C_s is the Smagorinksy constant and $||\tilde{S}_{ij}||$ is the Frobenius normal $\sqrt{2\tilde{S}_{ij}\tilde{S}_{ij}}$. The filter width (which defines $\triangle$) is taken as the cubic root of the local grid volume. In more recent development [44], the Smagorinksy constant, C_s, is dynamically calculated to produce local and instantaneous field value of C_s instead of one constant global value for the entire flow

field. This method has shown to improve upon the the original Smagorinsky model and will be used in this research work as the turbulence model of choice.

• Conservation of Energy

Written below is the filtered total enthalpy $[J/kg]$ transport equation, neglecting the temporal changes in pressure.

$$\frac{\partial(\bar{\rho}\tilde{h})}{\partial t} + \frac{\partial(\bar{\rho}\tilde{u}_i\tilde{h})}{\partial x_i} = -\frac{\partial}{\partial x_i}(\widetilde{\bar{\rho}u_i''h''}) + \frac{\partial}{\partial x_i}\Big(\frac{\lambda}{C_p}\frac{\partial\tilde{h}}{\partial x_i}\Big) - \rho W_r. \tag{2.28}$$

W_r is the heat loss due to radiation. The first two terms on the RHS are normally lumped together and represented by a thermal diffusion coefficient such at Eq. 2.28 can be re-written as,

$$\frac{\partial(\bar{\rho}\tilde{h})}{\partial t} + \frac{\partial(\bar{\rho}\tilde{u}_i\tilde{h})}{\partial x_i} = \nabla(\bar{\rho}D_t\nabla h) - \rho W_r. \tag{2.29}$$

The second term on the RHS is the diffusion of enthalpy, assuming that the diffusion is represented by gradient approximation, this can be thought of as conduction heat transfer, with the fluid as a still medium. The diffusion coefficient, D_h, is represented by the ratio of the turbulent viscosity to the turbulent Schmidt number. This is written as $D = \dfrac{\mu_t}{Sc_t}$ or $D = \dfrac{\mu_t}{Pr_t}$ with the use of the Prandtl number (Pr_t) which is interchangeable with the turbulent Schmidt number, for Lewis number of unity. Similarly, the transport equation for sensible enthalpy can be written as

$$\frac{\partial(\bar{\rho}\tilde{h^s})}{\partial t} + \frac{\partial(\bar{\rho}\tilde{u}_i\tilde{h^s})}{\partial x_i} = \nabla(\bar{\rho}D_h\nabla h^s) - \rho W_r - \rho\sum_i \dot{\omega}_i h_{f,i}. \tag{2.30}$$

The last term is included to account for the change in sensible enthalpy by the reaction rate, ω_i,and the heat of formation (for each species), $h_{f,i}$.

• Conservation of Mass Fraction of species i

$$\frac{\partial(\bar{\rho}\tilde{Y_i})}{\partial t} + \frac{\partial\bar{\rho}\tilde{u}_i\tilde{Y_i}}{\partial x_i} = \frac{\partial}{\partial x_i}\Big(\overline{\frac{\mu}{Sc_i}\frac{\partial Y_i}{\partial x_i}} - \overline{\rho u_i'' Y_i''}\Big) + \dot{\omega}_i \qquad (i = 1, 2, ..., N) \tag{2.31}$$

Closures for the mean reaction rate, $\dot{\omega}_i$, is required and discussed later in section 2.4.2. The turbulent flux, $\overline{\rho u_i'' Y_i''}$, is lumped together with the rest of the first term on the RHS and modeled by means of a gradient approximation. The resulting equation with the gradient approximation is written as,

$$\frac{\partial(\bar{\rho}\tilde{Y}_i)}{\partial t} + \frac{\partial \bar{\rho}\tilde{u}_i\tilde{Y}_i}{\partial x_i} = \nabla(\bar{\rho}D_t\nabla Y_i) + \dot{\omega}_i \qquad (i = 1, 2, ..., N) \tag{2.32}$$

• Conservation of Reaction Progress Variable

$$\frac{\partial(\bar{\rho}\tilde{c})}{\partial t} + \frac{\partial(\bar{\rho}\tilde{u}_i\tilde{c})}{\partial x_i} = \frac{\partial}{\partial x_i}\Big(\overline{\rho D_c \frac{\partial c}{\partial x_i}} - \overline{\rho u_i'' c''}\Big) + \frac{\sum^n s_i\dot{\omega}_i h_f, u - ad}{h_{s,e} - h_{s,u} + 2h_e - 2h_u} \tag{2.33}$$

The significance of each term in Eq. 2.33 is the same as Eq 2.13). The main difference is the introduction of $\overline{\rho D_c \frac{\partial c}{\partial x_i}}$ in the diffusion term which represents the turbulent scalar flux and requires modeling. The mean reaction rate, $\dot{\omega}_c$, also requires suitable modeling and is discussed later in section 2.3.

• Conservation of Variance of Reaction Progress Variable

In addition to the governing equation for the RPV, a transport equation for its variance must also be solved. The transport equation for the variance of RPV is derived by subtracting the Favre-averaged c equation from its mean $\tilde{c}$ equation. The fluctuations of ρ and D_c are neglected and the mean molecular transport has been neglected for simplicity, but the molecular diffusivity (D_i) still appears in the dissipation term since $D_i = D_c$ at Lewis number equal to unity. The transport equation for the variance of the RPV (cVar), is written below as

$$\underbrace{\frac{\partial(\bar{\rho}\tilde{c''^2})}{\partial t}}_{cVar1} + \underbrace{\frac{\partial(\bar{\rho}\tilde{u}_i\tilde{c''^2})}{\partial x_i}}_{cVar2} = \frac{\partial}{\partial x_i}\Big(\underbrace{\overline{\rho D_c \frac{\partial c''^2}{\partial x_i}}}_{cVar3} - \Big(\underbrace{\overline{\rho u_i'' c''^2}}_{cVar4}\Big) - \underbrace{2\overline{\rho u_i'' c''}\frac{\partial c}{\partial x_i}}_{cVar5} - \underbrace{2\bar{\rho}\tilde{N}_c}_{cVar6} + \underbrace{2\overline{c''\dot{\omega}_c}}_{cVar7}. \tag{2.34}$$

As usual, the first two terms (cVar1,2) of the LHS of Eq. 2.34 represent the temporal changes and spatial changes of the variance of c by means of convection. Term cVar3 represents the diffusive flux of the variance. Both D_c and $\overline{\rho u_i'' c''^2}$ require modeling. Terms cVar4 and cVar5 both represent the effects of mean and fluctuating strain fields and the interaction of turbulence u_i'' and scalar fields

c''. Usually these two terms are lumped together as both include a second moment term $\overline{a''b''^2}$ which requires modeling, these terms are typically related to the scalar dissipation rate, $\tilde{\epsilon}_c$. Term cVar6 represents the effect of the scalar dissipation rate on the variance. The scalar dissipation rate is given by

$$\bar{\rho}\tilde{N}_c = \overline{\rho D_c\Big(\frac{\partial c}{\partial x_i}\frac{\partial c}{\partial x_i}\Big)}. \tag{2.35}$$

This term is normally modeled by representing the scalar dissipation as the turbulent time scale and its variance, i.e

$$\bar{\rho}\tilde{N}_c = 2C_{c1}\rho\frac{\epsilon}{k}c''^2, \tag{2.36}$$

where Cc1 is a model parameter (usually between 0.9 and 1), ϵ is the dissipation rate of turbulent kinetic energy and k is the turbulent kinetic energy. Note that k and ϵ are computed from the CFD turbulence model and acts as a link between the CMC table and turbulent fluctuations modeled by the CFD. This model for scalar dissipation can be expressed in various other forms, depending on the turbulence model in use, which will be discussed in more detail in section 2.3. Since c is a reactive scalar, the production of variance $\overline{c''^2}$ due to chemical reaction exists and is represented by the last term cVar7 in Eq. 2.34. This term also requires modeling and will be discussed in section 3

• modeling for the Turbulent Scalar Flux $\widetilde{\rho u_i'' c''}$

In order to solve Eq. 2.34 and Eq.2.33, the turbulent scalar flux, $\widetilde{u_i'' c''}$, needs to be modeled. Where u_i'' and c'' are the Favre fluctuation of the velocity vector and progress variable, respectively [**?**, 60]. This term is often modeled using the classical gradient transport hypothesis (GTH), based on the eddy viscosity, [9] as

$$\widetilde{\rho u_i'' c''} = \overline{\rho u_i'' c''} = -\frac{\mu_t}{Sc_c}\frac{\partial \tilde{c}}{\partial x_i}, \tag{2.37}$$

where μ_t is the turbulent eddy viscosity and Sc_c is the turbulent Schmidt number. This hypothesis states that the turbulent flux transport is analogues to molecular transport. This hypothesis

holds true for gradient fluxes but is invalid for counter-gradient fluxes. However, theoretical analysis [10, **?**], experimental [17, **?**] and DNS [12, 13, 60] studies point out the existence of both gradient and counter-gradient fluxes in turbulent premixed flames. The transition from gradient to count-gradient fluxes is dependent on the ratio u'/S_L° and the heat release factor [13], where u' is the root mean square (RMS) of the turbulent velocity fluctuations and S_L° is the laminar flame speed. According the DNS analysis in [13], the transition occurs when the flow field is dominated by thermal expansion caused by heat release, i.e., when the ratio of u'/S_L° is large. A transport equation for the turbulent flux has been derived and analyzed [37] to account for the occurrence of gradient and counter-gradient fluxes. A simple algebraic model has also been proposed in an earlier study [13] to include the gradient and non-gradient scalar flux transports in premixed flames. It is not uncommon to use a gradient flux model in calculations of high Reynolds number and is explicitly valid in adiabatic simulation where there is no heat release.

2.3 Premixed Combustion Models

The main objective of turbulent combustion modeling is to provide closure for the mean reaction rate term, $\bar{\dot{\omega}}_i$, which appears in the species transport equation (Eq. 2.24), c transport equation (Eq. 2.33) and the variance equation (Eq. 2.34). The average reaction rate cannot be easily expressed as a function of averaged mass fraction ($\tilde{Y}_i$), mean density ($\bar{\rho}$) and mean temperature ($\tilde{T}$) since the reaction rate has a non-linear relation to these averaged quantities. Approaches have been proposed in the past and have been discussed in great detail [42]. It is not possible to review all of these approaches here, instead a brief overview of the related turbulent premixed combustion models are reviewed in this section. Before considering established models, a description of the regimes of turbulent premixed combustion is necessary to analyze the reaction rate ($\bar{\dot{\omega}}_i$).

2.3.1 Turbulent Premixed Combustion Regimes

All mean reaction rate models have a statistical relationship with the fluctuating quantities in turbulent flames which are dependent on the structure of the small scales. This encourages the use of LES based SGS models, since URANS/RANS models lose the small scale information due to the averaging procedure. Fundamentally, the models depend on the relativity between the scales of turbulence and that of the flame chemistry. Damkohler identified two limiting scenarios or regimes; flamelet and non-flamelet combustion [49].

In the case of flamelet combustion, the flame chemistry scale (FCS) is much smaller than the turbulent scales and vice-versa for non-flamelet combustion. To describe these two regimes a new set of length and time scales must be defined for the FCS in order to relate to the scales of turbulence. In the case of turbulent time scales, the Kolmogorov length scale, η_k, at a characteristic velocity u'_k of the integral length scale , Λ, at a characteristic velocity u'. Thus, the integral (large scale) time scale ,τ_t, and the Kolmogorov (small scale) time scale , τ_k, are defined respectively as

$$\tau_t = \frac{\Lambda}{u'}, \qquad \tau_k = \frac{\eta_k}{u'_k}. \tag{2.38}$$

In the case of the combustion time scales, the length scale is characterized by the flame front thickness, δ,and flame speed, S_L°. With these two scales the chemical time scale, τ_c, is defined as

$$\tau_c = \frac{\delta}{S_L^\circ} \tag{2.39}$$

The ratio of the integral time scale to the chemical time scale is defined as the Damkoler number

$$D_a = \frac{\tau_t}{\tau_c} = \frac{\Lambda/\delta}{u'/S_L^\circ}. \tag{2.40}$$

With a similar analogy to the small scales, the Karlovitz number is the ratio of chemical time scales

to the small scale turbulence time scale

$$K_a = \frac{\tau_c}{\tau_k} = \frac{\delta^2}{\eta_k^2}. \tag{2.41}$$

Reynolds number is a useful parameter for defining turbulent flow regimes, the turbulence can be written in the form of turbulent and chemical time as shown below.

$$Re = \frac{u'/S_L^\circ}{\delta/\Lambda} \tag{2.42}$$

This form of the Reynolds number assumes $\nu = \delta S_L^\circ$, which has been validated through dimensional analysis of the dependent terms in Eq. 2.42. The physical relationship between these non-dimensional numbers (D_a, K_a, Re) are commonly represented using the combustion regime diagram [38]. This regime diagram is used to classify the various turbulent premixed combustion regimes. A typical combustion regime diagram is shown below in Fig. 2.3 [40].

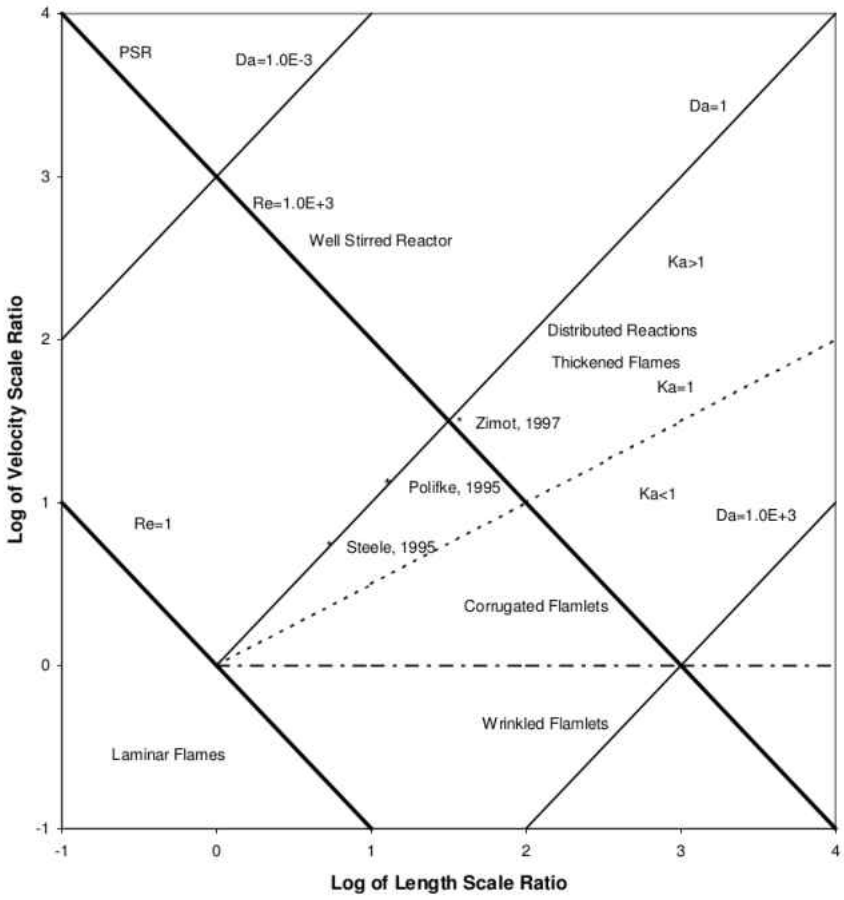

Figure 2.3: Premixed Borghi Diagram

If the thickness of the flame front is smaller then the integral eddies then chemical time scale, τ_c, is faster (smaller) than the integral turbulence time scale. This means the chemical reactions will occur much faster then turbulent fluctuations, which effectively uncouples the interaction between the turbulent and chemical time scales resulting in a laminar flame (called scale separation). Since small scale turbulence can not enter the flame front (due to a difference in scales) the flame front is simply wrinkled by the turbulence effects. This situation is denoted on Fig. 2.3 by $D_a > 1$ and is known as the flamelet combustion regime.

Inversely, as the thickness of the flame front increases past the size of the small scale eddies then the turbulent time scale, τ_t, becomes faster than the chemical time scale, τ_c. This couples the turbulent and chemical effects, since the turbulent (large scale) eddies can penetrate the flame

front the turbulence disturbs the flames internal structure and promotes continuous mixing of the reactants. This regime is known as the perfectly stirred reaction regime and is characterized by $D_a < 1$ The Karlovitz number is used to further subdivide the flamelet regime depending on the role of the small scale eddies. When $K_a > 1$ the turbulent flame scales are smaller then turbulent small scales and effectively the small scales of turbulence do not disturb the internal structure of the flame. This regime is separated by the Klimov-Williams line which signifies a combustion regime where $Ka = 1$ and $\delta = \eta_k$. In the case of $1 < K_a < 100$, the reaction zones of the flamelets are intact but the small eddies disturb the preheat zone which enhances heat and mass transfer in the reaction zone. This combustion regime is known as the thin reaction zone regime. The flamelet hypothesis has become a common approach for turbulent premixed combustion. In the cases of moderate to low mixing rates experimental review has shown evidence that non-flamelet behavior is sparse [23].

Fig. 2.3 labels the different combustion regimes (Laminar Flames, Wrinkled Flamelets, Corrugated Flamlet, Well Stirred Reactor, Thickened Flames, and Distributed Reactions. To demonstrate the state at which combustion of GTE exist, several GT combustor experiments have been labeled by Zimont et al. [73], and Steele [58] performed combustion experiments in the distributed reaction regime where Damkohler number is of order unity and the turbulent Reynolds number ranges from 130 to approximately 2,500. With this in mind, a review is presented of the existing models for turbulent premixed combustion in subsection 2.3.2.

2.3.2 Eddy Break-Up Model

Proposed by Spalding [56] the Eddy Break Up (EBU) model is applicable for flames with high Re and D_a. This model assumes that the reaction zone is described as pockets of unburnt and burnt gases and the turbulent eddies will promote mixing in these pockets. In essence, the EBU model assumes turbulent mixing controls the overall chemistry. Correspondingly, the reaction rate

is given by

$$\bar{\dot{\omega}} = C_{EBU}\bar{\rho}\frac{\sqrt{\tilde{c''^2}}}{\tau_t}, \tag{2.43}$$

where, C_{EBU} is a model constant between 0.1 and 100, and is normally of order unity. τ_t is the turbulent time scale which is defined as $\frac{\tilde{k}}{\tilde{\epsilon}}$ as previously stated. In order to estimate $\tilde{c''^2}$, the assumption of an infinitely thin flame yields $\tilde{c''^2} = \tilde{c}(1-\tilde{c})$. This model introduces the thin flame approximation, a widely used approximation, which assumes that all of the reactions take place in a very thin sheet that is smaller then the Kolmogorov scale η_k. A modified version of this model is the Eddy Dissipation concept (EDC), which uses the mean mass fractions instead of the RMS of the progress variable ($\tilde{c''^2}$), which reduces the computation cost with little loss in accuracy [56]. Based on the literature there is no agreed upon EBU model, but it is acknowledged that in order to allow for the widest range of conditions for flames the EBU model must account for chemical kinetics on top of the mixing effects. Few attempts have been made to include the chemical kinetics and most of the literature uses a 1-step mechanism or use the fast chemistry assumption, i.e. they neglect the chemical kinetics term. Polifke et al. [56] implemented the EBU model with a $k-\epsilon$ turbulence model to predict NO_x formation in a double cone burner. The turbulent Reynolds number was approximately 250, the Damkohler number was unity and the Karlovitz number was greater than 2. A 2-step global oxidation mechanism was used for the kinetics of the methane combustion. For these limited cases good results were achieved, although it was concluded that a more reliable turbulent combustion model would increase the accuracy in NO_x, temperature and CO concentrations. Significant disagreement in temperature and scalar quantities resulted in the vicinity of the flame front, which is expected with a 2-step mechanism.

2.3.3 Bray-Moss-Libby Model

The most generic and simplest flamelet model is the Bray Moss Libby (BML) [14] model, which is an extension of the Bray Moss model [11]. The BML model is based on a statistical approach using the probability density function (PDF) of the progress variable, c, which is zero in

the reactants and unity in the products. In flamelet models, the flow is broken into three distinct zones; the fully burned mixture, the unburned mixture and an infinitely thin flame zone (smaller then Kolmogorov scale) between the two stated limiting values. For the thin flame assumption, the flame zone has no intermediate values of temperature and no volume, which limits the model to fast chemistry, i.e. the flame proceeds instantly from the unburned to fully burned condition. This step from unburnt to burnt is analogous to a Dirac Delta function which takes on a value of zero or one with no intermediate values. For this reason, a PDF is built up of two delta functions, one at $c = 0$ and another at $c = 1$. The PDF is written below in its general form,

$$p(c = \zeta; x, t) = \alpha(x, t)\delta(\zeta) + \beta(x, t)\delta(1 - \zeta) + \gamma(x, t)f(\zeta), \tag{2.44}$$

where ζ is the sample space variable for c and $\alpha + \beta + \gamma = 1$. α and β are weights for each delta function where $c = 0$ or $c = 1$. For high Re and D_a numbers, the flame front is thin and the probability of encountering burning gases is much lower compared to finding unburnt and burnt mixtures. Therefor, since the flame is assumed thin there are no intermediate species and thus the third term is set to zero ($\gamma = 0$). The coefficients α and β are related to the heat release factor, τ, and the progress variable, c, by

$$\alpha = \frac{1 - \tilde{c}}{1 + \tau\tilde{c}}; \qquad \beta = \frac{(1 + \tau)\tilde{c}}{1 + \tau\tilde{c}} \tag{2.45}$$

where $\tau = (\rho_u/\rho_b) - 1$. Thus the PDF shape becomes a function of the gas density and progress variable. Since the burning state of combustion is neglected, an alternative methodology is required to close the mean reaction rate. Bray [8] showed that

$$\bar{\dot{\omega}}_c = 2\frac{\rho\tilde{N}}{2c_m - 1}, \tag{2.46}$$

when the limit of $\gamma \to 0$ and thus the expression $\widetilde{c''^2} = \tilde{c}(1 - \tilde{c})$ can be used. The constant c_m is given by a progress variable averaged reaction rate and is typically equal to 0.7 to 0.8. The scalar

dissipation rate is defined alternatively as Eq. 2.35 or Eq. 2.36.

An alternative approach to close the mean reaction is to analyze the flame crossing frequency. Flame crossing occurs when the flame front crosses over a fixed location in the turbulent flow, the frequency of the flame front crossing this location is found to be correlated to the mean reaction rate. In this method, the mean reaction rate is expressed as the product of the flame crossing frequency, f_c, and the reaction rate per flame crossing, $\dot{\omega}_c$, as

$$\bar{\dot{\omega}}_c = \dot{\omega}_f f_c. \tag{2.47}$$

Here the flame crossing frequency, f_c, can be estimated as

$$f_c = 2\frac{\bar{c}(1-\bar{c})}{\tau_c}, \tag{2.48}$$

where τ_c is the mean period of a telegraphic signal, this signal is chosen to represent the instantaneous c. The turbulent time scale, $\frac{\epsilon}{k}$, is again introduced into the model to determine the period of the telegraphic signal. The reaction rate in Eq. 2.47 is modeled as

$$\dot{\omega}_f = \frac{\rho_u S_L^\circ}{\delta_L^\circ / t_t}, \tag{2.49}$$

where t_t is the transient time and is defined as the time required to cross the flame front [12].

In all flamelet methods, including BML, a conservation equation must be solved for the reaction progress variable (Eq. 2.13). Normally, the species mass fraction equations are transformed to c space and solved independent of the fluid equations. This produces a set of N species conservation equations with c as the independent variable, replacing time and space. This formulation results in

the following conservation equation for the species mass fraction.

$$\rho u_c \frac{\partial Y_i}{\partial c} - \rho \frac{N}{2} \frac{\partial^2 Y_i}{\partial c^2} = \rho \sum_{n=1}^{N} v_{i,n} \omega_n \tag{2.50}$$

where $u_c = \sum_{n=1}^{N} \frac{\nu_{C0_{2,n}\omega n}}{Y_{CO2,ad}}$ and X is the scalar dissipation rate. This form of the conservation equation of c is not described in detail, but is used in sections 2.4.2 and 2.4.3 for comparison.

2.3.4 Flame Surface Density Model

The flame surface density model (FSD) was proposed at first for non-premixed flames and was later developed for premixed flames [63]. This model assumes the flame moves locally as a laminar flame, but the flame front is stretched or wrinkled. This stretching is accounted for by a flame surface density (Σ), which is the flame surface area per unit volume. With this the mean reaction rate can be expressed as

$$\bar{\dot{\omega}} = \rho_u S_l \Sigma. \tag{2.51}$$

Here the S_l is the local laminar flame speed which is the source of the turbulent stretching of the flame front since it included a stretch factor ranging from 0.9 to 1. In the case of LES, the modeled SGS turbulence is used to define the stretch factor dynamically based on the assumption that turbulent motions are in equilibrium with flame dynamics. This is a valid assumption in the case that the flame is fully developed and passed the early stages of the flame development.

In order to solve for Σ, algebraic expressions have been used and transport equations which require their own suitable closures. The modeling of various terms in the Σ transport equation have been the subject of many studies [42] and the important results have been summarized in the review paper [15].

Although based on laminar assumptions, the calculation of the FSD is a valuable variable. It can be shown that Σ is associated with a specific iso-surface of the progress variable when $c = c^*$.

This is expressed mathematically as

$$\Sigma(c^*, x, t) = \langle |\bar{\nabla} c| | c = c^* \rangle p(c^*, x, t), \tag{2.52}$$

where $\langle |\bar{\nabla} c| c = c^* \rangle$ is the conditional average of $|\bar{\nabla} c|$ for the condition that $c = c^*$ and $p(c^*, x, t)$ is the PDF. Although easy to implement all flamelet models provide limited information about the flame. All of the chemical kinetics information comes from the laminar flame speed and requires a correlation to relate the turbulent flame speed to both the laminar flame speed and turbulent intensity. Moreover, these correlations are experimentally developed and only valid for a limited range of operating conditions.

2.3.5 Probability Density Function

The PDF method makes full use of the PDF by implementation via Monte Carlo methods. In this method the control volume is discretized into a finite number of parcels. Each parcel has an assigned value of c such that the combined parcels act a PDF within each cell. Additionally, the parcels are allowed to perform four actions [50]:

1. They can be convected from upwind cells to downwind cells. The number of parcels transported in a given time depends on the local average velocity.

2. They can be exchanged for other parcels in neighboring cells to represent the turbulent diffusion process. The rate of exchange is based on local turbulence parameters.

3. They can mix with other parcels within the cell. The idea here is that an isolated, non-reacting cell would eventually converge to a uniform composition due to internal mixing. A number of models exist to describe this process. As an example, the Curl model [65] selects two parcels at random, mixes them, and assigns this average mixture composition to the two

cells. The mixing intensity (i.e., frequency of the averaging process) is modeled based on turbulence parameters.

4. They can react. Between the transport-based events described under 1-3, the parcels all undergo reaction as isolated simple batch reactors in parallel.

The first two actions include the transport process which is based on the turbulence models. The mixing law in number 3 uses empirical approaches to model the mixing frequency. The value of the PDF method is that the chemistry described in the 4th item is exact! Moreover, the effect of the fluctuations in temperature and composition on the chemical reactions since the chemistry of each parcel of the PDF is calculated independently. This concept is implemented by solving transport equations for the PDF's of the various species. Due to the behavior of the PDF in c space, direct solutions of these equations is often difficult requiring the Monte Carlo solution procedure until the field variables converge. Due to the numeric difficulties there are several variations of the PDF approach. In the simplest method, a single point PDF uses a 1-step chemical reaction to relate c to mass fractions and enthalpy. The PDF of c, P(c), is defined such that $c(x,t)$ is in the range [50]

$$c - \frac{dc}{2} < c(x,t) < c + \frac{dc}{2}. \tag{2.53}$$

The species and enthalpy equations are then formulated by recasting into a PDF balance equation as follows [50]

$$\frac{\partial}{\partial t}P(c) + \frac{\partial}{\partial x_i}\overline{u_i \delta(c(x,t)-c)} = \frac{\partial}{\partial c}\Big[-\omega(c)P(c)\Big] - \frac{\partial}{\partial c}\Big[\delta(c(x,t)-c)\frac{\partial}{\partial x_i}\Big(D\frac{\partial c}{\partial x_i}\Big)\Big] \tag{2.54}$$

where x_i is the location, u_i is the velocity (in all three components $i = 1, 2, 3$), $\omega(c)$ is the species production term and D is the diffusion coefficient which must be modeled. The four terms in Eq. 2.54 represent the unsteady effect, convection in physical space, convection in PDF space and the flux in the PDF space [50].

Alternatively, a presumed shape can be used for the PDF. The given form (e.g. Gaussian or Beta Function) of the PDF is assumed with constraints on the first and second moments. The exact shape of the PDF is then determined by two parameters (c, c''^2), which is effectively the target of the solution. It is also typical to use a Favre averaged β-function for given values of mean and variance of c. The Favre β-PDF is given by

$$\tilde{p}(\zeta) = \frac{\zeta^{a-1}(1-\zeta)^{b-1}}{\beta(a,b)}, \tag{2.55}$$

where,

$$a = \tilde{c}\Big(\frac{1-\tilde{c}}{\tilde{c}}\Big), b = (1-\tilde{c})\Big(\frac{1-g}{\tilde{c}}\Big), \tag{2.56}$$

$$g = \frac{\tilde{c''^2}}{\tilde{c}(1-\tilde{c})} \tag{2.57}$$

and

$$\beta(a,b) = \int_0^1 \zeta^{a-1}(1-\zeta)^{b-1} d\zeta \tag{2.58}$$

The dependence of the PDF on c and variance is evident in the above expressions, where the values are calculated from their respective transport equations. PDF's are used in the Conditional Moment Closure model to transform values from conditioned space to unconditioned (on c) space and are used in majority of turbulent combustion models. Although the assumed shape makes the PDF transport equation easier to solve, there is a resulting reduction in accuracy. Ideally, the assumed shape method will only exactly work on perfectly premixed and diffusion flames with fast chemistry assumption. To improve upon the model a joint PDF (JPDF) is used to incorporate the probability of more then one variable. There are three common types of joint PDF's; a species PDF as described above but with multiple species. In this type, the PDF has no information of the velocity field and requires the solution of the N-S equations. Additionally, the gradient-diffusion term in equation 2.54 is modeled [63]. The second type of JPDF is the velocity composition PDF. This method includes the three velocity terms in the PDF so that all forms of convection and transport

are treated exactly. The velocity-component PDF only accounts for the large scales so an equation representative of the dissipation of the velocity is additionally solved. The third type of JPDF is the velocity-dissipation-composition PDF. In this case no additional equations are required, but there are numerical difficulties in solving the PDF. This JPDF model assumes the scale of the species are proportional to the scales of the velocity [50]. The reaction, gravity and mean pressure gradient terms are treated exactly, but modeling is required for the fluctuating pressure gradient, molecular stresses and the scalar dissipation rate. Although using a JPDF to model the reactions is an improvement over the methods described in 2.3.3, they have large computational cost.

In [50] a combined velocity-composition JPDF in implemented in the commercial CFD code, FLUENT, with a 5-step kinetics mechanism. The model used a $k - \epsilon$ model in a 2D mesh. The authors reported an over prediction of the turbulent viscosity, severely limiting the model. The JPDF transport equation was solved with the Monte Carlo method. The model was compared to results from a laboratory-scale GT and predicts the correct trends and species concentrations except near the re-circulation zone. In essence, the PDF method is unique in that it offers an exact representation of the reaction rate but still requires a mixing sub-model which is usually related to the turbulence model.

2.3.6 G-Equation Model

The G-Equation model (GEQ), also known as the level set approach, is also based on the thin-flame assumption that chemical reactions occur within the infinitely thin flame front. The flame front separates the uburned and burned mixtures with a "burning" velocity normal to the front S_T.

The GEQ model represents the flame propagation by means of a non-reacting iso-surface of $G(x,t)$. $G(x,t)$ is a three dimensional field which is defined on the 2 dimensional flame surface area. It is defined such that there are no turbulent fluxes normal to the flame front which removes the need for a counter-gradient diffusion model. The GEQ model is novel in that it offers a kine-

matic representation of the flame front. Previously discussed models use a progress variable to determine how much of the mixture is fully burnt, whereas the GEQ calculates the G-field which measures the location of the center of the flame. This iso-surface, $G(x,t)$, acts as a "sheet" over the domain which maps the flame front location by considering an arbitrary iso-scalar value G_0. This value is chosen such that $G > G_0$ represents the burnt mixture and $G < G_0$ represents the unburnt species. The G-field is solved for by means of a transport equation for the mean of $G(x,t)$, written as,

$$\frac{\partial(\bar{\rho}\tilde{G})}{\partial t} + \frac{\partial(\bar{\rho}\tilde{u_i}\tilde{G})}{\partial x_i} = \bar{\rho}S_T \mid \frac{\partial \tilde{G}}{\partial x_i} \mid -\bar{\rho}D_t\kappa \mid \frac{\partial \tilde{G}}{\partial x_i} \mid \tag{2.59}$$

where models are needed for turbulent burning velocity, S_T, diffusion coefficient, D_t, and κ. Similar to the previously discussed models a transport equation for the variance of G, $\tilde{G''^2}$, is solved for. Similarly, a equation is solved for the mean of the absolute gradient of G,$\mid \bar{\nabla G} \mid$. Since the G-field is a non-reacting and kinematic representation of the flame location a customized model is needed to relate the laminar flame speed to the flame displacement speed. Solving these equations, with CFD for the solution of the N-S equations, produces the mean turbulent flame location. Unfortunately, an additional model is required to resolve the laminar flame structure from the turbulent flame structure. Previously discussed models such as the BML or EBU method have been used to achieve this function, although the author brings to attention the inconsistent nature of combining combustion models with different representations of the flame surface. The details of this method are discussed by Peters and BRAY in [14], It was concluded that the G-field formulation is only valid for the corrugated flamelet and thin reaction zone regimes of turbulent premixed combustion. Moreover, since both the G-equation and flamelet models were developed for laminar flame applications, it is doubtful that the combination of such models will be valid for industrial GT applications which operate mostly in the distributed reaction regime.

2.3.7 Summary

All of the above described models can be used in the modeling of turbulent premixed combustion but the difficulty remains in which model is appropriate for the given operating condition. As an example, flamelet models assume a thin flame assumption which is only valid for a small regime of flamelets and neglects the effect of small scale turbulence in the flame structure or internal mixing. If the model seeks to resolve the pollutants and minor species from the reacting mixture then this assumption is fundamentally invalid. Moreover, limited kinematic information is acquired in flamelet models which is a necessity in the prediction of pollutants in combustion. Although the PDF models show considerable improvement in its exact representation of the reaction rate, multiple variables needed in the JPDF's make the method computationally too expensive for rigorous industry use. The PDF approach also requires a model for the micro-mixing which has created variations of the PDF method and is the main source of uncertainty in this formulation. The G-Equation method has some benefits from its kinematic representation of the flow field, but offers no closure for the reaction rates. This requires the use of other premixed combustion models for closure which is inconsistent in the formulation used by each model.

The Conditional Moment Closure Model (CMC) [31, 32] is an alternative approach with good potential to predict emissions due to its detailed chemistry kinematics, generalized form (for all regimes of combustion) and moderate computational cost. This method has been widely used for non-premixed combustion but its development in premixed flames is sparse. The CMC method is chosen for this study and developed in a LES formulation for the prediction of emissions produced in LPM GT. A detailed description of the CMC model is provided in the final section of Chapter 2.

2.4 The Conditional Moment Closure Model

This chapter provides a review of the main features of the CMC. The first section states the fundamental concept and assumptions of the method. The second section briefly describes the

non-premixed CMC method, where as the third and fourth sections focus on the premixed CMC model and sub-models in a URANS and LES context.

2.4.1 CMC Methodology

As discussed in section 2.2 the main difficulty in premixed combustion modeling is the closure of the mean reaction rate. The standard moment method (MM) works under the principle that fluctuations of N scalars can be represented by the fluctuations of a single variable, in this case the reaction progress variable. Conventional moment methods are not applicable for closure since the variance from the mean for mass fraction and temperature is very high making the method inaccurate. However, Bilger in [61], stated that the hypothesis of the moment method can be used if one uses a conditional moment rather than a unconditional moment. A conditional moment calculates the fluctuations of a scalar when a conditioned is met such that $c = \zeta$, where c is the RPV and ζ is the "RPV" in conditional space. This is written symbolically as, $\langle Y_i | c = \zeta \rangle$, where Y_i is the conditioned scalar. Bilger's hypothesis is valid since fluctuations over the conditional mean are small compared to the fluctuations over the unconditional mean. Figure 2.4 from [32] illustrates the validity of the hypothesis showing the large variations of temperature and OH mass fraction over the unconditioned mixture fract on the left side. The right side of figure 2.4 shows how much smaller the variations from the mean of temperature and OH mass fraction are when conditioned in mixture fraction space. It is worth noting that conditioned values also have smaller fluctuations in physical space as well as mixture fraction or RPV space.

Thus, the main hypothesis of the CMC method is that fluctuations of scalar mass fraction and temperature are closely associated to the fluctuation in one or two key scalar quantities. These key scalar quantities are typically the RPV, c, variance, c''^2, enthalpy, h, or the mass fraction of a major species, Y_i.

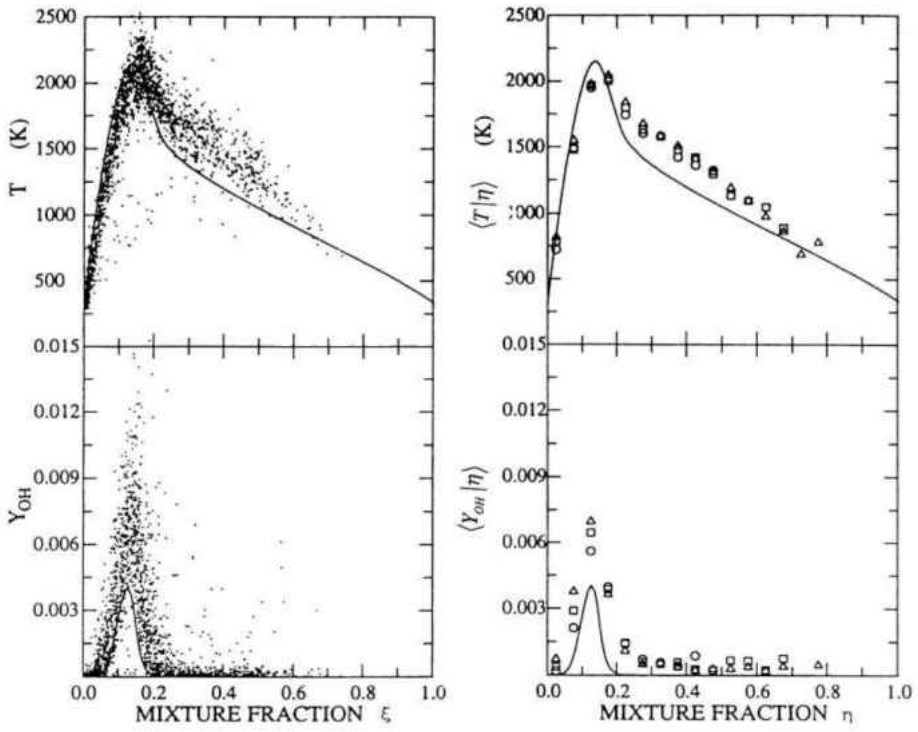

Figure 2.4: Scatter plots of instantaneous and conditional averages for the temperature and OH mass fraction at various downstream locations. The solid line represents the fully burned strained laminar flame result

The CMC method derives transport equations for the conditional averages and solves them along with additional moment equations subject to initial and boundary conditions. The resulting equations are detailed in sections 2.4.2 and 2.4.3. The governing equations are derived by first decomposing a instantaneous scalar value into its conditional mean, Q_i, and the fluctuation around Q_i. This decomposition is performed below on the mass fraction of a scalar i. Where the angled brackets, $\langle\rangle$, denote a conditional averaging subject to the condition on the right of the $|$ symbol.

$$Y_i(x,t) = \langle Y_i | c = \zeta \rangle + Y_i''(x,t) = Q_a(\zeta; x, t) + Y_i''(x,t) \tag{2.60}$$

With the correct choice of conditioning variable (c in this case) the fluctuating term in Eq. 2.60 is reduced. Thus, by increase the dimensionality of problem the fluctuations are reduced and a more accurate prediction of the average species concentrations is obtained. Additional conditioning

variables can be introduced for conditioning for better prediction of species conservation. Multiple variable conditioning is known as the Second Order CMC method which has higher computational costs then first order analysis. [32] Bilger shows that for flames far from extinction second order analysis provides the same results as the first order CMC approximation.

The transport equation for Q_i is derived by employing this decomposition on Eq. 2.8 and then taking the conditional average of the resulting equation, the resulting equation is known as the CMC equation and is discussed in detail in the following sections. It is interesting to note that the same CMC equation was derived by two different researchers (Bilger [32], Klimenko [33]) from different formulations of the conditioned quantities. This gives some hope that the CMC frame work is valid, in general, for the entire regime of turbulent combustion. Klimenko derives the CMC equation based on a JPDF approach whereas Bilger uses the above mentioned decomposition method. The similarities and differences in each derivation is discussed in detail in [59]. The resulting CMC equations introduce new un-closed conditional terms which require modeling. Specifically, the conditional averages of velocities, reaction rates and the conditioned scalar dissipation rate, N_η. Before entering into a detailed mathematical discussion of the CMC model it would be good to summarize, from a functional perspective with little numeric detail, the entire CMC method. The CMC method is summarized below in the following list.

1. With appropriate initial and boundary conditions, the CMC equation is solved (on a course grid) for N species, temperature, reaction rate, density or any other needed conditioned scalar resulting in conditional quantities ($\langle T|\zeta\rangle, \langle\rho|\zeta\rangle, \langle Y_i|\zeta\rangle, \langle\dot{\omega}_i(\rho, Y_i, T)|\zeta\rangle$).

2. The conditional quantities are transformed to unconditioned space by means of PDF integration with a presumed PDF shape resulting in "useable" unconditioned values (T, Y_i, ρ).

3. The CFD code uses this unconditioned density (ρ) with proper boundary conditions to solve the flow field for a given turbulence model, which predicts the turbulent time scale ($\tau = \frac{\epsilon}{k}$).

The turbulent time scale is used in the definition of scalar dissipation which is unconditioned in the variance equation and conditioned in the CMC equation.

4. The unconditioned reaction rate, density, temperature or scalar dissipation fields are needed for terms in the transport equations 2.33 and 2.34. These equations are then solved resulting in field values for the reaction progress variable, c, and its variance,c''^2.

5. The c field is then used to condition the unconditioned variables $\langle\rho|(c=\zeta)\rangle$ to rebuild the CMC equation. The new c and c''^2 fields are also used to determine the exact PDF shape used in step 2.

The steps 1-5 are repeated until convergence is reached in the flow and CMC fields. Although the grid size for the CMC equation is courser, due to weaker spatial dependencies with conditioned variable, it must be solved for N species, temperature and other scalar quantities. The resulting conditioned values, as stated in step 2, are transformed back to unconditioned space by means of a PDF function with a presumed shape. The uncondititional (ϕ) and conditional (ϕ_ζ) values can be related, by means of the PDF, by the following relation

$$\phi = \int \langle\phi|\zeta\rangle P(\zeta) dV, \tag{2.61}$$

where V is the volume of the CMC cell where the PDF integration is occuring. The CMC solution procedure is computationally costly and is noted to consume 85% of the entire solver (CMC & CFD) run time. An alternative to this approach is the tabulated premixed CMC (T-PCMC) method [38, 40] which solves the CMC equation (usually under steady conditions) for a range of RPV, variance, and conditional scalar dissipation, enthalpy or velocities. The solution is stored in a table, characterizing the T-PCMC as a table look-up method. The T-PCMC has advantages over previous table lookup-methods in that the tables are not empirically generated, they are instead generated "offline" by the solution of the CMC equations. This method is more computationally efficient with little increase in run time when compared to the cold flow! The validity of the T-PCMC

method for various regimes and transient scenario is still uncertain, accordingly this research work focuses on the validity of T-PCMC assumption and its applicability.

2.4.2 Non-Premixed CMC Model

The CMC model was originally implemented for non-premixed flames (NP-CMC). Many sub-models have been developed and the CMC approach has been successfully applied to various non-premixed combustion systems such as bagasse-fired boiler, hood fires [18], bluff-body stabilized and lifted jet flames [30], spray auto-ignition [71] and soot formation [72]. In the case of non-premixed method the conditioning variable is normally the mixture fraction (ξ) which is zero in the oxidizer stream and unity in the fuel stream making this suitable as a reaction progress variable. Notice the conditioning variable (mixture fraction) is a non-dimensional conserved scalar, this means that the c transport equation will be conserved and not include a reaction rate term ($\dot{\omega}_i$). Thus, the transport for the conserved scalar, ξ, (analogous to c) is given by

$$\rho\frac{\partial(\xi)}{\partial t} + \rho v\nabla\xi = \nabla\cdot(\rho D\nabla\xi), \tag{2.62}$$

where D is the mixture fraction diffusion coefficient. Note the similarity of Eq. 2.62 to the pre-mixed c transport equation (Eq.2.13) except the missing reaction rate term, this is due to the fact the ξ is a conserved scalar. Moreover, this simplification occurs since mass fraction, used normally as a dependent variable, is used as an independent variable. Bilger observed that in diffusion flames most fluctuations in mass fraction were associated with fluctuations of the mixture fraction.

The non-premixed CMC equations are derived by using this definition of c in the mass fraction transport equation (Eq. 2.8) and decomposing the resulting transport equation in a similar fashion as described in section 2.4.1. After derivation, the resulting non-premixed CMC equation is written

as,

$$\underbrace{\frac{\partial \rho Q}{\partial t}}_{T1} + \underbrace{\langle \rho u|\zeta\rangle \frac{\partial Q}{\partial x}}_{T2} = \underbrace{\langle \rho \omega|\zeta\rangle}_{T3} + \underbrace{\frac{Le_c}{Le_i}\langle \rho N|\zeta\rangle \frac{\partial^2 Q}{\partial \zeta^2}}_{T4} + \underbrace{e_y}_{T5} + \underbrace{e_Q}_{T6}. \tag{2.63}$$

where $Q \equiv \langle Y(x,t)|c=\zeta\rangle$ is the conditional mean of the desired scalar quantity, ζ is the sample space variable for c, ω is the reaction rate and N is the unconditioned scalar dissipation. Term T1 represents the unsteady changes in the conditional mean. Term T2 represents the convection of the conditional scalar by means of a conditioned velocity $u_\eta = \langle u|\zeta\rangle$, which requires modeling. Term T3 is the conditional reaction rate for species i. Term T4 represents the diffusion of conditional averages in the sample space η. Term T5 (e_y) represents the effect of the conditional fluctuation ($\langle u_i'' y_i\rangle$) on the evolution of Q. The last term, Term T6 (e_Q), represents the molecular diffusion of Q_i in physical space and the differential diffusion of mass and heat. Terms T5 and T6 are described in detail in section 2.4.3 and are usually neglected in the case of unity Lewis number and high Reynolds number flows.

The conditioned reaction rate, $\omega|\eta$, is approximated using a first order CMC closure as

$$\omega_\eta = \langle \rho\omega|\zeta\rangle \equiv \omega(Q_1, Q_2 .... Q_{ns}, Q_h) \tag{2.64}$$

, where the subscripts ns is the total number of species and h is the enthalpy. The first order CMC approximation takes note that detailed kinematic information is available in the N solutions of the CMC equation. Thus, the reaction rate is summed based on the contribution from each N species and conserved quantities (such an enthalpy, h). Since the fluctuating components of the species and enthalpy is known to be much smaller in conditioned space, a better approximation of the reaction rate than the normal unconditioned methods is achievable. Experiments have shown that for some problems the conditioned variables are approximately constant in certain spatial coordinates, so the spatial gradients can be ignored, reducing the dimensionality of the problem. Smith [55], Mastorakos [26, 62], Kronenbug [46] and Bilger [32] give some examples of non-premixed results in URANS and LES context.

2.4.3 Premixed CMC Model

The Conditional Moment Closure (CMC) method for premixed combustion is described in this section in its original RANS/URANS formulation. The premixed version of the CMC follows an identical solution procedure to that of NP-CMC except for the addition of source terms ($\dot{\omega}$) which appear in the RPV, c, and its variance, c. These new terms are a result of the chosen representation for the RPV. In the case of premixed CMC (P-CMC), the RPV is a reactive scalar which can be defined by ratios of the temperature, fuel mass fraction (Y_f) [32] or sensible enthalpy(h^s) [38, 40]. In this work the sensible and total enthalpy are used to represent the RPV since no assumptions are made regarding the changes in specific heat Cp. Additionally, this definition for c allows the system to be used for a non-adiabatic case [61]. This is accomplished by allowing c to grow greater than unity. This represents the regime after combustion where burnt gases are cooling as the enthalpy of the system decreases. For adiabatic problems the enthalpy (h) remains constant and c becomes a function of only the sensible enthalpies, which is a common definition in the literature. Thus, the RPV is defined as

$$c = \frac{(h^s - 2h) - (h^s_u - 2h_u)}{h^s_{b,ad} - h^s_u - 2h_e + 2h_u}, \qquad where \qquad c\begin{cases} c{=}1,\ Burnt\ State \\ c{=}0,\ Unburnt\ State \end{cases} \tag{2.65}$$

and the subscripts u and b signify the unburnt and burnt state, respectively. The filtered transport equations for mass fraction, total enthalpy, variance and RPV (Eq.2.8, 2.7, 2.13, 2.34) are used in this formulation. Adequate models are needed to close terms $cVar3$ through $cVar7$ in the variance equation (Eq:2.34) and is be discussed in section 3.4.

The P-CMC equation is derived, in a similar fashion to the UP-CMC, by inserting the representation of RPV (Eq. 2.65) into the filtered species mass fraction transport equation (Eq. 2.31) and then conditionally averaging the resulting transport equations, conditioned by the value of the RPV i.e. $\langle Q|c = \zeta\rangle$. Although this method is popular for its simplicity, an identical result can be found by following the JPDF approach by Klimenko [31]. It is important to note that the decomposition

of the conditional scalar, in the below formulation, is not performed with Favre density weighted averaging, the Favre averaged CMC equation is discussed later in section 3.4 where sub-grid scale filtering is incorporated into the sub-models of the P-CMC. The resulting unfiltered premixed CMC equation is written as,

$$\langle\rho|\zeta\rangle\frac{\partial Q_i}{\partial t}+\langle\rho\mathbf{U}|\zeta\rangle\cdot\frac{\partial Q_i}{\partial x_i}=\langle\rho\dot{\omega}_i|\zeta\rangle+\frac{Le_c}{Le_i}\langle\rho D_i\nabla c\cdot\nabla c|\zeta\rangle\frac{\partial^2 Q_i}{\partial\zeta^2}-\langle\rho S_c|\zeta\rangle\frac{\partial Q_i}{\partial\zeta}+e_Q+e_y, \quad (2.66)$$

Correspondence between Eq. 2.63 and Eq. 2.66 is very close and each term has the same physical representation as detailed in 2.4.2, except for the inclusion of a new source term, $\langle\rho S_c|\zeta\rangle\frac{\partial Q_i}{\partial t}$. This term appears since the RPV is now reactive and, in effect, will have its own fluctuations which contribute to the evolution of Q_i. The error term e_Q represents effects of molecular, thermal, and mass diffusion on the transport of the conditioned variable Q_i.

$$e_Q=\frac{1}{P_\zeta}\{2\frac{\partial\langle\rho D_i(\nabla c\cdot\nabla Q_i)|\zeta\rangle P_\zeta}{\partial\zeta}+\nabla\cdot\langle\rho D_i|\zeta\rangle\nabla(Q_iP_\zeta)-Q_i\nabla\cdot(\langle\rho D|\xi\rangle\nabla P_\xi)\} \quad (2.67)$$

Klimenko and Bilger [46] show that when a laplacian is applied to an averaged value the order of the term does not increase, such that $\nabla\langle\rho D_i|\xi\rangle\sim\langle\rho D_i|\xi\rangle\sim\frac{1}{Re}\to 0$. This makes the second and third terms negligible for high Reynolds number ($Re>2000$) which is most often the case in industrial applications. The remaining term can be assumed to be zero based on the argument This is a well known argument that high Re flows do not depend on molecular diffusivity. Although it is not clear if this argument can be applied to the first term, the assumption for premixed flows that Q is uniform within the reactor volume, causes the term to vanish since $\frac{\partial Q_i}{\partial x_i}=\nabla Q_i=0$. The error term e_y represents the effect of fluctuations by the conditional mean, Q_i'', and is written as

$$e_y=\frac{1}{P_\zeta}\{2\frac{\partial\langle\rho D_i(\nabla c\cdot\nabla Q_i)|\zeta\rangle P_\zeta}{\partial\zeta}-\frac{\partial^2\langle\rho D_i(\nabla c)^2Q_i|\zeta\rangle P_\zeta}{\partial\zeta^2}-\nabla\cdot(\langle\rho uQ_i|\zeta\rangle P_\zeta)-\frac{\partial\langle\rho S_cQ_i|\zeta\rangle P_\zeta}{\partial\zeta}\}. \quad (2.68)$$

Under the same assumption that scalar fluctuations are small for premixed combustion, one can ignore the effect of e_y since all terms have a $\frac{\partial Q_i}{\partial\xi}$ term. For flows where ignition and extinction

are present in the flame, the error terms play an important role since the gradients of Q will begin to be large and must be accounted for. Models for the conditional fluctuations in e_y have been developed adopting a gradient approximation, such that $\langle \rho u Q_i | \zeta \rangle = -D_t \nabla Q_i$. When limited to high Reynolds number flows the model gives a reasonable approximation [26, 46, 62]. The modeling of these two error terms in the literature is unresolved for both gradient and counter-gradient diffusion. The inclusion of both e_q and e_y is sparsely used in the literature solely for cases where local extinction of the flame is present [26, 46, 61, 62].

CHAPTER 3: MODEL IMPLEMENTATION

To describe the T-PCMC model a "top to bottom" approach is taken. Section II will begin with a description of the T-PCMC model flow chart, showing the basic inputs, outputs and shared variables between the CFD code and the tabulated solutions to the T-PCMC equations. The model specific equations solved offline by the combustion model and during run time by the CFD code will be discussed in more detail after a general description of the code is presented.

Figure 3.1 illustrates the T-PCMC model and how the premixed CMC table interacts with the CFD solver. The components within the dotted box refer to the T-PCMC table which is generated offline by solving a T-PCMC equations for each species in the mixture (ns) and for a range of scalar dissipation rate (N) values. Each species' T-PCMC equation is solved with the species' respective burnt and unburnt conditions. Changing the scalar alters the rate of diffusion of the mixture and the solution of the T-PCMC equation. By solving the T-PCMC equation for each species and for a range of N values a table may be constructed with the tabulated solutions for use by the CFD code.

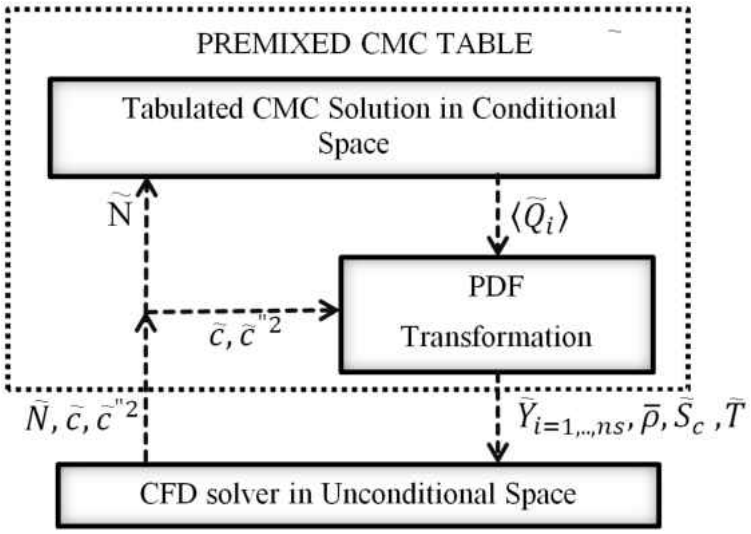

Figure 3.1: Flow Chart of the T-PCMC model

The value of N computed by the CFD is used to index the correct conditioned scalar ($\langle \tilde{Q}_i \rangle$) from

the table. Interpolation between N tables is not performed in this work, but the spacing between tables (dN) is dynamic and allows for dN to shrink at low N, where conditioned scalars show the strongest dependence on N. It was found that the conditioned scalars became independent of N at $N > 5000[1/s]$. In future work it would be beneficial to interpolate between N tables, although this would add a substantial amount to the run time of the simulation.

Once the correct N table is chosen, a set of conditioned values for mass fraction (Y_i), density (ρ), RPV source term (S_c) and temperature (T) may be accessed as a function of c. A PDF function integration is then used to transform the conditional quantities back to unconditioned space for use by the CFD. The PDF function takes an exact shape based on the values of the RPV (c) and its variance (c''^2). The PDF construction and integration is discussed in detail in section II.B. Once the conditioned scalars are transformed back to unconditioned space the 53 species mass fractions, density, RPV source term, molecular weight (MW) and temperature are available for use in the CFD code. The temperature is used to update the thermodynamic quantities of the mixture. S_c is used as the source term in the transport of c and $c^{"2}$. The transport equations for c and $c^{"2}$ are solved in transient form by the CFD code and in three spatial dimensions.

3.1 CFD Solver in Unconditional Space

The CFD code is required to solve for the flow field equations (continuity and momentum), the RPV transport equation (c), the variance transport equation ($c^{"2}$) and the scalar dissipation rate (N) at every time step and for every cell in the domain. At each time step every cell in the domain has available the unconditioned density, temperature, RPV source term, molecular weight and the 53 species mass fraction from the T-PCMC table.

To quantify the progress of the flame, a suitable quantity must be chosen to define the RPV. For non-premixed combustion the mixture fraction is used as the RPV. In premixed flow the mixture

fraction is constant and has no use as a variable to which remaining variables are conditioned. In this work, the change in sensible enthalpy is used to define the progress of the reaction (c) as in Eqn. 2.12. $c = 0$ and $c = 1$ corresponds to the fully unburnt and burnt conditions, respectively. In this arrangement, c is a monotonically increasing function and any fuel mixture can be used since the RPV does not depend on the mass fraction of any specific major species.

To develop a transport equation for the RPV, the RPV is first decomposed into its mean and fluctuating components using a density weighted Favre average ($\tilde{c}$). A density weighted average is employed since the fluctuations in density ($\bar{\rho}'$) are not required in Favre averaging. To solve for the RPV the Favre averaged transport equation for sensible enthalpy is substituted into equation **??**, as in **??**[40], resulting in Equation 3.1.

$$\bar{\rho}\frac{\partial(\tilde{c})}{\partial t} + \frac{\partial(\tilde{u}_i\tilde{c})}{\partial x_i} = \bar{\rho}\frac{\partial}{\partial x_i}\Big(\overline{D_c\frac{\partial\tilde{c}}{\partial x_i}} - \overline{\tilde{u}_i''\tilde{c}''}\Big) + \frac{[\sum_i \bar{\rho}\tilde{\omega}h_{f,i}]}{\Delta h^s_{ad-u}} = \nabla(\frac{\mu_t}{\sigma_c}\nabla\tilde{c}) + \bar{\rho}\tilde{S}_c. \tag{3.1}$$

Here $\bar{\rho}$ is the density, $\tilde{u}_i$ is the velocity in all three directional components, $\tilde{c}$ is the RPV, $\tilde{S}_c$ is the RPV source term and D_c is the diffusion rate of c which requires modeling. The spatial derivatives of the diffusivity (D_c) have been negated since in the T-PCMC model conditional species are assumed uniform. If the species are uniform in conditional space then there will be no changes in the mixture diffusion rate in conditional space. Instead, as in previous CMC work [7, 27, **?**], the diffusion is modeled assuming a Fick's law diffusion. Fluctuations in density are neglected since a density weighted Favre filter is used which reduces the magnitude of density fluctuations in the governing equations for c and variance. $\tilde{\omega}_i$ is the reaction rate of species i, $h_{f,i}$ is the heat of formation of species i, Δh^s_{ad-u} is the difference in sensible enthalpy between the adiabatic equilibrium and unburnt states, h^s is sensible enthalpy at the local temperature and h^s_u is the sensible enthalpy at the unburnt state. The diffusion term is unclosed due to the second moment term $\overline{\tilde{u}_i''\tilde{c}''}$. The second to last term on the RHS shows the diffusion term in closed form which uses the turbulent viscosity (μ_t) and turbulent Schmidt number ($\sigma_t = 0.7$) to represent the diffusion rate of the RPV.

The last term $\bar{\rho}\tilde{S}_c$ is the mean reaction rate of the RPV and is tabulated in the T-PCMC table by

$$\tilde{S}_c = \frac{[\sum_i \bar{\rho}\tilde{\omega}h_{f,i}]}{\Delta h^s_{ad-u}}. \tag{3.2}$$

In addition to the governing equation for the RPV (Eqn. 3.1), a transport equation for the variance (c''^2) of the RPV is solved. Typically, algebraic models for the variance are used which assume the variance is directly proportional to the scalar dissipation rate [22]. This assumption does not allow for the scalar dissipation rate to exist without the presence of variance or a change in the RPV. It is shown in DNS comparisons of a C_2H_4 turbulent jet flame [34] that algebraic models failed to adequately reproduce the DNS results in comparison to results obtained from a transport equation of the variance.

The transport equation for the variance of RPV is derived by subtracting the Favre filtered $\tilde{c}$ equation from its instantaneous c equation. Following previous literature [7, 27, **?**], the derivatives of the diffusivity (D_c) in space have been negated and is instead modeled assuming a Fick's law diffusion. The mean molecular transport is negated since turbulent transport is the dominant diffusion mechanism in the high Reynolds number flows considered in this work. The transport equation for the variance of the RPV (cVar) is written below as

$$\underbrace{\frac{\partial(\bar{\rho}\tilde{c}''^2)}{\partial t}}_{cVar1} + \underbrace{\frac{\partial(\bar{\rho}\tilde{u}_i\tilde{c}''^2)}{\partial x_i}}_{cVar2} = \frac{\partial}{\partial x_i}\Big(\underbrace{\overline{\rho D_c \frac{\partial \tilde{c}''^2}{\partial x_i}}}_{cVar3}\Big) - \Big(\underbrace{\overline{\rho u_i'' \tilde{c}''^2}}_{cVar4}\Big) - \underbrace{2\overline{\rho u_i'' \tilde{c}''}\frac{\partial c}{\partial x_i}}_{cVar5} - \underbrace{2\bar{\rho}\tilde{N}_c}_{cVar6} + \underbrace{2\overline{\tilde{c}''\dot{\tilde{\omega}}_c}}_{cVar7}. \tag{3.3}$$

The first two terms (cVar1,2) of the LHS of Eqn. 3.3 represent the temporal and spatial changes of the variance of c by means of convection. Terms cVar3 represents the diffusive flux of the variance. Both D_c and $\overline{\rho u_i'' c''^2}$ require modeling. Terms cVar4 and cVar5 both represent the effects of mean and fluctuating strain fields and the interaction of turbulence u_i'' and scalar fields c''. These two terms are lumped together as both include a second moment term $\overline{a''b''^2}$ which require modeling, these terms are related to the scalar dissipation rate, $\tilde{N}_c$. Term cVar6 represents the effect of the

scalar dissipation rate on the variance. Since c is a reactive scalar, the production of variance $\overline{c''^2}$ due to chemical reaction exists and is represented by the last term cVar7 in Eqn. 3.3 [38]. Since models are required for most of these terms the implemented form of the equation is shown below in Eqn. 3.4.

$$\underbrace{\bar{\rho}\frac{\partial(\tilde{c}''^2)}{\partial t}}_{cVar1_i} + \underbrace{\bar{\rho}\,\frac{\partial(\tilde{u}_i\tilde{c}''^2)}{\partial x_i}}_{cVar2_i} = \underbrace{\nabla^2(i_{eff}\tilde{c}''^2)}_{cVar3_i} + \underbrace{C_{c1}\mu_t(\nabla\tilde{c})^2}_{cVar4_i} - \underbrace{\rho\tilde{N}_c}_{cVar5_i} - \underbrace{10\frac{\tilde{c}''^2}{\tilde{T}(\tilde{c}+\frac{T_u}{T_{ad}-T_u})\tilde{S}_c}}_{cVar6_i} \tag{3.4}$$

Here i_{eff} is modeled by the contribution of laminar and turbulent thermal diffusivities in the URANS formulation. μ_t is the turbulent viscosity, which is also modeled in URANS to close the Reynolds stress tensor. The model constants (C_{c1}, C_{c2}) for the closure of terms cVar4$_i$ and cVar5$_i$ in Eq. 3.3 have been adjusted in comparison to the theoretical values of $C_{c1} = 2.86$ and $C_{c2} = 2.00$. C_{c2} is used in the model for N as in Eqn. 3.22. A value of 2.86 is obtained by $2/\sigma$ where σ is the Schmidt number equal to 0.7. These values are originally derived from non-reacting turbulence theory [45]. It is expected that in the premixed formulation of the variance equation these constants must change since there is a production term in the variance equation, which is not the case for non-reacting variance or non-premixed variance transport equations. The original values are obtained from non-reacting turbulent theory and resulted in large values of the variance, giving a lower flame temperature and larger flame thickness. It was evident from the initial values that there was an overproduction of variance, limiting the C_{c1} and increasing C_{c2} was performed once and has performed well for multiple geometries, mesh resolutions and boundary conditions [38, **?**, 64]. The adjusted model constants are , 0.715 and 8.00, respectively. The URANS model has shown a weaker dependence on the values for C_{c1} and C_{c2} in comparison to the steady RANS version presented in Ref. [**?**, 39]. The LES formulation of the T-PCMC model has shown the weakest dependence on the model constants, since N is redefined in LES framework to represent the SGS. It was found that good agreement was also found when using the theoretical values for C_{c1} and C_{c2} with the LES T-PCMC model. In contrast, RANS and URANS implementations both

over predicted variance when using the theoretical C_{c1} and C_{c2} values.

The unconditioned scalar dissipation $\tilde{N}_c = D_c \frac{\partial \tilde{c}}{\partial x_i} \frac{\partial \tilde{c}}{\partial x_i}$ is modeled in the RANS/URANS version of the T-PCMC model as

$$\tilde{N}_c = C_{c2} \frac{\tilde{\varepsilon}}{\tilde{k}} \tilde{c}''^2, \tag{3.5}$$

where $\tilde{\epsilon}$ is the turbulent dissipation rate, $\tilde{k}$ is the turbulent kinetic energy and $\tilde{c}''^2$ is the variance which is obtained by solution of equation 3.4. An improved model for $\tilde{N}_c$, formulated for URANS, has been proposed in Refs.[2, 3] which additionally includes the effects of molecular diffusion. The additional terms, representing the chemical and molecular diffusion, are inversely proportional to the Ka # ($\frac{1}{Ka^{0.4}}$) [2]. Under the well mixed assumption used in this work, Ka is large ($O(10-100)$), accordingly the inclusion of chemical diffusion is considered small compared to that of turbulent diffusion. Note that the unconditioned form of N is shown in equation 3.22, in contrast the T-PCMC table uses a conditional N to index and solve the T-PCMC equation. The transformation from unconditioned to conditional N will be discussed in subsection B.

3.2 The T-PCMC Solution in Conditional Space

Referring to figure 3.1, the T-PCMC table must take in values of RPV, its variance, scalar dissipation rate and output the unconditioned species mass fractions, density, temperature and RPV source term. To generate these values, the T-PCMC method solves a reduced premixed CMC formulation in conditional space. A brief derivation of the T-PCMC equation is provided below and interested readers are referred to Ref.[40] for a detailed derivation and description.

The species mass fractions can be decomposed into its Reynolds decomposition representing the

mean ($\tilde{Y}_i$) and fluctuating component (y_i).

$$Y_i(x,t) = \tilde{Y}_i(x,t) + y_i(x,t) \tag{3.6}$$

In unconditional space ($f(x,t)$) the fluctuating component can be the same order of magnitude as the mean value. In conditional space $\tilde{Q}_i$ is representative of any unconditioned scalar, like the species mass fraction $\tilde{Y}_i$. Notice that the same decomposition can be performed except with the conditional mean ($\tilde{Q}_i$) and its respective fluctuation (q_i) from the mean.

$$Y_i(x,t) = \tilde{Q}_i(\tilde{c}(x,t),x,t) + q_i(c,x,t). \tag{3.7}$$

Here, q_i is the conditional fluctuation and $\tilde{Q}_i$ is the conditional mean of Y_i. Note that by conditioning $\tilde{Y}_i$ with values of the RPV, a new dimension, $\tilde{c}$, is introduced. With this added dimension, conditional fluctuations (q_i) are greatly reduced $y_i >> q_i$ and adequate accuracy can be obtained from a first order approximation, i.e., $Y_i \sim \tilde{Q}_i$.

In order to condition the equations of species mass transport ($\tilde{Y}_i$) on the value of the RPV (c), a Favre averaged conditional moment of the species mass fraction is performed below as

$$\tilde{Q}_i(\tilde{c},x_i,t) \equiv \frac{\langle \bar{\rho}(x_i,t)\tilde{Y}_i(x_i,t)|\tilde{c}(x_i,t)=\zeta\rangle}{\langle \bar{\rho}(x_i,t)|\tilde{c}(x_i,t)=\zeta\rangle}, \tag{3.8}$$

where vertical bars indicate the average is taken over only those values of Y where c equals ζ (the condition) and the angle brackets indicate an average value. ζ is equivalent to c, but in conditional space, i.e., ζ is a set of values in c space representative of the c values in real space. As in c, ζ

ranges from 0 to 1 which represent the unburnt and fully burnt conditions.

With a filtered conditional representation of the species mass fraction available, the derivation of the premixed CMC equation can be performed as follows. Equation 3.8 is substituted into equation 3.7 which is then used to replace Y_i in the reactive species mass fraction transport equation. Lastly, equation 3.1 is substituted into the resulting mass fraction conservation equation and conditionally averaged resulting in

$$\langle\bar{\rho}|\zeta\rangle\dot{\tilde{Q}}_i + \langle\bar{\rho}\tilde{\mathbf{U}}|\zeta\rangle\cdot\nabla\tilde{Q}_i = \langle\bar{\rho}\dot{\tilde{\omega}}_i|\zeta\rangle + \langle\bar{\rho}D_i\nabla\tilde{c}\cdot\nabla\tilde{c}|\zeta\rangle\tilde{Q}_i{}'' - \langle\bar{\rho}\tilde{S}_c|\zeta\rangle\tilde{Q}_i{}' + e_Q + e_y. \tag{3.9}$$

In equation 3.9, the primes indicate derivatives in c space, the gradient operator (∇) is a derivative with respect to physical space and the dot indicates a time derivative. Equation 3.9 is similar in form to the NPCMC equation, except for the addition of $\langle\rho\tilde{S}_c|\zeta\rangle\tilde{Q}_i{}'$ which appears as a consequence of c being a reactive scalar and represents the convective velocity in c space. The addition of this convective velocity term makes the PCMC equations stiffer than the NPCMC formulation. Moreover, the PCMC equation becomes stiffer as N approaches the theoretical limit of zero. For a detailed description of each term the reader is referenced to [38].

To make equation 3.9 more usable for tabulation, simplifying assumptions are made. The following simplifications are made to reach the T-PCMC equation which is proposed to be applicable for well-stirred or distributed reaction regimes. Bilger states in Ref. [61] that for stationary turbulent flows, as in the discussed flame, conditional averages will depend weakly on time ($\frac{\partial\tilde{Q}_i}{\partial t} \approx 0$). Thus the time derivative of conditional quantities is removed from equation 3.9. Although this assumption will limit the applicability of the model to stable flames, the temporal fluctuations in c and c''^2 are accounted for in equations 3.1 and 3.4. Since $\tilde{Q}_i \sim f(c)$, the temporal changes

of Q, in c space, are implicitly accounted for in equations 3.1 and 3.4. The removal of the time derivative in the PCMC equation allows the T-PCMC table to be decoupled temporally from the flow field equations. This is key to solving for the T-PCMC equations offline and storing them in a tabulated format. The two error terms (e_Q, e_y) are negligible. e_Q is negligible since it scales with $Re^{-1/2}$ making it small for highly turbulent flow. e_y is dependent on q_i and is considered negligible since the fluctuation of the conditional mean q_i is small; thus the gradient of the fluctuations in real space, ∇q_i, should also be small. Negating e_Q and e_y additionally implies that differential diffusion effects are neglected. For a detailed derivation and description of e_Q and e_y, the reader is referenced to Ref.[40]. In the case of unity Lewis number, such as the methane (CH_4) flame under consideration, the assumption is appropriate as differential diffusion effects are small when thermal and mass diffusivities are equal. Based on the discussed assumptions Eqn. 3.9 reduces to

$$\langle \bar{\rho}\tilde{\mathbf{U}}|\zeta\rangle \cdot \nabla \tilde{Q}_i = \langle \bar{\rho}\dot{\tilde{\omega}}_i|\zeta\rangle + \langle \bar{\rho} D_i \nabla \tilde{c} \cdot \nabla \tilde{c}|\zeta\rangle \tilde{Q}_i{}'' - \langle \bar{\rho}\tilde{S}_c|\zeta\rangle \tilde{Q}_i{}'. \tag{3.10}$$

No major assumptions have been made to restrict the combustion regime of the premixed flame, except that the flow is turbulent and the flame is stationary. To adapt the remaining expression to the well-stirred or distributed reaction regimes it is conjectured that in the case of a well stirred reactor, the conditional scalars (not the unconditioned scalars) are approximately uniform over real space. This assumption results in small gradients of the conditioned species mass fraction in real space which reduces $\nabla \tilde{Q}_i$ to zero, removing the second term from equation 3.9. The same assumption, $\nabla \tilde{Q}_i = 0$, would also remove the e_Q term for its additional dependence on $\nabla \tilde{Q}_i$. The assumptions that $\nabla \tilde{Q}_i = 0$ and $\nabla \tilde{q}_i = 0$ will limit the range of scalar dissipation values that are valid in this model, even though other values may give a solution. To better determine the relative magnitude of the assumptions taken to reach equation 3.11, additional DNS and experimental data are required for the reaction regimes under consideration. It is anticipated that this assumption is

valid for low to moderate Da# or flames with characteristics of a well-mixed or distributed reaction regime. This final assumption ($\nabla\tilde{Q}_i = 0$) results in the T-PCMC equation written as

$$\langle\bar{\rho}D_c\nabla\tilde{c}\cdot\nabla\tilde{c}|\zeta\rangle\tilde{Q}_i'' - \langle\bar{\rho}\tilde{S}_c|\zeta\rangle\tilde{Q}_i' + \langle\bar{\rho}\dot{\tilde{\omega}}_i|\zeta\rangle = 0. \tag{3.11}$$

The first term in equation 3.11 is the conditioned scalar dissipation rate, which represents scalar diffusion in RPV space. The diffusion (D_c) is the diffusivity of the RPV which is represented in this work as the thermal diffusivity. The second term is the conditional source term of the RPV which resembles convection in RPV space. The third term represents the conditional reaction rates of species i and is the source term of the equation 3.11.

It is interesting to note that Eqn. 3.11 can also be reached from Eqn. 3.9 by assuming fast chemistry at a quasi-equilibrium, such that $\langle Y|\zeta\rangle = Y^e(\zeta)$ in the CMC Eqn. [**?**]. This corresponds mathematically to $\nabla\tilde{Q}_i = 0$, since $\tilde{Q}_i$ reduces to only a function of c, but the physical assumption of a thin flame is quite different from that of a distributed reaction.

Even though equation 3.11 has a similar form to the steady flamelet equation, there are three distinct differences in the implementation of equation 3.11 (T-PCMC) to the premixed steady laminar flamelet equations as used in Ref. [21, 25]. First, scalars are conditionally averaged providing reduced fluctuations from the mean which incur less error in gradient diffusion or Fick's Law approximations. Fick's Law assumes that diffusion occurs at a steady state. For diffusion to be theoretically steady, the temporal fluctuations of the mean concentration gradients must approach zero. Since temporal fluctuations from the mean are reduced in conditional space, a closer match to the assumed steady diffusive state is obtained. Secondly, the local scalar dissipation rate is calculated for each cell in the domain and the effect of small scale turbulence on the reaction rates is directly included. Although flamelet models can also achieve this, laminar flamelet models assume the flow is laminar at the small scales, therefore a constant N ($N \neq f(c)$) value is prescribed and is volume averaged across the entire computational domain as in Ref. [21, 22, 25]. The third and

most influential distinction is in the physical closure, provided by the first order CMC approximation, of the mean reaction rate ($\tilde{\omega}_i$). The mean conditional reaction rate from all ns species is closed using a first order approximation of the conditioned scalar. Neglecting conditional fluctuations ($q_i = 0$) allows the individual mean reaction rates to be summed up for all ns species and then conditionally averaged. This closure provides a physical representation of the mean reaction rate based on the chemical composition and thermodynamic state of the entire mixture. This first order closure is written below as

$$\langle \bar{\rho}\dot{\tilde{\omega}}_i|\zeta\rangle \simeq \langle\bar{\rho}|\zeta\rangle\dot{\tilde{\omega}}(\tilde{Q}_1, \tilde{Q}_2, ..., \tilde{Q}_{ns}). \tag{3.12}$$

Note that $\dot{\tilde{\omega}}_i$ additionally appears in the closure of the RPV source term (Sc), the convective term of equation 3.11.

Equation 3.11 is coupled to the flow field equations by the conditional scalar dissipation rate, $\langle\tilde{N}_c|\zeta\rangle = \langle\rho D\nabla\tilde{c}\cdot\nabla\tilde{c}|\zeta\rangle/\langle\bar{\rho}|\zeta\rangle$. Accordingly, a scalar dissipation rate must be calculated by the CFD ($\tilde{N}_c$), in unconditioned space, to be able to index the correct N solution set from the table. Note that ($\tilde{N}_c$) must first be converted to a conditional scalar dissipation rate ($\langle\tilde{N}_c|\zeta\rangle$), as in Eq. 3.11.

For complete closure of equation 3.11, $\langle\tilde{N}_c|\zeta\rangle$ requires modeling. Experimental measurements of $\langle\tilde{N}|(\zeta = c)\rangle$ for premixed flames do not exist in the literature and closures for $\langle\tilde{N}|(\zeta = c)\rangle$ have solely been developed and validated in non-premixed CMC formulations. In recent premixed CMC work [61] the non-premixed closure for $\langle\tilde{N}|(\zeta = c)\rangle$ is adopted due to a lack of validated models for the conditional scalar dissipation rate in premixed flow. Typically in NPCMC models a bell-shaped PDF function is used to statistically weigh the conditioned N ($\langle\tilde{N}_c|\zeta\rangle$) as a function of its unconditioned value ($\tilde{N}$). The methodology is best known as the Amplitude Mapping Closure [20]. Similarly, in this work, a parabolic curve is used to model the shape of $\langle\tilde{N}_c|\zeta\rangle$. The parabolic shape was developed using results from a premixed flamelet solution set (not shown here) which

showed a nearly symmetric relationship for the conditional scalar dissipation as a function of the RPV. $\langle \tilde{N}_c|\zeta \rangle$ has its maximum value at c=0.5 and is formulated as

$$\langle \tilde{N}|\zeta \rangle = 4\tilde{N}_c(\zeta(1-\zeta)) \tag{3.13}$$

A constant, equal to 4, is multiplied to ensure that the maximum value of $\langle \tilde{N}|\zeta \rangle$ is equal to the value of the unconditioned N ($\tilde{N}_c$) from the CFD, i.e. $\langle \tilde{N}|(\zeta = 0.5) \rangle = \tilde{N}_c$. To demonstrate the dependence of the conditional quantities on the conditioned N, a plot of the conditional RPV source term and CH_4 mass fraction is shown below in figure 3.2.

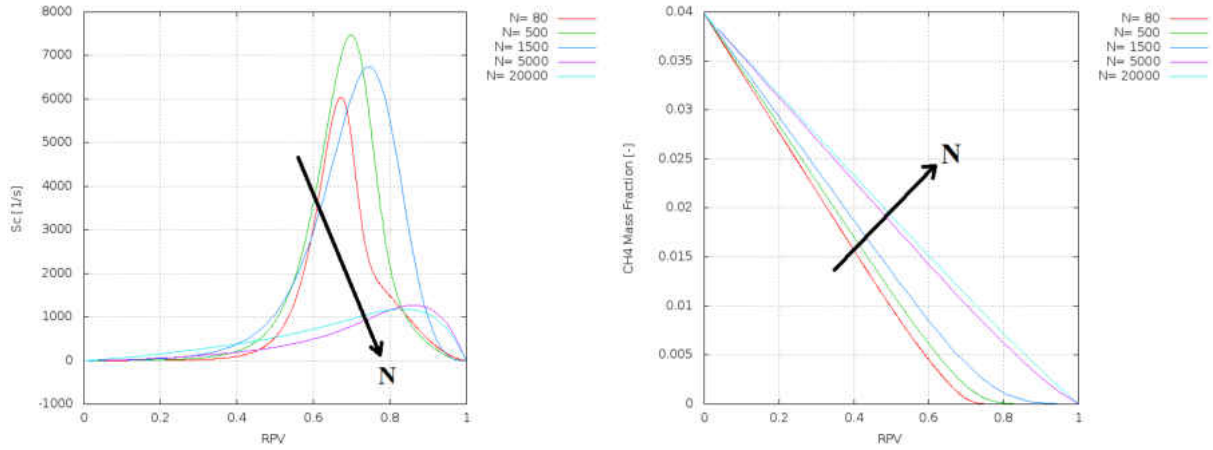

Figure 3.2: Adiabatic RPV source term (left) and CH_4 Mass Fraction (Right) versus RPV at various N.

Figure 3.2 demonstrates that conditioned quantities are least dependent on N, near the boundaries ($c = 0, c = 1$) and most dependent on N within the flame. With this in mind, closure of $\langle \tilde{N}|\zeta \rangle$ should be most accurate near the middle of the flame. For this reason the parabolic profile assumed in this work for $\langle \tilde{N}|\zeta \rangle$ is set to equal the unconditioned value for N at $c = 0.5$. As stated previously, it can be shown that the results are near independent of N when $N > 5000$.

Now with a model for $\langle \tilde{N}|\zeta \rangle$ in place, equation 3.11 is fully closed. Equation 3.11 may now

be written into 53 coupled, second order, non-linear, ordinary differential equations and solved simultaneously for a given value of N. Note that each species' T-PCMC equation is solved for the entire range of N, resulting in a data set of $\tilde{Q}_i \sim f(N = N_{min}, .., N_{max})$ where $i = 1, .., ns$.

To convert the resulting conditional averages ($\tilde{Q}_i$) to ensemble averages ($\tilde{Y}_i$) a PDF integration is performed on the conditional averages [31]. A Beta function PDF is used as in Ref.[57, 25, 22] and is defined as

$$P(\zeta; , \beta) = \frac{1}{B(\alpha, \beta)} \zeta^{\alpha-1}(1-\zeta)^{\beta-1}. \tag{3.14}$$

α and β are shape functions of the Beta function $B(\alpha, \beta)$ and are defined with respect to the RPV (c) and its variance (c''^2) as

$$\alpha = c\Big(\frac{c(1-c)}{c''^2} - 1\Big) \qquad\qquad \beta = (1-c)\Big(\frac{c(1-c)}{c''^2} - 1\Big) \tag{3.15}$$

The PDF assumes $0 < \zeta < 1$ and that the variance stay positive and below its theoretical maximum ($c(1-c)$). Both of these conditions are prescribed in the solution of the T-PCMC equations and the CFD code performs bounding of the c and c''^2 fields to ensure both criteria are satisfied. Note that this allows for a individual PDF shape to be used for each cell in the CFD domain, depending on the RPV and variance at the cell center. Recall that the RPV and variance are solved in 3-D and in transient using equations 3.1 and 3.4. The Beta function PDF is then integrated with the conditioned scalar over RPV space as in equation 3.16. The resulting PDF integration produces

the unconditioned scalar ($\widetilde{Y_i}$).

$$\widetilde{Y_i} = \int_0^1 \widetilde{Q_i}\tilde{P}(\zeta)d\zeta. \tag{3.16}$$

The authors note that this transformation, also used in premixed FGM [22] and CMC [61] models, is not particularly well suited for premixed flows. Recall, that the RPV is a reactive scalar in premixed combustion, i.e. there exists a production term for the RPV (S_c) in the transport equation for c and c''^2. Thus, the total distribution of the probability of $\tilde{Y}_i$ taking a value at $\tilde{\zeta}$ is not fully conserved, yet a conserved PDF is still used. This is analogous to using a Galton board to obtain a Gaussian distribution, except some of the dropped balls are removed or added and still a Gaussian distribution is expected. Further DNS or experimental data is required to quantify the error incurred when using conserved PDF transformations on a reactive progress variable. It is hypothesized that a corrected non-conserved PDF can be obtained through information of the current value of the RPV source term (Sc) since the removal of the RPV production term would make the RPV a conserved scalar, as in the non-premixed CMC formulation.

Now with the details on the governing equations described, subsection 3.3 will describe the procedure of numerically solving equation 3.11, for each species and for a range of N, to develop the T-PCMC table for use by the CFD code.

3.3 T-PCMC Table

To generate the T-PCMC table, Eqn. 3.11 is solved simultaneously for each ns species for a range of N values. Recall that N is the diffusive term in a species' T-PCMC transport equation. Thus by varying N the species transport from unburnt to fully burnt conditions becomes less or more

diffusive, while maintaining the same unburnt ($c = 0$) and fully burnt ($c = 1$) conditions.

Eqn. 3.11 is a system of second order, non-linear, ordinary differential equations of the boundary value type and is solved using a two point boundary value problem (TPBVP) solver [16]. The TPBVP solver is a global method to compute numerically the solution of a non-linear TPBVP. MIRK numerical schemes of orders 4, 6 and 8 are solved in a deferred correction framework to give a solution accurate to a prescribed local tolerance ($Q(10^{-}6)$) [16].

Eqn.3.11 is solved over a range of scalar dissipation values from 0.02$[1/s]$ to 20,000$[1/s]$. Smaller increments of N are used at low N due to the stiffness of the kinetics-turbulence interaction when $N < 10$. The boundary conditions for Eqn. 3.11 are the unburnt mass fractions at c=0 and the adiabatic equilibrium mass fractions at c=1. Chemkin along with the full GRI3.0 kinetic mechanism [54] is used to provide the species reaction rates ($\dot{\omega}_i$), sensible enthalpy (h_s), heat of formation ($h_{f,i}$), mixture specific heat (C_p), species specific heat($C_{p,i}$), mixture molecular weight (MW) and species MW as a function of temperature and species mass fraction. With these relationships available, the species reaction rate and diffusion coefficient can be determined for the simultaneous solution of Eqn. 3.9 ($\tilde{Q}_i$) for all ns species. Now the conditional density, temperature, species mass fractions and RPV source term can be computed for the CFD. Thermodynamic quantities were shown to satisfy the ideal gas law in both conditional and unconditional space.

The conditional RPV source term is closed as in Eqn. 3.1 since the individual species reaction rates and heat of formations are now available. The temperature is determined by iterating through the data set for a given combination of c and Y_i, that satisfies energy conservation. With the conditional temperature available, fixed pressure of 1atm and the MW of the mixture known, contributed by all 53 species, the density can be computed via the ideal gas law. The conditionally averaged results of density, temperature, species mass fractions and the source term for the RPV equation are stored in tabular format for each set of N conditions. At this stage, Eq. 3.16 is used to convert all of the conditioned scalars back to physical space for use by the CFD code. This transformation is also performed offline so that the CFD code receives the unconditioned quantities from the

T-PCMC table, preventing any added CFD run time from the PDF integration. The resulting unconditioned scalars are tabulated and linearly interpolated between the tabulated values for both c and c''^2. In the case of the dissipation rate, the index closest to the value of N is used. The resulting T-PCMC table is a 57x100x200x38 table where 57 scalars (53 species, density, molecular weight, temperature and source term) are indexed by 100 values of c ($0 < c < 1$), 200 values of variance ($0 < c''^2 < 0.25$) and 38 values of N ($0.02 < N < 20,000$).

To illustrate the output from the T-PCMC table the resulting density and temperature tables are illustrated in figure 3.3 and shown as functions of c and cVar. Both plots are made at a scalar dissipation rate of 200$[1/s]$. Although these contours are available for the entire range of c and cVar values, there are many regions which will never be encountered since the max variance is theoretically limited by c(1-c). To help limit these contours from non-physical combinations of c and cVar, values for which $c''^2 > c(1-c)$ are removed. It can be seen in figure 3.3 that both density and temperature at c=0 and c=1 have only one value at a variance of zero. At c=0, temperature is prescribed its unburnt value of 573K and at c=1 prescribed the fully burnt adiabatic value of 2064K. It can be seen that increasing variance results in a more distributed and uniform variation for density and temperature with c.

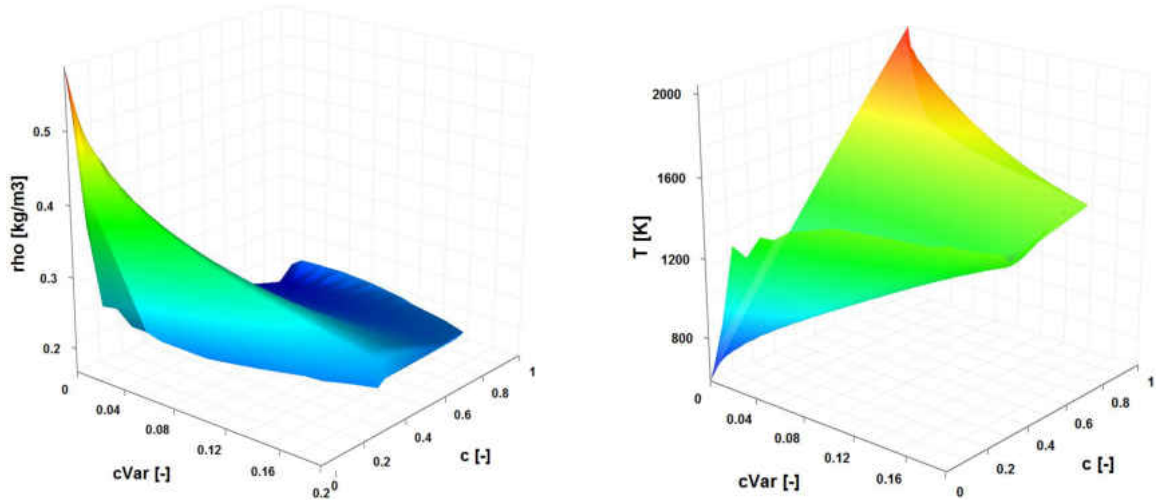

Figure 3.3: Density (left) and Temperature (right) as a function of RPV and variance at a scalar dissipation rate of 200$[1/s]$

Spikes at the extremes of the temperature and density fields demonstrate the stiffness of equation 3.11. Although figure 3.3 is useful in illustrating the table output, it is unclear the role of scalar dissipation rate and still un-physical combinations of c and cVar are encountered (cVar=0 at $0 < c < 1$). To help filter out the lower and upper bounds of the variance, the variance is adjusted based on a percentage of the max obtainable variance. Mathematically, $cVar = c(1-c)n\%$, where $n\%$ is the percentage of variance desired. This allows for an average variance to be obtained while preserving local changes in cVar with respect to c instead of holding variance constant for all values of c. In the CFD simulations it was found that approximately 10% of the maximum variance is achieved on average within the flame. Accordingly, in figure 3.4 a dynamic variance is used where all values of c are at a variance of 10% of their own theoretical maximum, c(1-c). Note that this value of average variance is solely used for illustration, the CFD and T-PCMC model are allowed to use the whole range of variance. Now with an average variance defined for each value of c the scalar dissipation rate can be included as an axis. This allows for illustration of the tabulated scalars for both major and minor species mass fractions as a function of c, cVar and N.

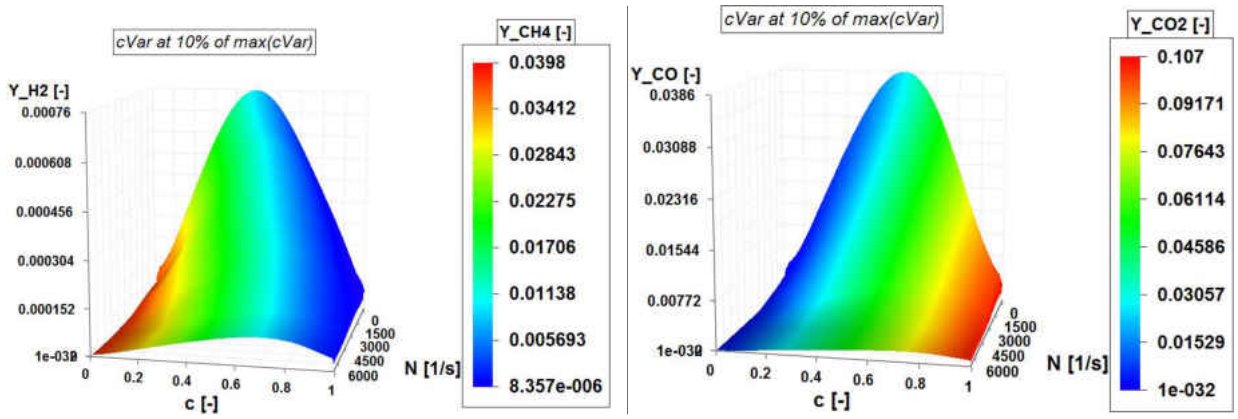

Figure 3.4: Unconditioned Hydrogen mass fraction (Left) (Y_{H_2}) as a function of RPV (c) and scalar dissipation rate (N) at a varince equal to $\frac{1}{10}C_{var,Max}$ colored by Methane mass fraction (Y_{CH_4}). Unconditioned Carbon Monoxide (Right) mass fraction (Y_{CO}) as a function of RPV (c) and scalar dissipation rate (N) at a varince equal to $\frac{1}{10}C_{var,Max}$ colored by Carbon Dioxide mass fraction (Y_{CO_2}).

Figure 3.4 shows two 3-D comparisons. On the left side Hydrogen (H_2) mass fraction is plotted

and colored by methane (CH_4) mass fraction. CO mass fraction is plotted on the right side and colored by the CO_2 mass fraction; both plots are shown as functions of c and scalar dissipation rate. Here it is evident the strong dependence of major and minor species on the scalar dissipation rate. It can be seen that at low N, where H_2 formation is largest, more CH_4 has been burnt, resulting in lower CH_4 with decreasing N. From a kinetics perspective, since there is less CH_4 there must be more CO_2 or more intermediates (CO,H_2) being formed. Looking at CO_2 on the right side of figure 3.4 shows that in fact less CO_2 is formed at low N. Thus if at low N there is less CO_2 and less CH_4, there must be more intermediate species, which is in accordance with the increase of H_2 and CO at low N values in figure 3.4.

For both plots in figure 3.4 the mass fractions become independent of any changes in N at approximately N=6000. The CFD results predicted N to range between 0.5-400$[1/s]$ within the flame ($0 < c < 1$). This encourages the notion that the effect of fluctuating N must be taken into account in combustion regimes where $Da\# < 1$ and changes in N are large within the flame.

The results from the CMC model show directly the effect large (variance) and small (N) scale turbulence have on the reaction rates and ultimately the species mass fractions. Moreover, the small scale mixing, $N = D\frac{\partial c}{\partial x_i}\frac{\partial c}{\partial x_i}$, has been shown to directly alter the reaction pathways, where at low N, the flame is thick ($\frac{\partial c}{\partial x_i} \rightarrow 0$) producing more intermediates and radicals. In contrast, at high N the flame is thin ($\frac{\partial c}{\partial x_i} \rightarrow \infty$) and the majority of CH_4 is directly converted to CO_2, similar to the behavior of single-step kinetic mechanisms.

The limiting cases of N in Eqn. 3.11 result in analogous solutions, in conditional space, for a perfectly-stirred reactor (PSR) and the fast chemistry approximation. These limiting cases are solely mentioned in this work and the interested reader is referenced to Ref.[41] for a more detailed discussion and derivation of the limiting cases of N. This promotes the idea that the validity of Eqn. 3.11 may be larger than expected and that the assumed regime in conditional space, where $\frac{\partial \tilde{Q}_i}{\partial x_i} = 0$, is applicable for a wider range of combustion regimes than originally assumed.

3.4 T-PCMC with Large Eddy Simulations

There has only been a single published work in the development of premixed CMC for LES. Bilger in 2013 formulated the same premixed CMC transport equations by applying a Favre density weighted (FDW) filter to the premixed CMC equation (Eq. 3.19) and by adopting the same sub-models used by non-premixed CMC models in premixed CMC. The FDW filter is given by

$$\tilde{P}(\zeta) = \frac{\int_{V_{cmc}} \bar{\rho} P(\zeta) dV}{\int_{V_{cmc}} \bar{\rho} dV}, \tag{3.17}$$

where V is the volume of the CMC cell. $\tilde{P}(\zeta)$ can now be used to convert the filtered conditional quantities back to uncondition space through the following relation.

$$\tilde{\phi} = \int \langle \tilde{\phi} | \zeta \rangle \tilde{P}(\zeta) dV \tag{3.18}$$

Although the FDM filtered premixed CMC equation is identical to Eq. 3.19, special care is needed to determine the filtering of each term. By using the SGS variance (c''^2_{sgs}) to construct the shape function in Equation 3.15 the PDF is implicitly filtered and density weighted (Favre Filter). With the FDM filter and neglecting error terms, the premixed CMC equation is

$$\widetilde{\langle \rho \dot{\omega}_i | \zeta \rangle} + \frac{Le_c}{Le_\alpha} \widetilde{\langle \rho N | \zeta \rangle} \frac{\partial^2 \tilde{Q}_i}{\partial \zeta^2} - \widetilde{\langle \rho S_c | \zeta \rangle} \frac{\partial \tilde{Q}_i}{\partial \zeta} = 0, \tag{3.19}$$

where the $\tilde{()}$ indicates a Favre filtered quantity evaluated on the CMC grid. In Eq. 3.19 N is the scalar dissipation rate, S_c is the source term from the RPV, $\dot{\omega}$ is the chemical species reaction rate and u_i is the velocity. Each of these variables are conditionally averaged $(\cdot|\zeta)$ on the RPV when $(c = \zeta)$. Although the terms in the CMC equation do not change with Favre density weighted filtering, the RPV equation will differ after filtering. The filtering introduces a sub-grid scale term

for the diffusion of the c transport equation 2.13, written as

$$\frac{\partial(\bar{\rho}\tilde{c})}{\partial t} + \frac{\partial(\bar{\rho}\tilde{u}_i\tilde{c})}{\partial x_i} = \frac{\partial}{\partial x_i}\tilde{J}_i - \frac{\partial}{\partial x_i}J_i^* + \rho\dot{\omega}_c \tag{3.20}$$

where $\tilde{J}_i$ is the resolved diffusive flux of c, defined as $\tilde{J}_i = D\frac{\partial\tilde{c}}{\partial x_i}$, and J_i^* is the sub-grid diffusive flux defined by

$$J_i^* = \bar{\rho}(\widetilde{u_j c} - \tilde{u}_j\tilde{c}) \tag{3.21}$$

The contributions to mass fraction from the smallest scales are approximated by J_i^* and are unclosed. J_i^* is modeled with a turbulent diffusivity D_t and a gradient transport model (or mixing length model), where $D_t = (C_D\Delta)^2||\tilde{S}_i j||$. The CMC equation is thus solved by following the discussed solution procedure, but models are needed for the SGS fluctuations of RPV, variance, scalar dissipation rate, and velocity. SGS closures are readily available for velocity and are well developed. Typically, a turbulent viscosity model is used to resolve the sub-grid scale stress tensor as discussed in section 2.2.3. The remaining sub-grid scale fluctuations are modeled by a gradient approximation for double moment terms, where the SGS variance of the c ($\widetilde{c_{sgs}''^2}$) is calculated by the solution to equation 3.3.

Note that in the Favre filtered version of Equation 3.3, the scalar dissipation rate has a SGS component. Closure of the unconditioned scalar dissipation in the literature is based primarily on existing methods for NP flows [61]. Accordingly, the NPCMC formulation for a conserved scalar is adopted in this work as in [57], even though a reactive scalar is used in PCMC. This simplification has been performed in a premixed CMC and DNS analyses [61], with adequate results. The unconditioned filtered scalar dissipation rate, in physical space, is closed as shown below,

$$\tilde{N}_c = C_{c2}\underbrace{\frac{\nu}{Sc}\frac{\partial\tilde{c}}{\partial x_i}\frac{\partial\tilde{c}}{\partial x_i}}_{Res} + \underbrace{\frac{\tilde{\epsilon}_{sgs}}{\tilde{k}_{sgs}}\widetilde{c''^2}}_{sgs}. \tag{3.22}$$

A more elaborate model for $\tilde{N}_c$, formulated for URANS, has been proposed by [2, 3] which

include the effects of the turbulent, chemical and molecular diffusion. The additional terms, representing the chemical and molecular diffusion of c, is inversely proportional to the Karlovitz ($\frac{1}{Ka^{0.4}}$) [2]. Under the well mixed assumption used in this work, Ka is large ($O(100)$), accordingly the inclusion of chemical diffusion is considered small compared to turbulent diffusion. This formulation accounts for both the resolved and sub-grid scale (SGS) components of the scalar dissipation rate, where ν is the laminar viscosity and Sc is the laminar Schmidt number. Formulations for a LES ϵ_{sgs} and k_{sgs} are provided in [29] and adopted in this work since they are model independent and ultimately dependent on the filter size, a SGS model constant and the velocity strain rate tensor $|S_{ij}|$.

To demonstrate the effect of the LES turbulence model on the flame shape an instantaneous image of the DLR flame is compared under a URANS and LES framework in figure 3.5.

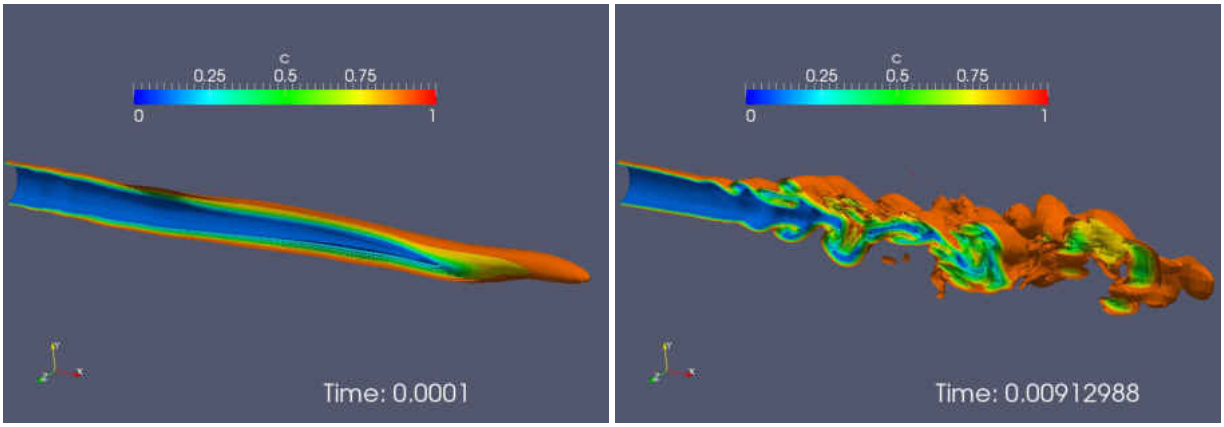

Figure 3.5: URANS (Left) and LES (Right) Instantaneous Contours of RPV

3.5 T-PCMC with Heat Loss

To keep the unconditioned species uncoupled from the flow equations, the effect of heat loss must depend on N, c, cVar and not directly on space. However, spatial heat loss effects can be accounted for in the burnt regime since there is no change in the tabulated values in this regime. Thus the heat

loss model is developed separately for two distinct regions. These regions are illustrated below in figure 3.6, where the colored region is "burning" region where the reaction zone exists and the remaining white portion is the "burnt" region. First the burning region is considered ($0 < c < 1$), in which the effects of heat loss are tabulated as a function of the conditional quantities. Second, the burnt region outside of the flame ($c = 1$) is described, which has a different spatial dependency with heat loss. In the burning region ($0 < c < 1$) the effect of heat loss directly alters the mean reaction rates and ultimately the species mass fraction as a function of c. In the burnt region ($c = 1$) the effect of heat loss solely alters the mixture temperature and density, but the species mass fractions remain constant, fixed at their burnt condition. This is a valid approximation, since when $c = 1$ the reaction is complete and the RPV source term, scalar dissipation rate and variance are all equal to zero.

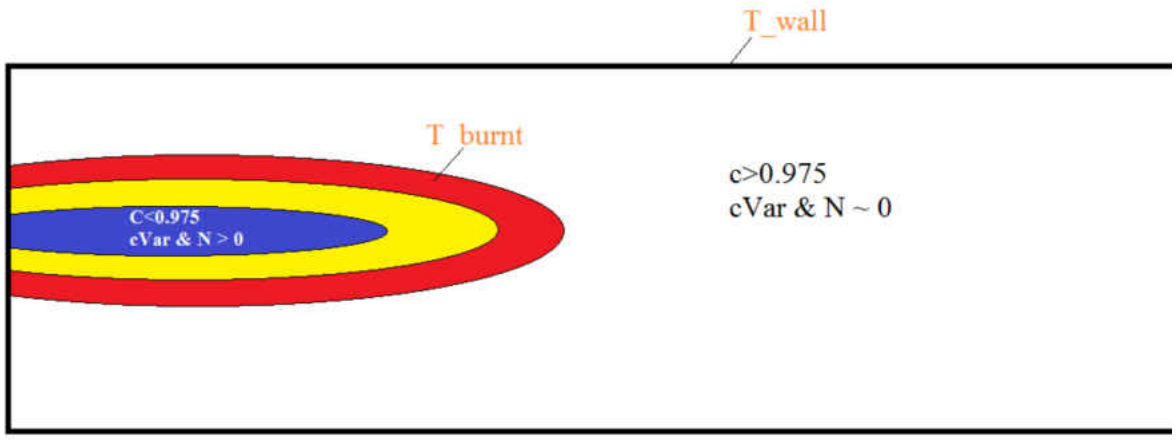

Figure 3.6: Flame Depiction of burnt and unburnt reaction regions

As in the adiabatic T-PCMC model (A-T-PCMC), the $c = 0$ and $c = 1$ boundary conditions must be defined for temperature, enthalpy and all of the species mass fractions in the mixture. In the case of the heat loss model these boundary conditions are also calculated, but the end sensible enthalpy, total enthalpy and temperature are altered by the effect of heat loss. Note that in the A-T-PCMC the total enthalpy was not needed at the boundaries since it was held constant and can not alter the value of c. To determine the end boundary conditions under heat loss a Perfectly Stirred

Reactor (PSR) model is employed under identical initial conditions and with the same chemical kinetic mechanism (GRI3.0).

The $c = 1$ boundary conditions discussed above are determined by solving a PSR solution with constant heat loss. The governing equation for species transport in a perfectly stirred reactor is provided below. In equation **??** $Y_{k,i}$ is the inlet mass fraction and $h_{k,i}$ is the inlet total enthalpy.

$$\frac{\partial h}{\partial t} = -\frac{\dot{m}_i}{\rho V}\sum_{k=1}^{k=ns}(Y_k h_k - Y_{k,i}h_{k,i}) - \frac{\dot{Q}_{loss}}{m} \tag{3.23}$$

Note that the change in enthalpy can be removed from the summation and $\frac{\dot{m}}{\rho V}$ can be written in terms of the the reciprocal of the residence time. With these two substitutions, equation 3.23 can be re-written as

$$\frac{\partial h}{\partial t} = -\frac{\Delta h_t}{\tau}\sum_{k=1}^{k=ns}(Y_k - Y_{k,i}) - \frac{\dot{Q}_{loss}}{m}. \tag{3.24}$$

From equation 3.24, it can be seen that the heat loss rate and residence time are inversely proportional. Such that an increase in $\dot{Q}_{loss}$ would require a decrease in τ for a fixed change in total enthalpy, the same is true if the solution is steady or transient.

By replacing the change in total enthalpy (Δh_t) with the definition of the RPV source term (Eqn. 3.29) a similar relation can be obtained between the RPV source term (S_c) and the heat loss rate ($\dot{Q}_{loss}$). Equation 3.25 shows that an increase in the heat loss rate would result in a decrease of the RPV source term to maintain a fixed change in total enthalpy ($\frac{\partial h}{\partial t}$). Since the scalar dissipation rate (N) scales with residence time, it is expected that an increase in N would also cause a decrease in the total heat loss transferred.

$$\frac{\partial h}{\partial t} = -\Big(\frac{\Delta hs}{2} - \frac{\sum_i \bar{\rho}\tilde{\omega}h_{f,i}}{2S_c}\Big)\frac{\sum_{k=1}^{k=ns}(Y_k - Y_{k,i})}{\tau} - \frac{\dot{Q}_{loss}}{m} \tag{3.25}$$

The PSR equation, allows for the transient solution of a flame under a constant heat loss rate for a given mixture and mass flow rate. For a fixed and long residence time (100 secs) the equilibrium

solution is obtained. This fact is demonstrated below in figure 3.7, which shows identical solutions for the RPV source term from both the equilibrium end boundary condition and the PSR end boundary condition at $\tau = 100\ [s]$ and $\dot{Q}_{loss} = 0\ [cal/s]$.

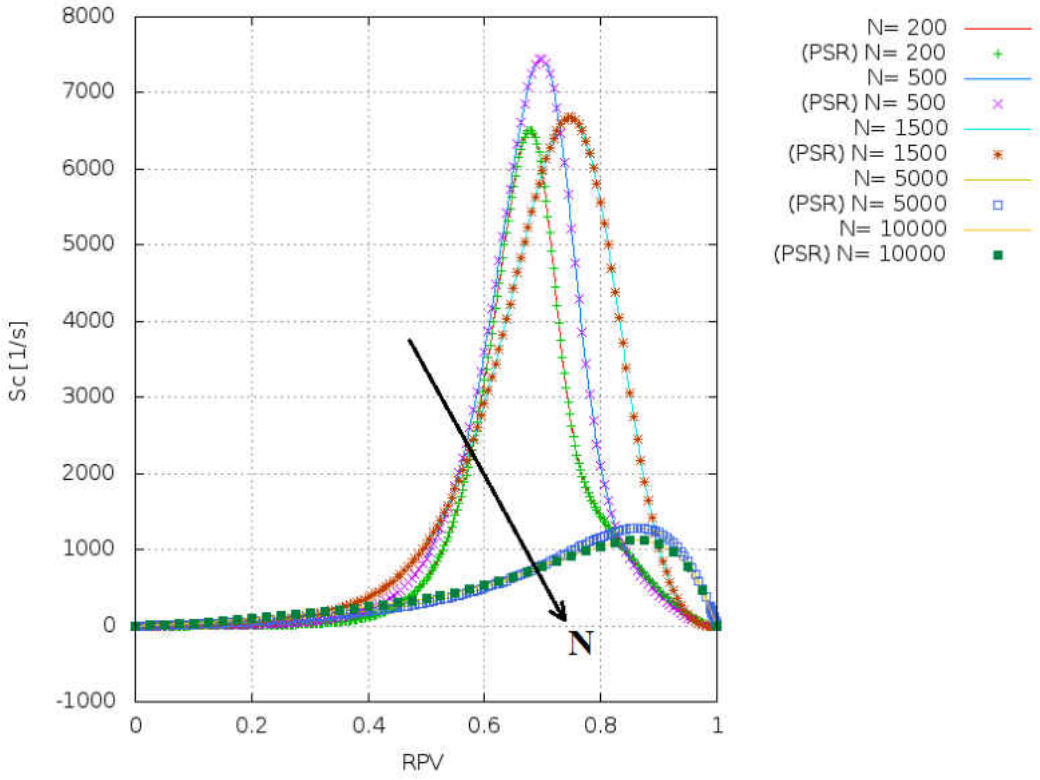

Figure 3.7: RPV Source Term for various N values. PSR:Symbol, Equilibrium:Line

By solving the PSR equation for a fixed steady state solution with heat loss, the $c = 1$ conditions may be prescribed before solving the T-PCMC equation to ensure a loss of total enthalpy must occur between $(0 < c < 1)$ and eventually meet the reduced exit total enthalpy.

This approach has the following advantages:

1. Y_i, h, h_s, T at $(c = 0)$ are the same for all $\dot{Q}_{loss}$.
2. $h, h_s, Tat(c = 1)$ changes for different $\dot{Q}_{loss}$.
3. $Y_i(c = 0)$ & $Y_i(c = 1)$ are the same for all $\dot{Q}_{loss}$.
4. $Y_i(0 < c < 1)$ changes for all $\dot{Q}_{loss}$
5. Sc(c) changes as a function of Q_{loss}.

6. $\dot{Q}_{loss}$ directly and physically alters the T-PCMC end conditions before solving.

7. If τ is reduced $Y_i(c = 1)$ will not reach its fully burnt condition.

By maintaining the temperature at the $c = 0$ condition, it is ensured that the inlet conditions of the mixture are maintained. It is important that the mass fractions at $c = 1$ are maintained at their equilibrium values and not a partially-burnt value. If a partially-burnt value is used at $c = 1$ then there can not exist fully-burnt species in the mixture, i.e., the entire exhaust would have a uniform partially-burnt value regardless of the mixing rate. Since combustors operating in the distributed regime will have high mixing and re-circulation, there must exist a condition in the field where the fuel is fully burnt since partially burnt products are reintroduced into the flame and allowed to finish reacting and reach their fully burnt condition. Thus, by maintaining the equilibrium species concentrations at the c=1 condition, at a reduced enthalpy, the solution ensures that a condition exists where there is a fully burnt mixture. It will be shown that the reduced exit enthalpies cause a reduction in the reaction source term (Sc) which slows the reaction rates allowing for faster velocity scales to advect the mixture downstream. In effect, lowering the exit total enthalpy creates a longer flame as expected under the effect of heat loss. With the change in sensible and total enthalpies at the burnt condition, the solution from the T-PCMC CFD model is directly altered by the amount of $\dot{Q}_{loss}$ prescribed, through a reduction in the source term (Sc). To avoid extinction or creating tables that do not include the full range of c, the steady state assumption is adopted in the PSR and $\tau = 100s$. This assumption is explained in more detail when the new RPV for heat loss is defined in equation 3.28.

To account for the effect of heat loss in the burnt regime, an additional temperature (burnt temperature) is calculated within the T-PCMC solver and stored in the T-PCMC table for the total range of total enthalpy experienced. The burnt temperature is calculated in conditional space and is integrated by the Beta function PDF and becomes a function of the variance and RPV in unconditional space. This burnt temperature range is distinct from the mixture temperature. The burnt temperature is computed for the same range of enthalpies experienced ($0 < c < 1$), except the

burnt mixture mass fractions ($Y(c = 1)$) are always used when calculating the mixture enthalpy and temperature at each value of c. This means the temperature is calculated assuming the mixture is always at the fully burnt species condition and the sensible and total enthalpy is allowed to change, for the full range of c, in the calculation of the burnt temperature set. This is consistent with the loss of temperature in the burnt region, due to a loss in enthalpy, at a fixed species concentration since this occurs outside of the reaction zone. To compare the burnt temperature profile, figure 3.8 below compares the burning temperature at various N with the burnt temperature as a function of the RPV.

It can be seen that the temperature progression as a function of enthalpy loss is similar for both the burnt and burning temperature profiles. Largest differences occur at $c = 0.5$ where the burnt temperature is approximately 4% lower when compared to the value of the burning temperature.

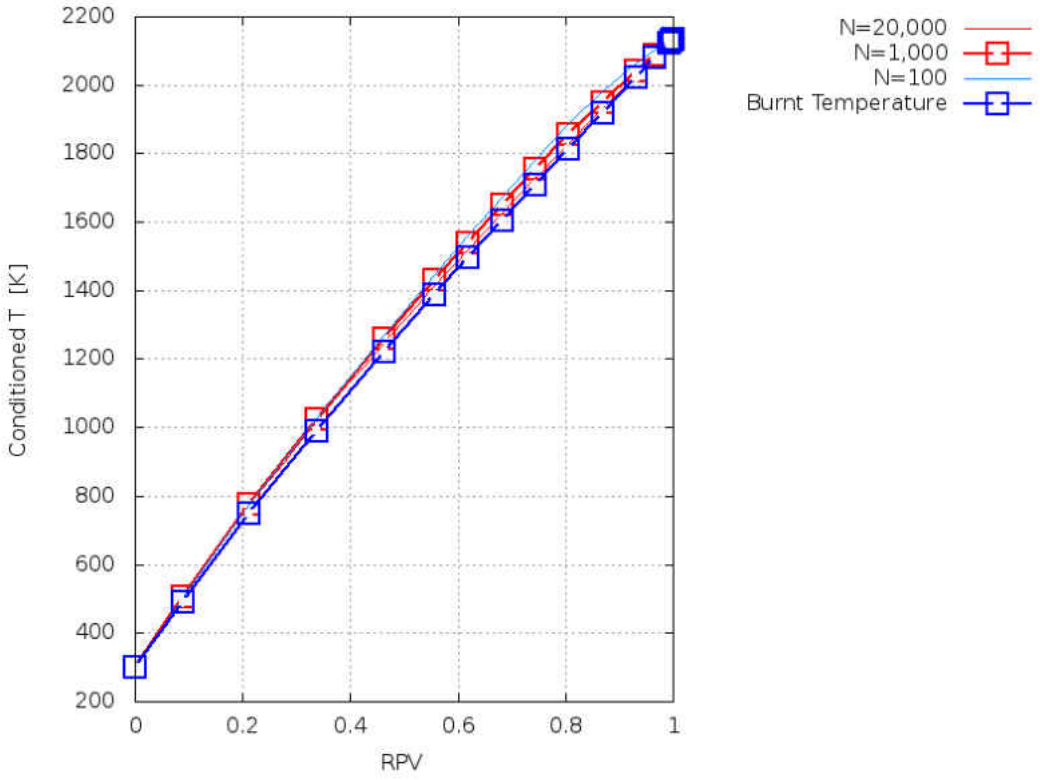

Figure 3.8: Temperature profiles for burning and burnt temperatures vs RPV

This burnt temperature data set is added to the T-PCMC table along with the change in total enthalpy which is used as an index, instead of c, to access the burnt temperature in the CFD solver.

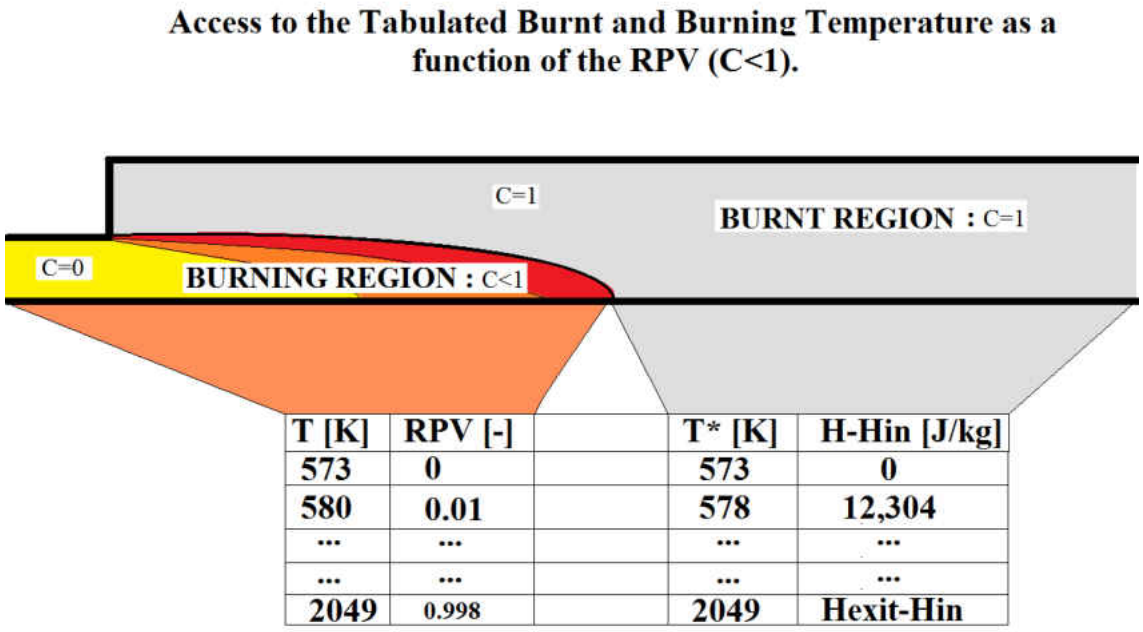

Figure 3.9: Illustration of the Burnt and Burning regions and their appropriate tabulated temperature.

In order to index the new burnt temperature data set from the T-PCMC table, as a function of total enthalpy loss, a 3-D transient total enthalpy transport equation is solved at every time step in the CFD. Once a solution is obtained for the total enthalpy field, the loss in total enthalpy is computed and used to index the correct burnt temperature from the T-PCMC table. The transport equation for the total enthalpy is defined as

$$\frac{\partial(\rho h)}{\partial t} + \frac{\partial(\rho u_i h)}{\partial x_i} + \frac{\partial(\rho K)}{\partial t} + \frac{\partial(\rho u_i K)}{\partial x_i} = -\frac{\partial p}{\partial t} + \frac{\partial}{\partial x_i}\Big(\frac{\lambda}{C_p}\frac{\partial h}{\partial x_i}\Big). \tag{3.26}$$

where, $K = \frac{1}{2}|U^2|$.

In the original definition of the RPV [55] , the RPV is written as

$$c = \frac{(h^s - 2h) - (h^s_u - 2h_u)}{h^s_{b,ad} - h^s_u - 2h_{ad} + 2h_u}. \tag{3.27}$$

In this formulation c becomes greater than unity with a loss in total enthalpy since the denominator maintains the adiabatic change in total enthalpy, which is zero. If the RPV were greater than unity, the Beta function PDF integration would no longer be valid since the Beta function PDF requires that $0 < c < 1$.

It was found that when attempting to solve the T-PCMC equations, with RPV ranges greater than unity, the equations became more difficult to solve numerically. At RPV greater then unity the T-PCMC equations stiffened which made convergence at low values of N ($N < 50$) very difficult to reach with the TWPBVP solver. This could also be attributed to the requirement of a new closure for the conditional scalar dissipation rate. The original closure $\langle \tilde{N}|\zeta \rangle = 4 * c(1 - c)$ assumes the max value of c is one. This closure was modified to $\langle \tilde{N}|\zeta \rangle = 4 * c(c_{max} - c)/c^2_{max}$, which scaled the original closure to reach the same maximum value, with a parabolic profile, even when $c_{max} > 1$. It is apparent that solving the T-PCMC equation when $c_{max} > 1$ requires a new closure for the conditioned N, a new PDF shape function for the PDF integration and better numerics to solve the stiffer T-PCMC equations produced when $c_{max} > 1$.

For this reason, a new definition of the RPV is proposed which is better suited for cases where the total enthalpy is not constant and $c_{max} = 1$. The proposed non-adiabatic RPV is defined as

$$c = \frac{(h^s - 2h) - (h^s_u - 2h_u)}{h^s_{exit} - h^s_u - 2h_{exit} + 2h_u} \tag{3.28}$$

Note that in equation 3.28 the denominator includes the exit total and sensible enthalpies and not the adiabatic or equilibrium values. The exit enthalpies are calculated based on the PSR solution, for a given $\dot{Q}_{loss}$. Since the exit total and sensible enthalpies will change based on a given heat

loss rate, each table will adjust to maintain $0 < c < 1$. This allows for the same conditional scalar dissipation rate profile to be used since the same bounds of RPV are still maintained. Moreover, this method allows for the continued use of the Beta function PDF which requires that $0 < c < 1$. The exit total enthalpy is altered directly by $\dot{Q}_{loss}$. The user can define $\dot{Q}_{loss}$ if the net heat loss rate of the flame is known or the user can iterate through different $\dot{Q}_{loss}$ solutions to determine the appropriate $\dot{Q}_{loss}$ to reach the expected exit temperature, which is below the adiabatic temperature.

The new definition for the RPV results in identical transport equations for c (Eqn. 2.33) and c''^2 (Eqn. 2.34) except that the definition of S_c is altered. The RPV source term is altered by the addition of the change in total enthalpy in the denominator and is re-written as

$$\tilde{S}_c = \frac{[\sum_i \bar{\rho}\tilde{\omega}h_{f,i}]}{\Delta h^s_{ex-u} - 2\Delta h_{ex-u}}. \tag{3.29}$$

The RPV and SGS variance equations are implicitly altered since the tabulated value for Sc, which is used in both RPV and SGS variance equations, accounts for the new denominator presented in equation 3.29.

The following changes were required to convert the adiabatic T-PCMC model to the non-adiabatic version.

1. Use the PSR solution, for a given $\dot{Q}_{loss}$, to define the burnt ($c = 1$) species and thermodynamic conditions.

2. Include the change in total enthalpy in the denominator of the RPV (Equation 3.28) and the RPV source term 3.29.

3. Use the new definition of c and the species mass fractions to calculate the change in sensible enthalpy to compute the burning temperature.

4. Calculate and tabulate a burnt temperature as in step 3, except hold the mass fractions con-

stant at the exit conditions for the whole range of total enthalpies.

Notice that the equations and framework in the CFD portion of the T-PCMC model remain unchanged. The change in c due to heat loss is accounted for implicitly in the CFD equations by the new $\tilde{S}_c$, which is looked up from the non-adiabatic T-PCMC table.

3.6 Heat Loss Analysis

To determine an adequate heat loss for the simulations and to better understand the effect of heat loss on the reaction, the solution from the T-PCMC equation is plotted and described in this section. Note that the following quantities are conditional and are only a function of scalar dissipation rate (N), the RPV and heat loss ($\dot{Q}_{loss}$), i.e., they have not be integrated by the PDF to unconditioned quantities. This demonstrates that the effect of N and $\dot{Q}_{loss}$ is incorporated before the T-PCMC equations are solved which are not considered *ad hoc* methods and maintains the coupling between N and $\dot{Q}_{loss}$.

The adiabatic solution for the conditional RPV source term and temperature are plotted below in figure 3.12 with varying scalar dissipation rate values ranging from 200[1/s] to 10,000[1/s]. The reaction source term reaches its maximum value between $c = 0.7$ and $c = 0.9$, note that increasing N decreases S_c and moves the max value towards higher values of c. In contrast, the temperature field is almost independent of the value of N. This is expected sense the mixture temperature is dependent on the mixture density, enthalpy and mean molecular weight of the mixture. These quantities are the net product of the individual species mass fractions and consequently are less influenced by individual species fluctuations in the mass fraction, as a function of N. Notice that both S_c and T reach their burnt values of $0[1/s]$ and $2049[K]$ respectively, independent of the value of N or the path taken in reaching the c=1 condition.

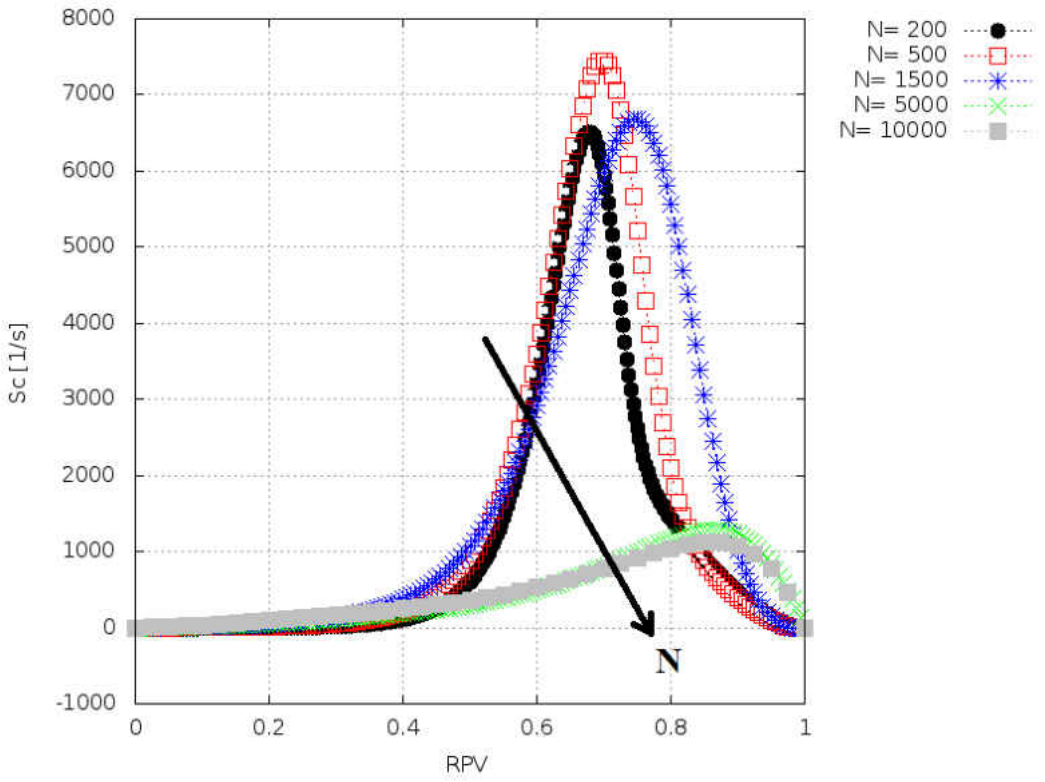

Figure 3.10: Adiabatic RPV source term versus RPV at various N ($\dot{Q}_{loss} = 0$).

Much in the same way that different values of N solely change the path of the solution and not the end conditions, it is expected that the effect of $\dot{Q}_{loss}$ will behave similarly even though $\dot{Q}_{loss}$ solely alters the $c = 1$ conditions. This allows the NA-T-PCMC equation to account for the effect of a global heat loss rate and changing N. In effect, $\dot{Q}_{loss}$ and N are coupled in the NA-T-PCMC model, this will be demonstrated in the following discussion. This effect is verified by plotting the RPV source term for various N as in figure 3.12, but with heat loss imposed. Figure 3.11 shows that the same values for N at different $\dot{Q}_{loss}$ resulted in a reduction of the RPV source term. Moreover, it appears that the reduction of S_c, due to heat loss, equally effects the high or low values of scalar dissipation rate.

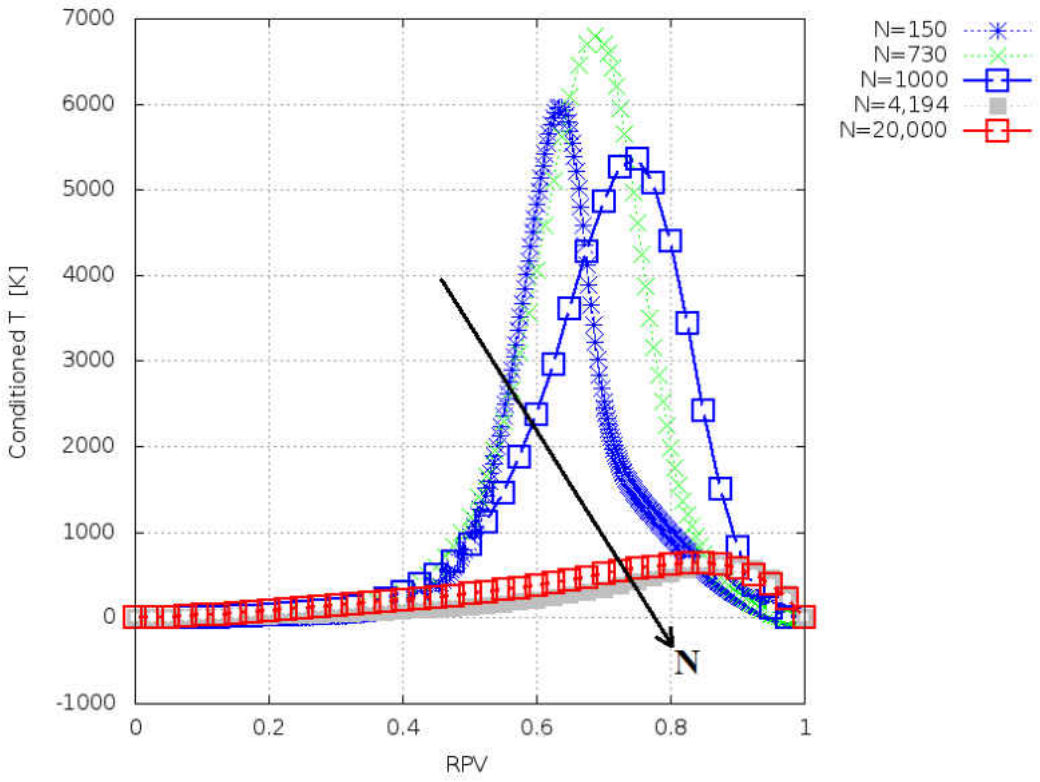

Figure 3.11: Non-Adiabatic RPV source term versus RPV at various N ($\dot{Q}_{loss} = 1.7$).

As previously discussed the PSR solution will depend on two controlling variables; the residence time (τ) and the heat loss rate. If residence time is small then the reaction will not have enough time in the combustion chamber to fully complete the reaction. Additionally, reduced residence times minimize the effect of heat loss since the mixture is exposed to the heat loss for a shorter duration of time. Since the heat loss rate is proportional to time, approximately a 10% reduction in the residence time would require a 10% increase in the heat loss to reach the same exit total enthalpy. This premise can be demonstrated by plotting the exit total and sensible enthalpies from the PSR solution for various residence times and heat loss rates.

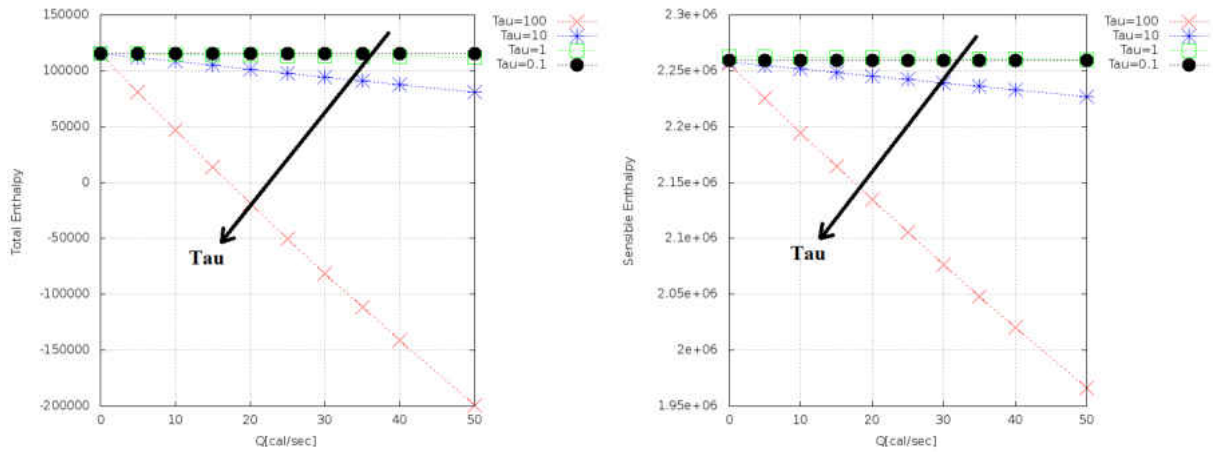

Figure 3.12: Total Enthalpy (left) and Sensible Enthalpy (Right) vs. Q : PSR solution for various τ $[s]$ & $\dot{Q}_{loss}$ $[cal/s]$.

Figure 3.12 shows the solution to various PSR solutions, each data point is the exit condition of a single PSR solution under different residence time and heat loss rates. Figure 3.12 demonstrates the above statement that the same exit total or sensible enthalpy can be reached at various different combinations of τ and $\dot{Q}_{loss}$. Each path is physically valid but represents a different flow rate (τ) and heat loss ($\dot{Q}_{loss}$). As stated above it is desirable to have the $c = 1$ condition represent the fully burnt conditions so that the CFD solution is not void of fully burnt concentrations. For this reason a τ of 100 seconds is used to generate the NA-T-PCMC tables, since it allows the mixture concentrations to reach their fully burnt conditions while being able to lower the temperature, sensible enthalpy and total enthalpy at the $c = 1$ condition.

If figure 3.12 is re-plotted with the progress variable in place of $\dot{Q}_{loss}$ as the x axis, the same conclusion is met as illustrated in figure 3.13. Note that RPV can only be computed for large values of the RPV, near the exit conditions as in a PSR. Figure 3.13 shows again that the sensible and total enthalpies can be changed for various τ and $\dot{Q}_{loss}$ combinations and the same rate of change with respect to the RPV is maintained. This shows that each path is physically valid and consistent with the changes in enthalpy or species mass fractions as a function of the progress variable. Moreover, it is evident from figure 3.13 that the same values for exit enthalpy can be obtained by multiple

different combinations of the residence time (TAU) and $\dot{Q}_{loss}$. Note that the heat loss rates in figure 3.13 are the same as those in figure 3.12, the only difference is that the range of $\dot{Q}_{loss}$ lowers the max value of c for a given residence time. This shows that heat loss can directly alter the maximum RPV value and this influence by heat loss increases with increasing residence times ($\tau > 1$).

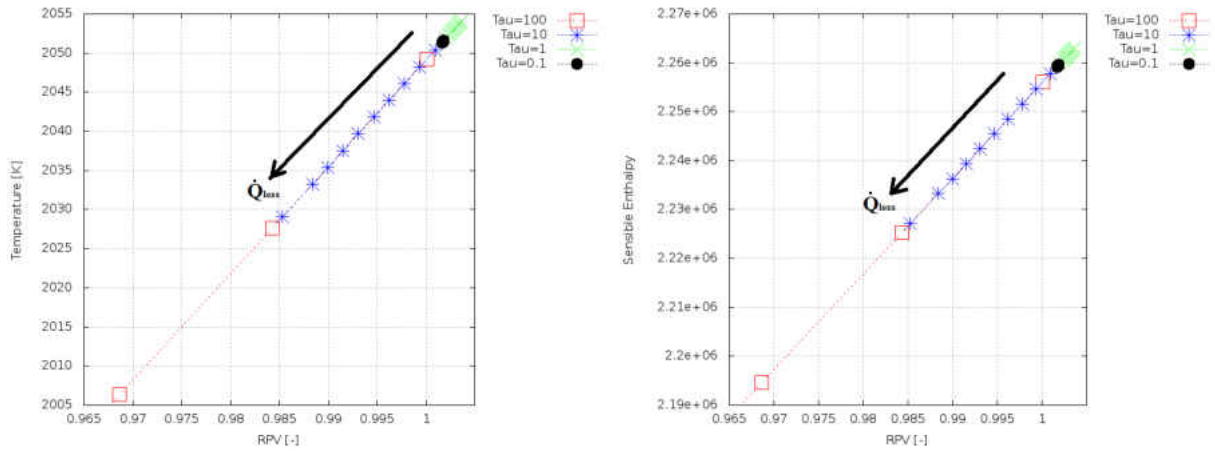

Figure 3.13: Temperature [K] (left) and Sensible Enthalpy [J/kg] (Right) vs RPV: PSR solution various τ $[s]$ & $\dot{Q}_{loss}$ $[cal/s]$.

To determine the coupled effect of $\dot{Q}_{loss}$ and N, the conditional CH_4 mass fraction, CO_2 mass fraction, total enthalpy and the RPV source term are plotted as a function of RPV for various $\dot{Q}_{loss}$ and N values from the solution of the T-PCMC equation. Figure 3.14 shows solutions of the total enthalpy for a range of heat loss values and at two distinct values of N. The low N solution plot on the left of figure 3.14 has a N value of 149 [1/s]. The high N solution plot on the right of figure 3.14 has a N value of 20,000 [1/s].

Figure 3.14 shows that at low N the effect of heat loss is less progressive and only alters the solution past $c = 0.6$. At high N the change in total enthalpy occurs for the whole range of c, even though the same end conditions are maintained, thus the heat loss and scalar dissipation rate are strongly coupled. It is hypothesized that the increase in scalar dissipation helps to distribute the flame properties by enhance mixing. In this view, an increase in N results in more uniform differences between the solutions from various $\dot{Q}_{loss}$.

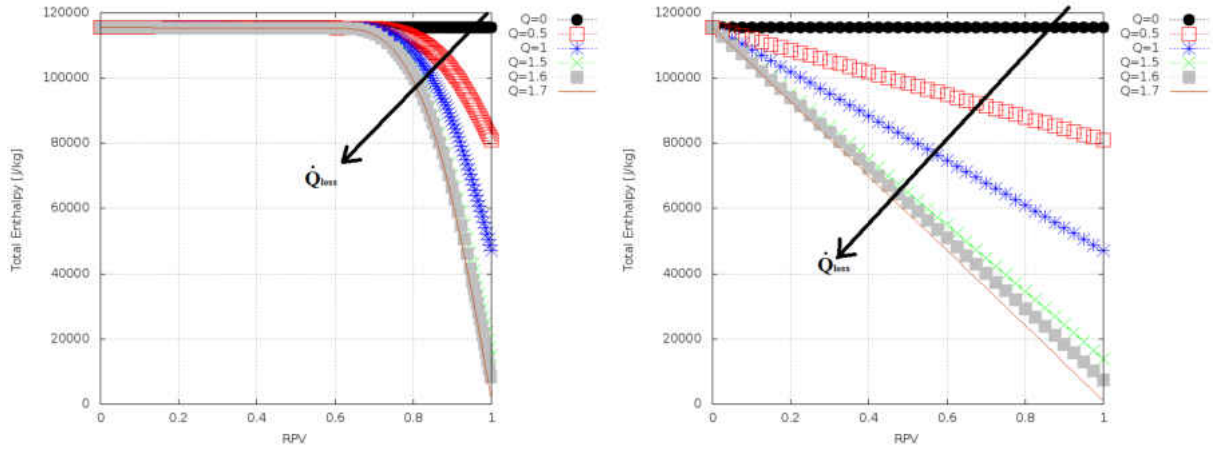

Figure 3.14: Total Enthalpy vs RPV: NA-T-PCMC solution at N=149[1/s] (left) and N=20,000[1/s] (right) with $\tau = 100s$.

Looking at the same comparison for the RPV source term in figure 3.15 shows a similar behavior with an interesting conclusion. Figure 3.15 shows that again the effect of heat loss is less significant at low N. Moreover, it is evident now that an increase in N and $\dot{Q}_{loss}$ result in a reduction of RPV source term (S_c).

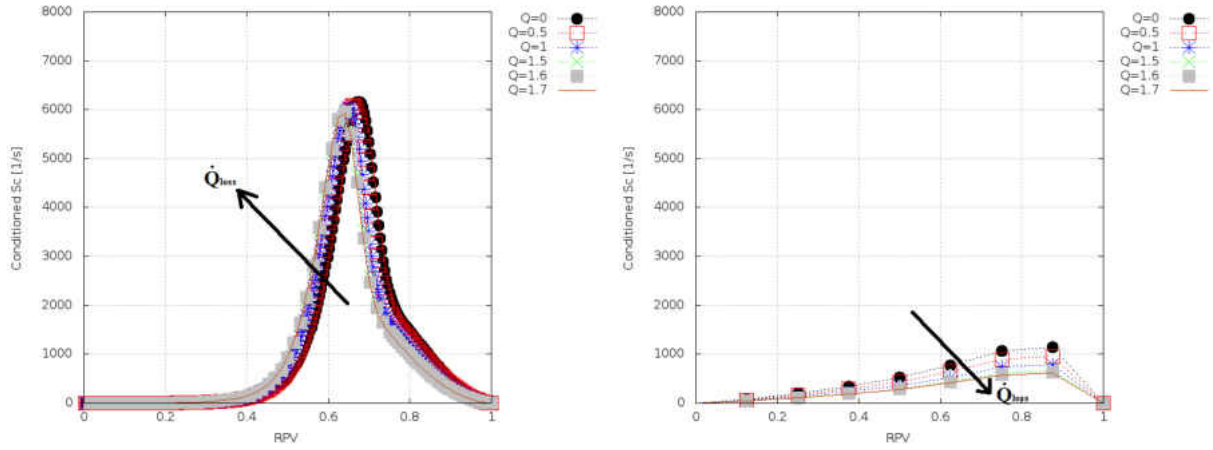

Figure 3.15: RPV Source Term vs RPV: NA-T-PCMC solution at N=149[1/s] (left) and N=20,000[1/s] (right) with $\tau = 100s$.

The reduction in S_c makes physical sense, since both an increase in N and $\dot{Q}_{loss}$ results in an

increase in the heat release rate of the flame. N represents the increase in the heat convection rate due to thermal diffusion at the small scales and $\dot{Q}_{loss}$ accounts for radiative and conduction heat losses to the surroundings. This concept is illustrated below in figure 3.16.

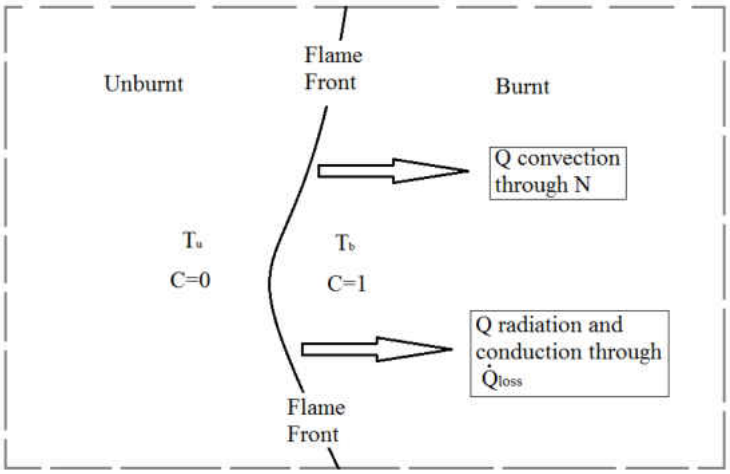

Figure 3.16: Flame front under diffusive and radiative heat losses

The same can be seen when plotting the CH_4 and CO_2 mass fraction which are plotted in figures 3.17 and 3.18.

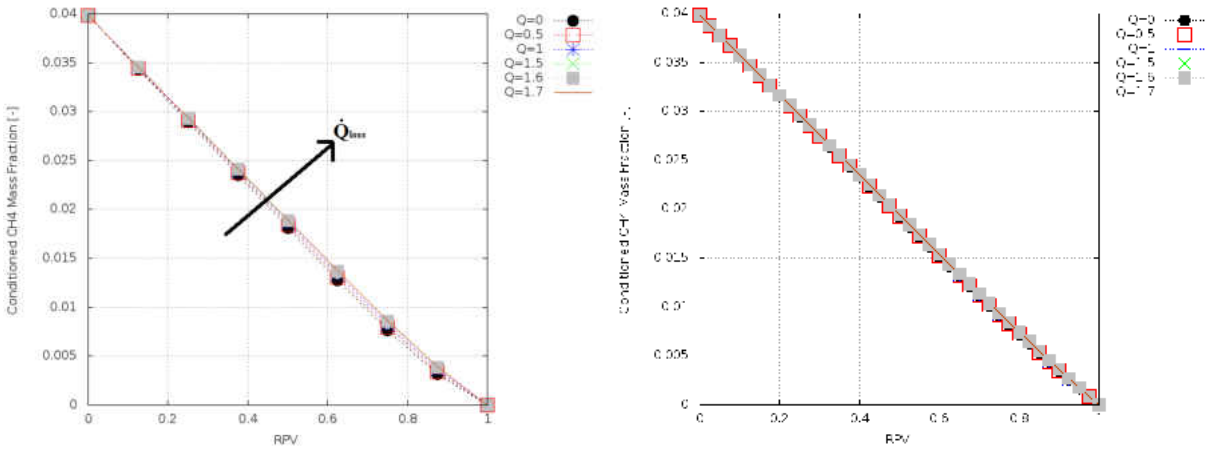

Figure 3.17: CH_4 Mass Fractions vs RPV: NA-T-PCMC solution at N=149[1/s] (left) and N=20,000[1/s] (right) with $\tau = 100$ [s].

Figures 3.17 and 3.18 show that increasing $\dot{Q}_{loss}$ or N results in a slower consumption of CH_4, slower production of CO_2 and accordingly the rate of the reaction is reduced with respect to a change in the RPV. These results indicate that it may be feasible to account for the effect of heat loss through the value of N. Validation cases are still required to prove the change in $\dot{Q}_{loss}$ is always proportional to a change in N. Once proven a new term may be added to the conditional scalar dissipation rate to account for the effect of heat loss on the reactions.

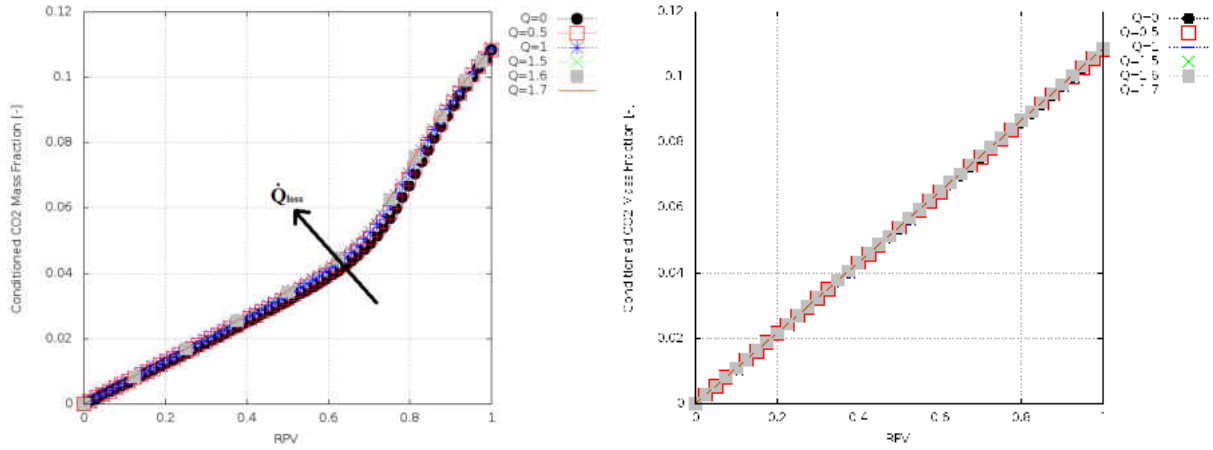

Figure 3.18: RPV Source Term vs RPV: NA-T-PCMC solution at N=149 [1/s] (left) and N=20,000[1/s] (right) with $\tau = 100$ [s].

To further demonstrate that various combinations of $\dot{Q}_{loss}$ and N can lead to identical solutions from the T-PCMC equation. The sum of the RPV source term is plotted for the entire range of c in figure 3.19. Note that in figure 3.19, the solutions from two different N and $\dot{Q}_{loss}$ rates show almost identical behavior. This summation of the RPV source term shows that the net change in energy is equivalent for different combinations of $\dot{Q}_{loss}$ and N.

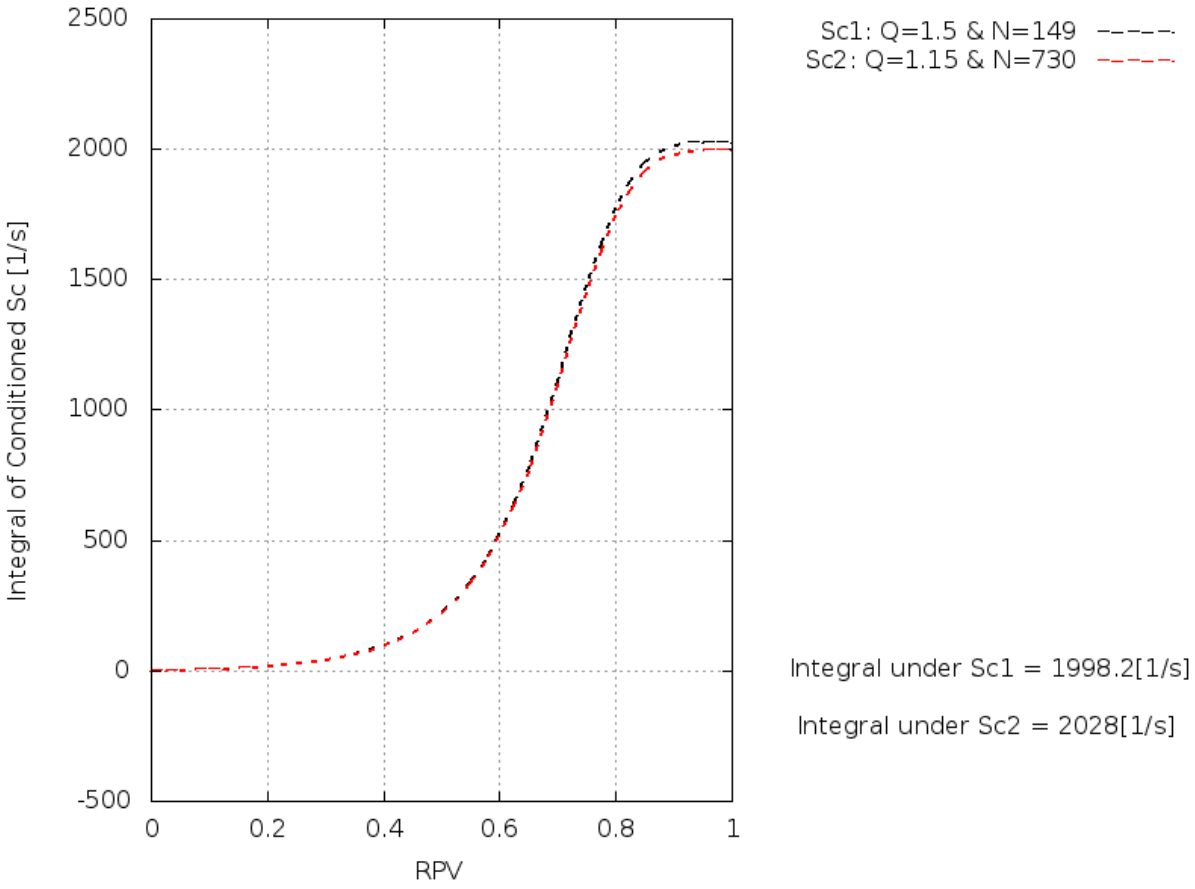

Figure 3.19: Sum of the RPV Source Term vs RPV for two different τ and $\dot{Q}_{loss}$ combinations.

CHAPTER 4: RESULTS

4.1 T-PCMC Model Validation

The proposed T-PCMC model is validated in this chapter against two different experimental data sets. The first data set provides qualitative results of time averaged contour plots of a lean reacting methane flame through a backward facing step. The second data set is from the DLR research group and includes detailed measurements of a LPM combustion chamber running at lean conditions for a methane and hydrogen flame. More detail will be provided on the experimental configurations in the following sections. At this point it is important to note that both flames are acted upon by a strong re-circulation zone which mixes partially burnt products with incoming unburnt fuel. This feature is expected to be in the distributed reaction regime, for which the T-PCMC model is applicable, and serve as excellent cases to validate the NA-T-PCMC model.

4.2 Backward Facing Step Case

4.2.1 Experimental Flame Measurements

A wind tunnel is used to drive a premixed methane air/fuel mixture through a backward facing step enclosure. The enclosure has a width of 157 mm, height of 40 mm and a length of 520 mm. Natural gas (94% CH_4) is pressurized upstream of the test section until a mass flow rate of 125 kg/h is reached. Although three equivalence ratios are presented in the experimental work [24], an equivalence ratio of 0.9 is chosen for its abundance of data when compared to the other two equivalence ratios. The step height is 20 mm, exactly half of the height of the enclosure, producing a sudden expansion for the upstream pipe flow. This sudden expansion raises the turbulence of the mixture to promote combustion while creating a separation region, in front of the step, to stabilize the flame structure so that it may burn downstream. Additionally, measurements were

performed with a smaller step height of 10mm to analyze the effect of the step height on the flame structure and species predictions. The Reynolds number at the inlet plane is approximately 1.35 X10^4; for internal flow this is considered highly turbulent. Averaged temperature, velocity, and species concentrations for CO, CO_2 and unburned hydrocarbons are measured using a laser Doppler anemometer. For more information on the details of the measurements provided refer to [24]. For validation of the T-PCMC model, temperature, CO, CO_2 and UHC's fields are used for comparison. Additionally, the RMS of the axial velocity is used to compare against the CFD T-PCMC predictions of the transient history of the flow. Contour graphs of the experimental results are taken directly from the [24] and compared, side by side, to identical contours from the CFD results.

4.2.2 CFD Case Description

An unstructured mesh is used to discretize the domain of the the backward facing step section with approximately 800k cells. The computational domain length is shortened to match the experimental window. This allowed for good resolution with a relatively low cell count. Four different mesh sizes ranging from 800k-2,300k cells were tested and it was found that results showed relative mesh independence even with the coarsest mesh. The mesh is composed mostly of Hexahedral (hex) cells, with the addition of few Tetrahedral (tet) cells introduced at the interface between coarse and fine cell levels. Inserting tetrahedral cells above the height of the boundary layer allowed for twice the cell refinement of the boundary layer. In conjunction with an expansion ratio of 1.2 near the wall, the mesh is able to sustain a Y+ values of $O(1)$ along the top wall. The mesh for the backward facing step is illustrated below in figure 4.1.

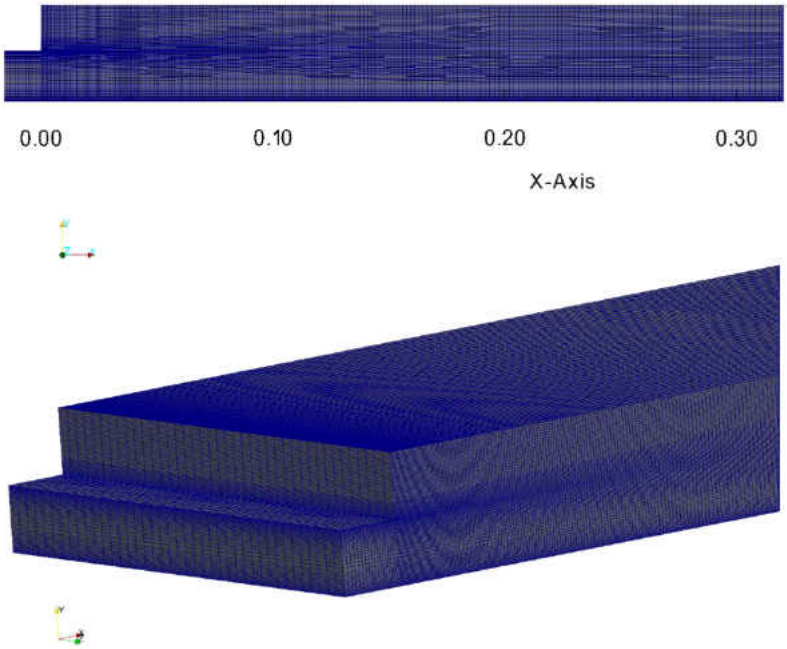

Figure 4.1: Backward Facing Step Computational Mesh

The bottom surface (longest) has a Y+$\approx$ 100 and employs a wall function for both the sub-grid scale (SGS) thermal diffusivity and compressible turbulent viscosity with approximated initial values based on the Reynolds number and the characteristic length scale of the large turbulent eddies (l_t). The compressible Smagorinsky LES turbulence model is used to model the SGS velocity fluctuations while the large scale 'energy carrying' eddies are directly resolved, traditional of LES filtering. Moreover, the employed SGS model assumes a local equilibrium at the filter size between the resolved and sub-grid velocity fluctuation scales. The implemented Smagorinksy model is not dynamic in that the Smagorinsky constant, C_s, is held uniform over the domain and set equal to 0.21. The SGS viscosity (μ_{sgs}) and thermal diffusivity (α_{sgs}) are modeled as

$$\mu_{sgs} = c_k \rho \Delta \sqrt{k_{sgs}} \tag{4.1}$$

$$\alpha_{sgs} = \frac{\mu_{sgs}}{P_{r,t}} \tag{4.2}$$

where c_k is a model constant set to 0.1, $P_{r,t}$ is the turbulent Prandtl number and k_{sgs} is the SGS turbulent kinetic energy which is modeled analytically, based on the velocity stress tensor, the model constant c_k and the filter size, Δ. The 3-D low Mach Number version of OpenFOAM [68] is employed to solve the coupled pressure-velocity equations from the discretized momentum equation. Here the Mach number is low enough that compressibility effects are negligible and the velocity is large enough that buoyancy effects are negligible. A Pressure Implicit Split Operator (PISO) algorithm [28] is used to solve the discretized momentum equations in time and space.

A velocity profile is imposed on the inlet matching the inlet profile (10.5 m/s) in figure 4.2. Additionally, a random turbulent intensity of 2%, from the mean flow, was imposed on the inlet flow to sustain the turbulent energy and match the measured velocity root mean square just before the sudden expansion. A low turbulent intensity was chosen since the sudden expansion naturally provides sufficient turbulent kinetic energy generation for the remaining downstream flow. The reaction progress variable and its variance are set equal to zero at the inlet and the temperature is prescribed its unburned value of 300K. The outer walls have an imposed no-slip condition requiring the velocity to be equal to zero and a zero gradient condition for pressure, temperature, scalar dissipation rate, RPV and variance. The outlet pressure is set equal to atmospheric pressure and the zero gradient (Z.G.) condition is used for the remaining, above mentioned, variables. These external boundary conditions are depicted below in figure 4.2.

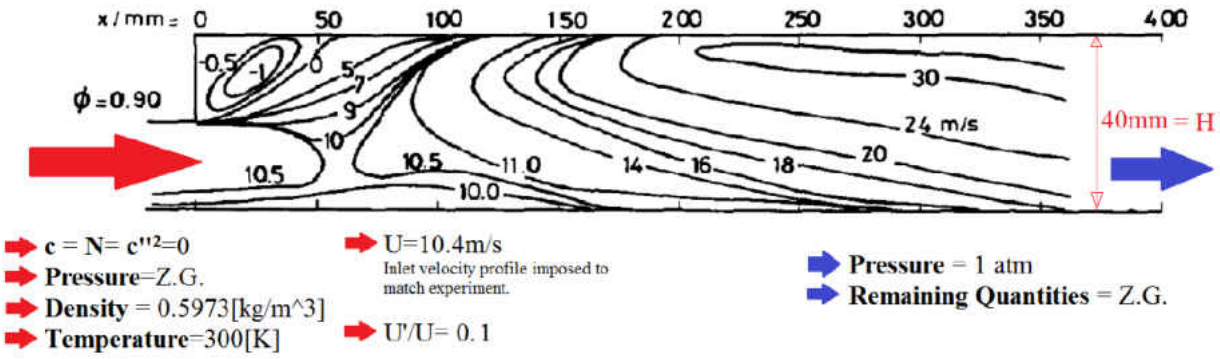

Figure 4.2: Schematic of Test Rig

To determine the approximate combustion regime of the methane flame under consideration, the premixed Borghi diagram is plotted below in figure 4.3 with values calculated by the CFD and T-PCMC results. Chemkin, with the GRI3.0 Mechanism [54], is used to calculate the flame speed, S_l, and the laminar flame thickness, l_f. The CFD code is used to calculate the velocity root mean square (RMS) of the flow field, u', along with the integral length scale of the large (energy containing) eddies, l'. Expressions for the calculation of l' are available for RANS and URANS turbulence models due to the existence of a resolved turbulent kinetic energy (k_{res}) and a resolved turbulent dissipation rate (ϵ_{res}). In the case of LES, these values are not available and typically algebraic models for the integrated length scale are used. Instead, as in [29], l' is approximated by multiplying the resolved RMS velocity fluctuations by the mixture diffusion. i.e. $l' = \frac{u'}{D}$. Where the diffusion, D, is represented by the magnitude of the resolved strain rate, $|S| = \sqrt{2S_{ij}S_{ij}}$. The deformation gradient tensor, S_{ij}, is solely dependent on the velocity field which removes any dependencies on the chosen LES model. Once the four values (u', l', S_l and l_f) are calculated they are filtered on the condition that c is between 0.05 and 0.95. By removing the values of c outside of the flame zone, the scattered data u'/S_l and l'/l_f is ensured to solely represent the reaction regime within the flame! Traditionally, the inlet boundary conditions are used to make rough, single point estimates of the flame's combustion regime. It is evident from figure 4.3 that even within the flame zone ($c = 0.05 - 0.95$) there are multiple combustion regimes occurring. The flame resides mostly within the corrugated and wrinkled flamelet regimes where Karlovitz number is less than unity. Additionally, it can be seen that there are occurrences of the thin reaction regime. In this regime the flame thickness is larger then the SGS and Kolmogorov length scales which allow for these small eddies to enter and alter the flame structure.

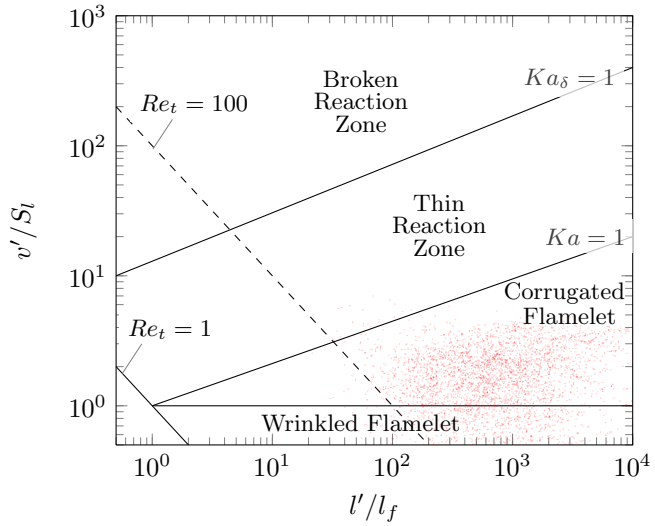

Figure 4.3: BORGHI DIAGRAM: COMPUTED FROM CFD IN FLAME ZONE
$(C = 0.05 - 0.95)$

The simulation time step is of the order of a micro second, but is allowed to loosely adjust based on the requirement that the Courant number remains below 0.5. Lowering the Courant number limit from 1 to 0.5 stabilized the solution and is suggested for reacting LES cases.

Every time step the density, temperature and source term (for the enthalpy equation) are looked up from the T-PCMC table and every two time steps the species of interest (Y_i) are looked up from the table. A second-order backward euler implicit time marching scheme is used for all of the variables and a third order cubic scheme is used for the divergence, laplacian, gradient, and interpolation operators of the discretized equations and field values in physical space. The model constants for the closure of terms (cVar4$_i$,cVar5$_i$) in Eq. 2.34, C_{c1} and C_{c2}, are 0.715 and 8.00, respectively. These values have been adjusted in comparison to the theoretical values of 2.86 and 2.00, since the theoretical values are derived based on non-reacting flow. The use of these (non-reacting) theoretical values resulted in large values of the variance, giving a lower flame temperature and larger flame thickness. It was evident from the initial values that there was an overproduction of variance, limiting the values was performed once and has performed well for multiple LES models with different geometries and boundary conditions. LES models have shown

a weaker dependence on the values for CC1 and CC2 in comparison to URANS. This is due to the fact that LES T-PCMC model uses the SGS versions of turbulent kinetic energy, k, and turbulent dissipation rate, ϵ, to determine the turbulent time scale. The SGS components of k and ϵ are used since "real" molecular diffusion occurs at the Kolmogorov length scale. For typical mesh sizes, as well as this mesh, the Kolmogorov length scales exist entirely within the SGS and thus fluctuations of this scale and consequently the molecular diffusions are modeled and not resolved.

Even with LES turbulence g and detailed chemistry, model run times are comparable to non-reacting CFD simulations. The mean and variance results are based on approximately 5000 sequential time steps over a period of 1 second of simulation time. It takes approximately 0.04s for the mixture to flow through the entire domain, thus there are 25 flow-thru times simulated for the calculation of the mean and variance values. The simulation is allowed to run for 3 flow cycles before the average begins taking sample, thus the average is taken over the last 22 flow cycles. The results produced statistically independent fields and were deemed stable. The simulation was performed in parallel on four Xeon E5650 hex-core processors with 24GB of RAM for 11 hours. The runtime is an order of magnitude reduction when compared to traditional CMC runtimes where the CFD and CMC equations are both solved simultaneously.

4.2.3 Results and Analysis

The contour plots of the mean temperature, axial velocity, carbon monoxide (CO), carbon dioxide (CO_2) and the unburned hydrocarbons (UHC) are shown to compare the predicted results from the both the adiabatic T-PCMC (A-T-PCMC) and non-adiabatic T-PCMC (NA-T-PCMC) model against the measured experimental results. The CFD data is mapped and compared to the contour plots in the experimental paper [24]. The results are scaled such that the two data sets can share the same axis' and units, for easy comparison of the simulation results to the measured data. The x and y axis' are displayed in units of meters. Each figure shows the results from the A-T-PCMC on top, the measured results in the middle and the NA-T-PCMC results at the bottom, so that both

the adiabatic and non-adiabatic solutions can be easily compared to the experimental contours. In all of the shown plots the contours are labeled and have similar contour levels as the experimental results, which are also labeled. For all of the contour plots, the top contour is the A-T-PCMC, the middle contour is the measured data and the bottom contour is the NA-T-PCMC result.

Figure 4.4 shows the mean temperature profile based on the LES results compared to experimental measurements. Overall agreement of the temperature trends and magnitudes is evident except for the re-circulation region. Since the CFD A-T-PCMC model is adiabatic all temperatures outside of the flame ($c = 1$) experience no heat loss and are equal to the adiabatic temperature of 1900K. This is an expected result and it is shown that accurate trends are found in the combustion regime ($c < 1$) farther from the heat loss effects of the wall which are not captured in the A-T-PCMC combustion model.

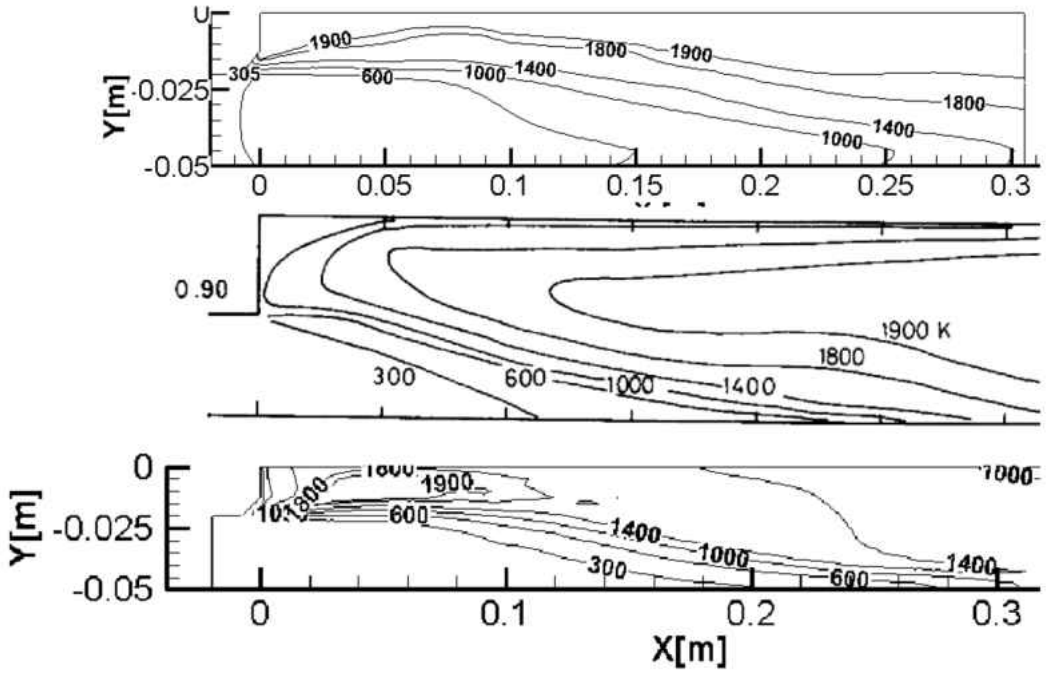

Figure 4.4: Mean Temperature [K]: A-T-PCMC (top), Measured (middle), NA-T-PCMC (bottom)

In contrast, the NA-T-PCMC model is able to predict temperature changes outside of the flame. In particular, the temperature within the re-circulation region is well predicted by the A-T-PCMC

model which accounts for the changes in total enthalpy due to the increased strain generated by the re-circulating eddies.

Figure 4.5 compares the contours of the measured and predicted mean axial velocity. The results show that the separation region and re-circulation zone in front of the step are both well predicted by LES. Aside from the second separation region, the magnitudes and locations of the mean axial velocity are well predicted. Note that both the experimental and CFD results show almost identical re-circulation lengths. This indicates LES is quite suitable for predicting the re-attachment length of the re-circulation zone which helps to stabilize the flame and direct the reactions downstream. Although the velocity field is well predicted by both the NA-T-PCMC and A-T-PCMC solutions, the NA-T-PCMC results show better predictions of the fastest velocity contours which are more slender then the A-T-PCMC results.

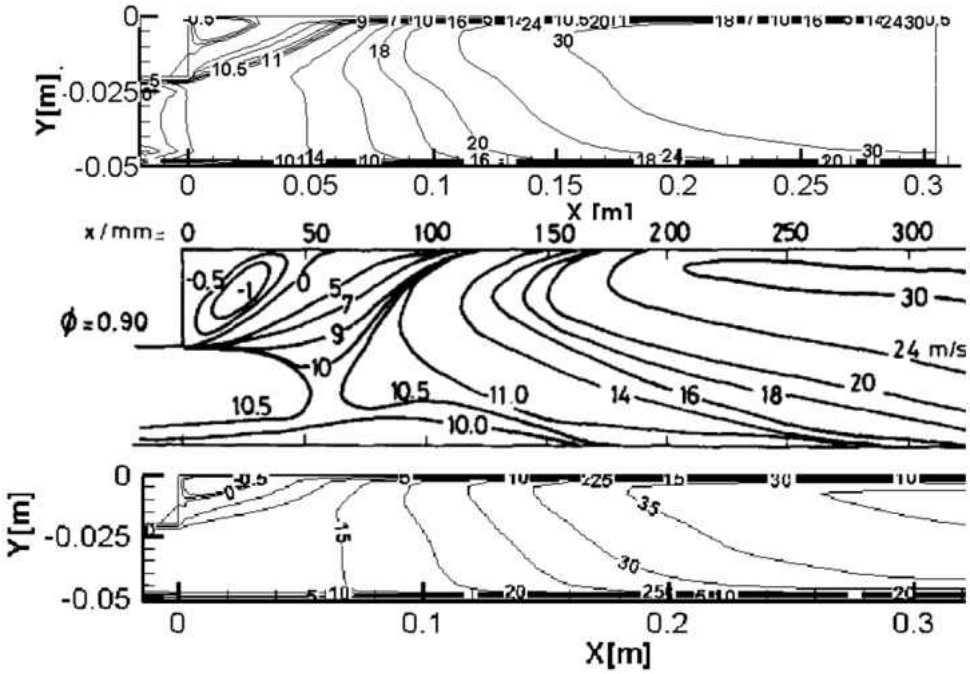

Figure 4.5: Mean Axial Velocity [m/s]: A-T-PCMC (top), Measured (middle), NA-T-PCMC (bottom)

To validate the T-PCMC model in predicting emissions of premixed flames, the CO, CO_2, and

UHC emissions are compared in figures 4.6, 4.7 and 4.8. The CO and CO_2 results for the volume concentrations are on a dry mole fraction basis with the removal of unburned hydrocarbons such as methane (CH_4) and ethane (C_2H_6) from the mixture fractions and total molar mass. The UHC volume concentration is wet. As in the other contour plots, similar contour levels are used between the T-PCMC results and the measured data for easy comparison.

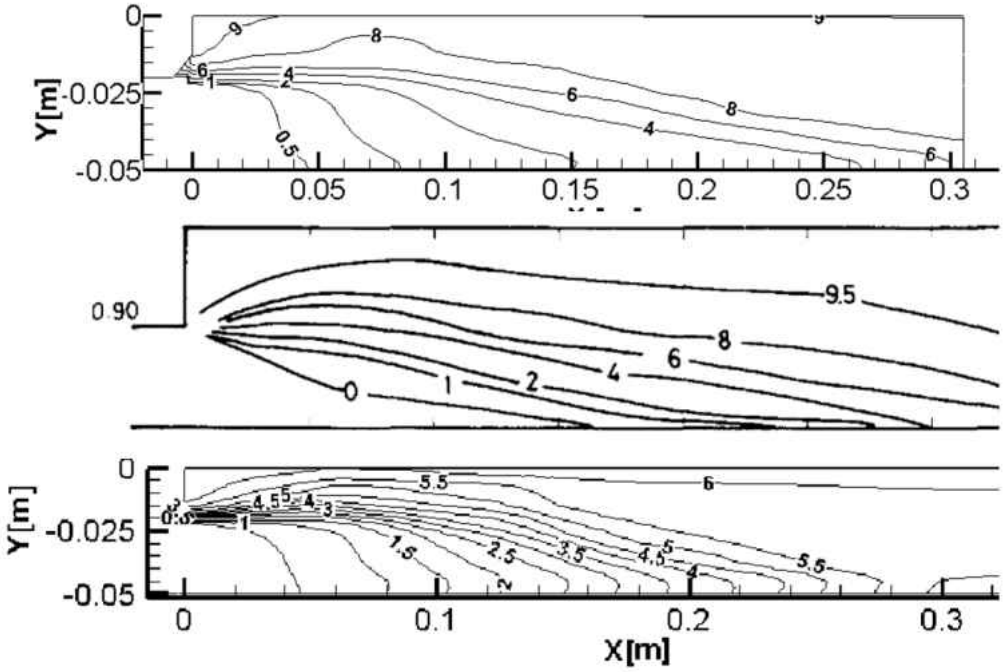

Figure 4.6: Dry CO_2 Volume Fraction [%] with UHC removed: A-T-PCMC (top), Measured (middle), NA-T-PCMC (bottom)

Figure 4.6 shows a good overall agreement with the magnitude and distribution of the resulting CO_2 in the burnt gases. The measured species concentrations are more spread out then in the predicted results, this indicates that there is an under prediction of the flame thickness compared to the experimental data. In the case of CO_2 there were larger differences between adiabatic and non-adiabatic solutions downstream of the step and near the step differences are small.

Figure 4.7 shows the results for the dry CO volume fractions. Here it is more evident that there are still reactions occurring along the top wall since there exist small concentrations of CO

in this region, which are not captured by the A-T-PCMC model. The adiabatic model will not predict this region since it exists outside of the flame surface and thus is considered fully burnt and prescribed the respective fully burnt (c=1) adiabatic value. In contrast the NA-T-PCMC model is able to predict the formation of CO at its downstream location in accordance with the measured results. In specific, the region of highest CO formation (CO=0.5%) is well predicted and exits the measurement regions ($x = 0.35m$) at almost an identical Y height when compared to the measured results.

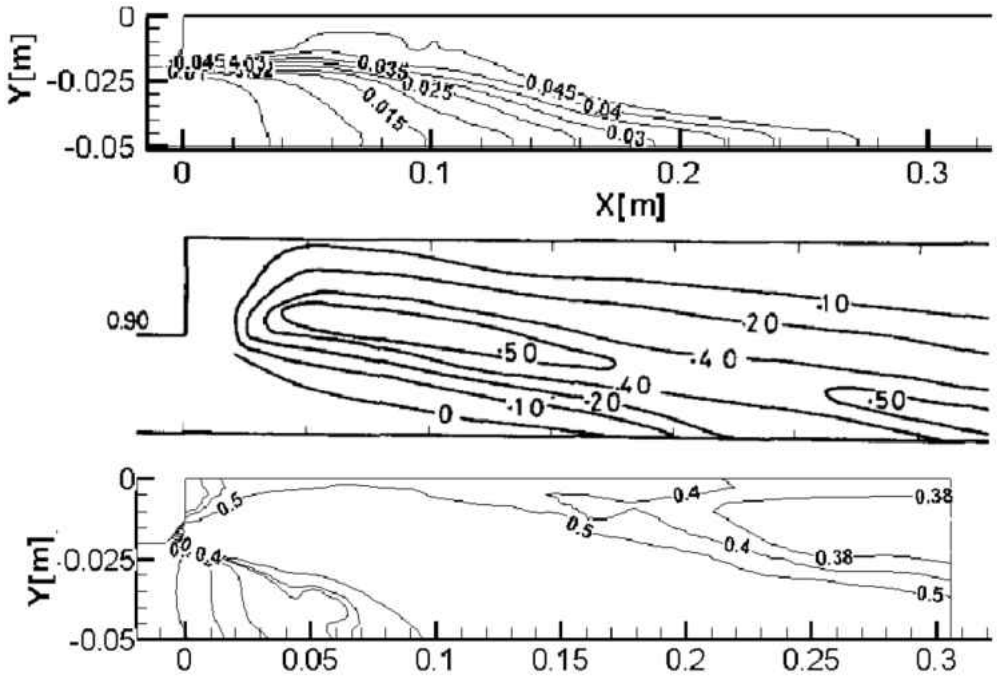

Figure 4.7: Dry CO Volume Fraction [%] with UHC removed: A-T-PCMC (top), Measured (middle), NA-T-PCMC (bottom)

To conclude the comparison of the 20mm step height case, the contours of the unburned hydrocarbons are compared to measurements in figure 4.8.

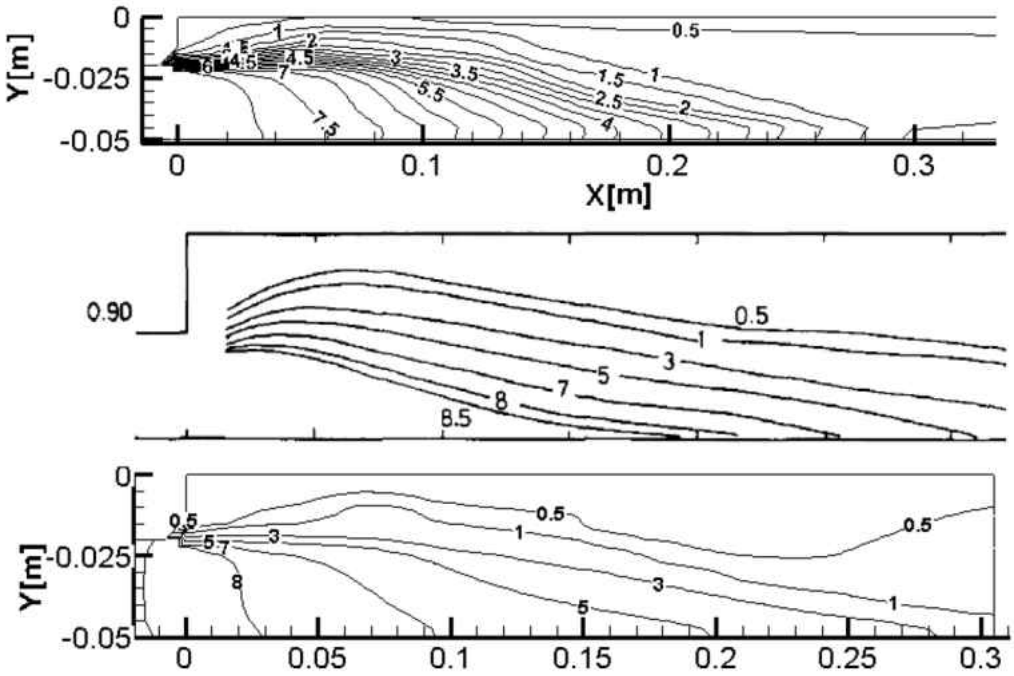

Figure 4.8: Dry Unburnd Hydro-Carbons (UHC) Volume Fraction [%]: A-T-PCMC (top), Measured (middle), NA-T-PCMC (bottom)

The predicted unburned hydrocarbons are in overall better agreement with the measured data when compared to those of CO and CO_2. This can be explained since HC's are abundant much earlier in the flame then the formation of other emissions such as CO and CO_2. Since the majority of HC's will react in the preheat zone of the flame, the UHC species are less influenced by heat loss to the surroundings of the flame. Still, evident by the smallest UHC values, the NA-T-PCMC model better predicts the exit values and locations of the 1 % and 0.5 % UHC when compared to the A-T-PCMC predictions.

The results have demonstrated that the heat loss effects are strong in the measured flame and that the adiabatic nature of the A-T-PCMC formulation is not well suited for this flame. None the less, good prediction of the velocity mean and RMS quantities are obtained. The results from the NA-T-PCMC solution show an overall improvement and provide a better match to the experimental results, specifically at downstream locations where the effects of heat loss are strong. Though

a much better prediction of the temperature field was obtained, only a slight improvement of the species concentrations was achieved. These results show a quantitative validation of the NA-T-PCMC model and have verified the coupling of LES turbulent quantities, with detailed chemistry and the inclusion of the small scale mixing effects have been demonstrated. To provide a quantitative validation of the NA-T-PCMC model, line plots from a more turbulent flame are provided in the following section.

4.3 DLR Jet Case

4.3.1 Experimental Flame Measurements

To compare the T-PCMC CFD results to experimental work, the DLR [21, 35] single jet premixed methane flame is chosen for simulation. Methane and air are premixed at an equivalence ratio of 0.71. The mixture is preheated to 573 K with an inlet velocity (V_{jet}) of 90 m/s and a Reynolds number of approximately 18,000. The Damkohler and Karlovitz values for the measured flame are not provided in the experimental work. The average Damkohler and Karlovitz numbers within the flame are approximately equal to 0.22 and 2.4, respectively. This would place the DLR flame in between the well-stirred and distributed reaction regimes.

The jet is offset from the center of the chamber such that a re-circulation zone will stabilize the flame and redirect burnt products downstream of the nozzle. The rectangular rig had optical access for PIV and laser Raman measurements of velocity and scalars, respectively. On the left side of figure 4.9, the dimensions of the test geometry are labeled for the single jet case. The inlet pipe diameter (d) is one centimeter ($d = 0.01m$) and is used to scale the dimensions of the domain on the left side of figure 4.9. On the right hand side of figure 4.9 are mean and instantaneous velocity fields captured by the experimental particle image velocimetry (PIV) [21].

The PIV data provides a 2.2 x 2.2 mm^2 spatial resolution. An uncertainty of 2.3 m/s in both ax-

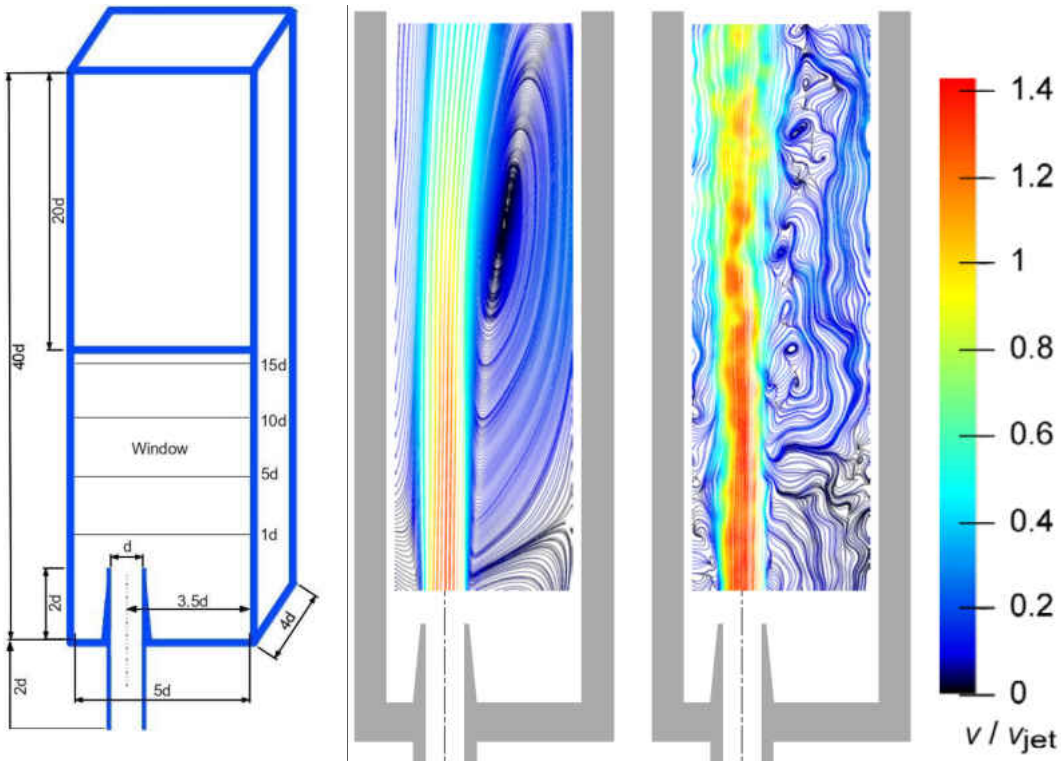

Figure 4.9: DLR combustion chamber dimensions (Left) and (Right) PIV mean and instantaneous velocity field

ial and vertical velocity measurements was reported and the Raman measurements of temperature and species concentration report an average 5% error in the flames used for calibration. Though not specified, it appears the data error of 2.3 m/s corresponds to the instantaneous velocity measurements, it is not specified how this would affect the error of the averaged results.

The inside diameter of the inlet nozzle is 10 mm. Measurements were performed at atmospheric pressure with the walls air cooled. The heat loss from the rig and wall temperatures were not reported and the measured peak flame temperature was approximately 200 K below the adiabatic flame temperature computed by the T-PCMC model. A recent numerical study [52] estimates the wall temperature to be approximately 1000 K. Comparing these estimates to the adiabatic fully burnt temperature, 2064K, demonstrates the presence of heat loss.

4.3.2 CFD Case Description

The CMC table lookup combustion model described in section 3.3 was added to the OpenFOAM CFD code as described in section 3.3 and used to model the experiments described in Ref. [35]. The open source CFD software OpenFOAM [68] was employed to solve the coupled fluid pressure-velocity equations along with the equations for $\tilde{c}, \tilde{c}''^2$ and $\tilde{N}$. Here the Mach number was low enough that compressibility effects were considered negligible and the velocity was large enough that buoyancy effects were negligible. A Pressure Implicit Split Operator (PISO) algorithm [28] was used to solve the Favre-filtered governing equations for mass and momentum in time and space. A second-order backward Euler implicit time marching scheme was used for all variables. For convection, fluxes were interpolated using the central difference scheme for momentum. The remaining scalars use a third order cubic discretization scheme for the divergence, laplacian, and gradients of the discretized equations and field values in physical space.

The computational domain, illustrated in figure 4.9, was discretized into approximately 800k, 1,200k and 2,000k cells for comparison. To illustrate the block distribution developed for this geometry a two dimensional slice along the plane of symmetry is shown in figure 4.10. Figure 4.10 is cut at a distance of $7.5d$ downstream of the nozzle for illustration. The outlet of the domain is located $38d$ downstream of the nozzle exit. Grading of the mesh cell size is used to refine the mesh resolution near the jet shear layer and along the interior walls of the nozzle.

A three dimensional image of the mesh in the nozzle region is shown in Figure 4.11. The top and front patches of the domain are removed in figure 4.11 to offer a view of the mesh progression from the outer boundaries to the jet region. The mesh consists of a main core with five surrounding blocks added to place the jet core in the correct offset location as the experimental apparatus. The geometric center of the enclosure is illustrated in figure 4.11 which shows the nozzle is symmetric with respect to the axial (X-axis) and span-wise directions (Z-axis), but offset in the vertical direction (Y-axis).

To determine the independence of the solution on the computational domain, a URANS simulation is run with identical conditions except the mesh is replaced. The URANS solution for each

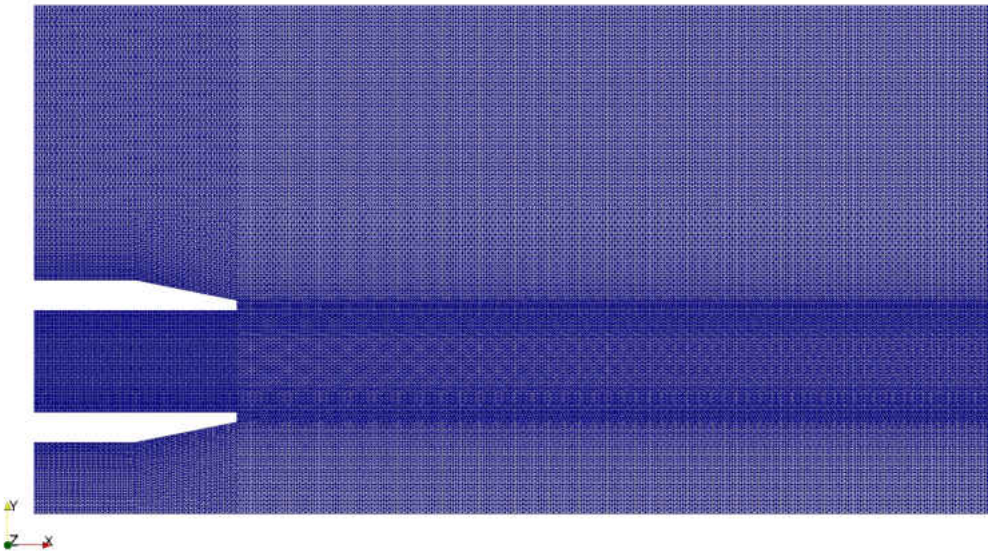

Figure 4.10: Two dimensional slice of the computational domain along the plane of symmetry.

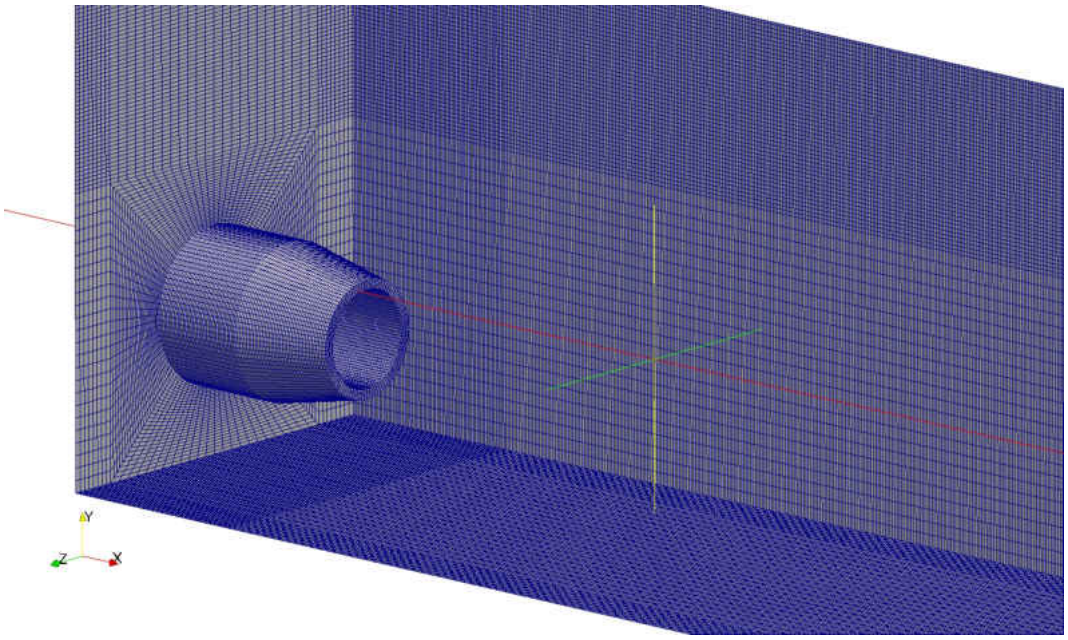

Figure 4.11: Three dimensional image of the computational domain near the jet nozzle.

mesh is initialized with the same steady RANS solution. The simulation is set to run for 5 flow passages. Based on quantitative comparisons of the mean velocity and temperature fields at 1, 2, 3 4 and 5 flow passages, the average difference in mean velocity fields was below the 2.3 m/s experimental uncertainty and the difference in mean temperature was below the 5% experimental uncertainty by the third flow passage. Since the change in mean velocity, with additional run time, was below the experimental uncertainty, the field is considered to have reached a statistically converged solution by the third flow through time. An additional two flow passages were included in the average to secure the converged solution. The temperature is chosen as the sensitivity variable since it is highly dependent on other fields values. Temperature is dependent on the velocity, RPV, variance and scalar dissipation fields. Comparisons of the mean temperature fields are plotted aside one another in figure 4.12. The solutions are similar except for the small changes in temperature along the shear layer of the reacting jet. To better quantify the difference in mean temperature among the three mesh's, line plots of the mean temperature are compared at a distance of $1d$ and $15d$ downstream of the nozzle along the plane of symmetry.

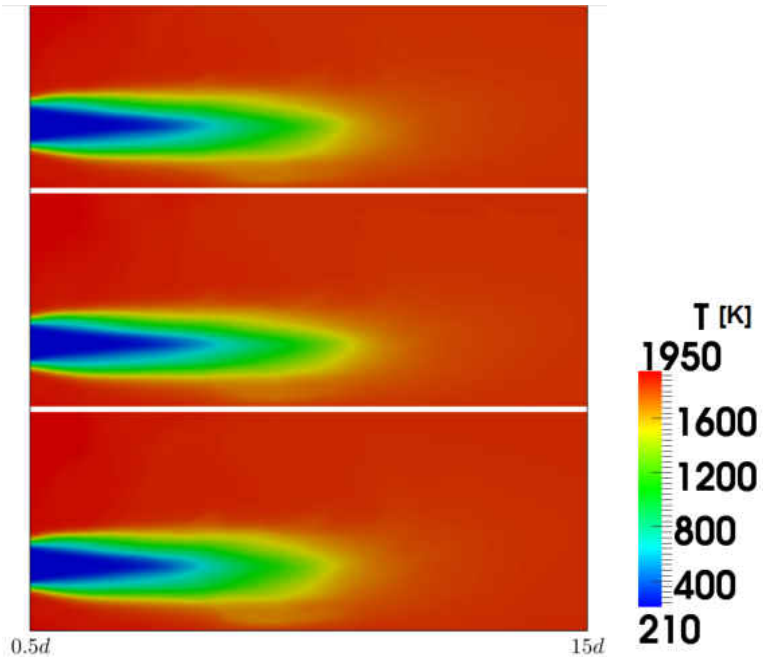

Figure 4.12: Comparisons of the mean temperature fields from the 800k cell mesh (top), 1200k cell mesh (middle) and 2000k cell mesh (bottom)

As seen in the temperate contours, differences between the three solutions are greatest along the shear layer. The largest percent difference in temperature, weighted by the total change in temperature ($T_{ad} - T_u$), among the three solutoins was equal to 4% at the $1d$ location and 2.3% at the $15d$ location. Since the differences between the three solutions are smaller then the experimental uncertainty in the temperature field (5%), the solution is deemed independent of the three mesh computational domains. Moreover, this same conclusion was found in a previous numerical study [52] and for this reason at 800k cells the mesh is considered independent of the solution. In the validation simulations, the 1,200k cell mesh is chosen in this work for its increased resolution of the small scale turbulent features. Each of the three mesh cases are prescribed different time steps of the order of a micro-second to determine the solution dependence on the temporal resolution. The 800k mesh uses a dynamic time step such that the Courant # would not exceed unity. For the case of the 1,200k and 2,000k cell meshes the max Courant # allowed is 0.8, respectively. Though the stability critiria for incompressible flow is a Courant # of unity, reduced values are used here to improve the numerical stability of the simulation. The same model constants (C_{c1} & C_{c2}) are used for each case, which suggests the two model constants are effectively independent of the grid resolution.

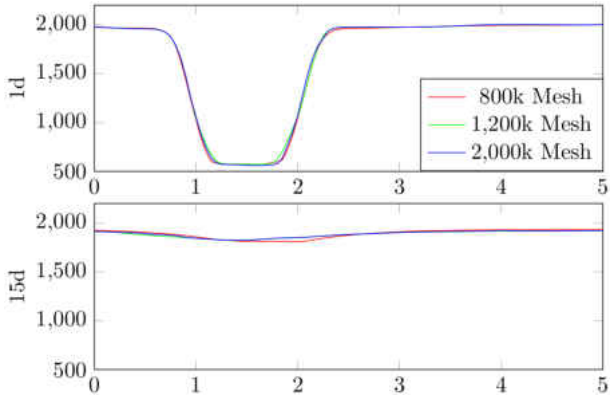

Figure 4.13: Comparisons of the mean temperature [K] at locations $1d$ and $15d$ away from the nozzle.

The mesh consists mostly of hexahedral (hex) cells, with the addition of a few tetrahedral (tet)

cells introduced at the interface between course and fine cell levels. Inserting tet cells above the height of the boundary layer allows for twice the cell refinement of the boundary layer. In conjunction with an expansion ratio of 1.2 near the wall, the mesh is able to sustain a Y+ values of $O(10)$ along the nozzle interior wall. The walls of the combustion chamber have a Y+$\approx$ 300 and employ wall functions for the turbulent kinetic energy and dissipation rate profiles within the boundary layer.

Three external boundaries are considered in this simulation; The inlet which is located 4d upstream, the outlet which is 38d downstream of the nozzle exit and the remaining walls of the enclosure which include the pipe walls inside the nozzle. The simulation occurs at atmospheric pressure and is prescribed this pressure at the outlet. All other scalar and vector quantities are imposed a zero-gradient condition at the outlet boundary. The pressure on the remaining walls and inlet is allowed to change and is imposed the pressure value from the interior cells adjacent to the boundaries, i.e. a zero gradient. The velocity profile at the inlet is made to be parabolic and was confirmed that the velocity profile matched the measurements at the nozzle exit and maintained the same mass flow rate. Random turbulent fluctuations are imposed on the inlet velocity profile at 10% about its mean velocity of 90 m/s. This turbulence intensity has been reported in previous numerical studies [21, 52] to provide excellent correspondence between measured and simulated velocity RMS profiles at the nozzle exit (4d downstream of the inlet). The inlet mixture equivalence ratio, Reynolds number, density and mass flow rate are equal to 0.7[-], 1.8x10^3[-], 0.5793[$\frac{kg}{m^3}$] and 4.2 [$\frac{g}{s}$], respectively.

Three distinct compressible LES models were used to model the SGS velocity fluctuations while the large scale "energy carrying" eddies are directly resolved, traditional of LES filtering. Results for the Spalart Allmaras (SA) [4], One Equation Eddy (OEE) viscosity [19] and the Smagorinksy models [66] were compared and the best model chosen for the prediction of the reactive scalars. The SA model is considered a hybrid-LES model, which actively switches between LES and URANS closure models depending on the magnitude of the turbulent length scale (l'). When l'

is large LES is used to better resolve regions with increased strain. The implemented Smagorinsky model is not dynamic in that the Smagorinsky constant, C_s, was held uniform over the domain and set equal to 0.21. The OEE viscosity model is similar in its implementation to the Smagorinsky model, except that a transport equation for the SGS turbulent kinetic energy is solved instead of an algebraic expression, as in the Smagorinsky model.

The length of the nozzle was sufficient enough (see Fig. 4.9) to allow the inlet values to adjust to the experimental profiles by the end of the nozzle. N, RPV, and its variance were set to zero at the inlet and set a zero gradient condition for the remaining walls and outlet. The inlet temperature is prescribed a fixed value of 573K, the remaining boundaries impose a zero gradient with temperature.

The simulation flow field is initialized by a converged RANS solution and then runs 'unsteady' for 5 flow passages through the entire domain. A single flow passages lasts 0.7 milliseconds. A quasi-steady state is again reached after 3 milliseconds (ms) of simulation time, at which point there still exist turbulent fluctuations but the flame length remains approximately constant. To quantify the steadiness of the flow field the RPV from every cell in the domain is included in a weighted average, where the RPV is weighted by its respective cell volume. The results for the volume weighted RPV are plotted against time for each mesh size in figure 4.14. When the weighted average of the RPV reaches a constant value, the flame can be considered to have reached steady burning conditions even in the presence of sustained turbulent fluctuations both in the jet and re-circulation zones. This calculation is performed at every time step and the transient results plotted in figure 4.9.

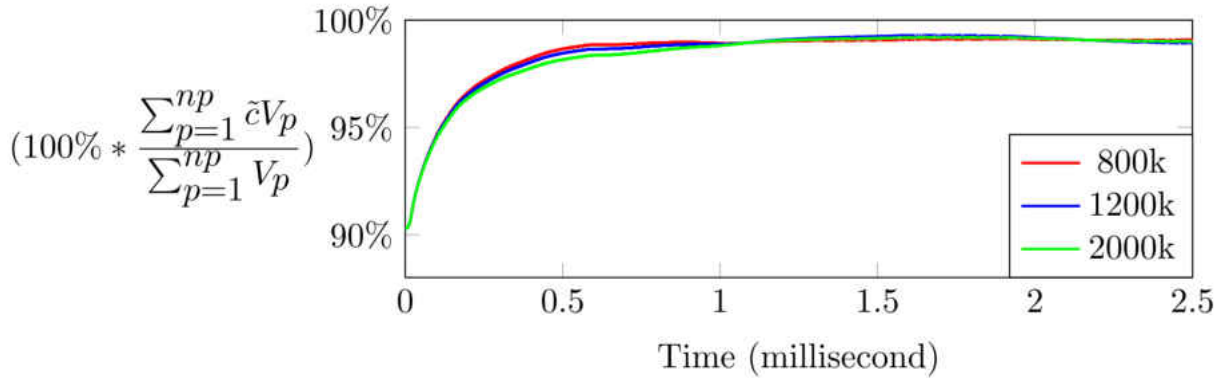

Figure 4.14: Volume weighted average RPV versus time.

Statistics are then taken, for the mean and root mean square (RMS), for an additional 35 ms. The simulation is run in parallel on sixteen Xeon E5650 hex-core processors for a total of 22 computational hours. The T-PCMC run time is approximately 10% higher than non-reactive simulations under the same flow conditions making it attractive for design purposes where low run times are desired with the inclusion of detailed chemistry in the combustion model.

4.3.3 Results and Analysis: Methane Flame

The T-PCMC LES combustion model is now validated against the experiments described in [35] on a single jet turbulent premixed lean methane flame. The presented results from the T-PCMC model are based on the 1,200k cell mesh. Velocity mean and RMS profiles are taken at 1d, 5d, 10d and 15d downstream of the nozzle exit, as shown in figure 4.9 for verification of the results.
Figure 4.15 compares the mean profiles of the predicted axial and radial velocity components to the PIV measured data at 4 planes 1, 5, 10 and 15 diameters downstream of the nozzle exit as illustrated in figure 4.9. The vertical axis is the velocity $[m/s]$ and the horizontal axis is the radial distance from the bottom wall scaled by the nozzle diameter ($\frac{y}{D}$). Overall the prediction of the axial and radial velocities, by the three LES models, provide a reasonable match with experimental results.

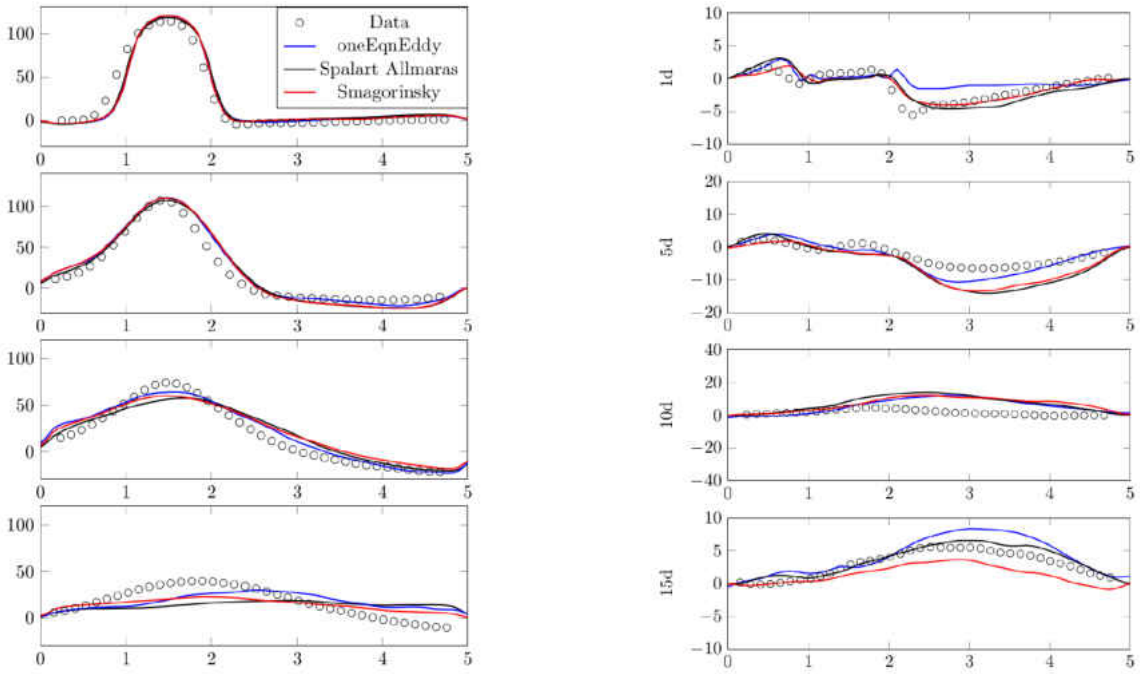

Figure 4.15: Mean Axial (left) and Radial (right) Velocity Profiles at four downstream locations ($x = 1d, 5d, 10d\&15d$)

Considering the axial velocity in figure 4.15, the maximum velocity is located slightly higher than the experimental data which means the predicted flame has a slightly higher upward deflection, which is dependent on the size of the re-circulation zone. The re-circulation zone ($Ux < 0$) is long and present along the top wall at all four axial locations. At the x=15D locations, LES predicts the re-circulation zone has terminated ($Ux > 0$), but is still present in the experimental data. It is worth noting that all prior numerical studies [21, 52] show the same offset of the axial and radial velocity profiles at the 1D location. The shear layer at the 1D location is particularly challenging to resolve and was largely over predicted by the OEE viscosity model. This region experiences large velocity gradients which may be improved upon with mesh refinement around the nozzle. The radial velocities are also well predicted but begin to show larger differences among the three LES models, in comparison to the small differences found in the axial velocity. Predictions are good at the lower heights (0-2mm) and then begin to over and under predict the radial velocity component near the upper wall. Aside from small discrepancies, the SA model seemed

to best predict the trends and magnitude of the velocity field and accordingly is the chosen LES turbulence model for species predictions with the T-PCMC model.

Figure 4.16 shows the axial velocity RMS profiles at the same four locations downstream of the nozzle.The measured RMS trends are well predicted. Larger values for RMS are predicted which indicate a higher total enthalpy would be appropriate since there is more kinetic energy in the predicted results. The good match the the velocity RMS at the $1d$ location indicates that an appropriate turbulence intensity was used at the velocity inlet condition. Based on the performance of the three models in figures 4.15 and 4.16, the SA model best predicts the time averaged and fluctuations of the velocity field. For this reason the remaining results of the species mass fractions are presented solely with the SA LES model.

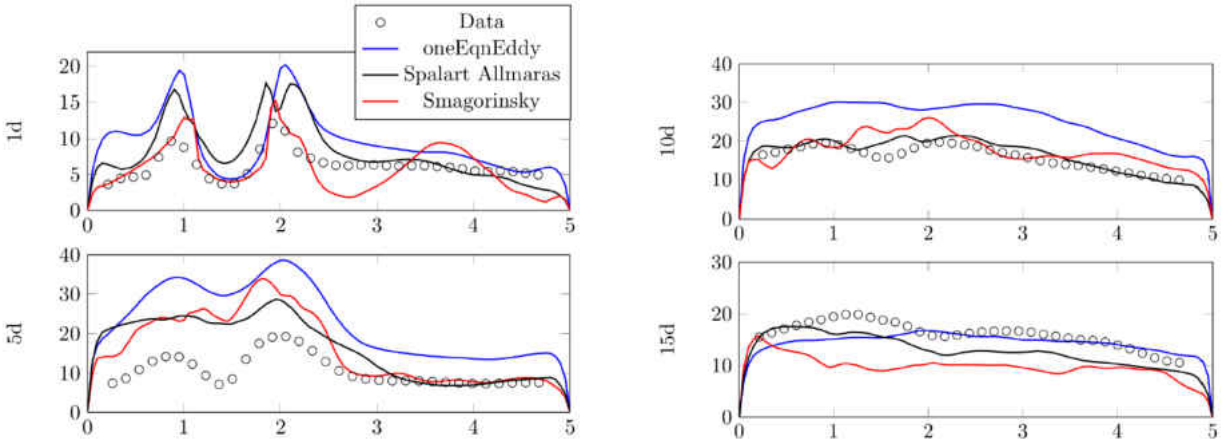

Figure 4.16: Root Mean Square of Axial Velocity at four downstream locations ($x = 1d, 5d, 10d\&15d$)

To qualitatively show the improved prediction of the NA-T-PCMC model in comparison to the adiabatic results (A-T-PCMC), contour plots of the mean CH_4 and mean CO_2 fields are compared against one another. Figure 4.17 shows the elongation of the unburnt methane in the flame, this is due to the reduction of the RPV source term due to to heat loss. Notice that much like in figure 3.17 the extension of CH_4 and CO_2 occurs near the burnt conditions. This is in agreement with the maximum S_c values that occur at high values of c as in figure 3.17.

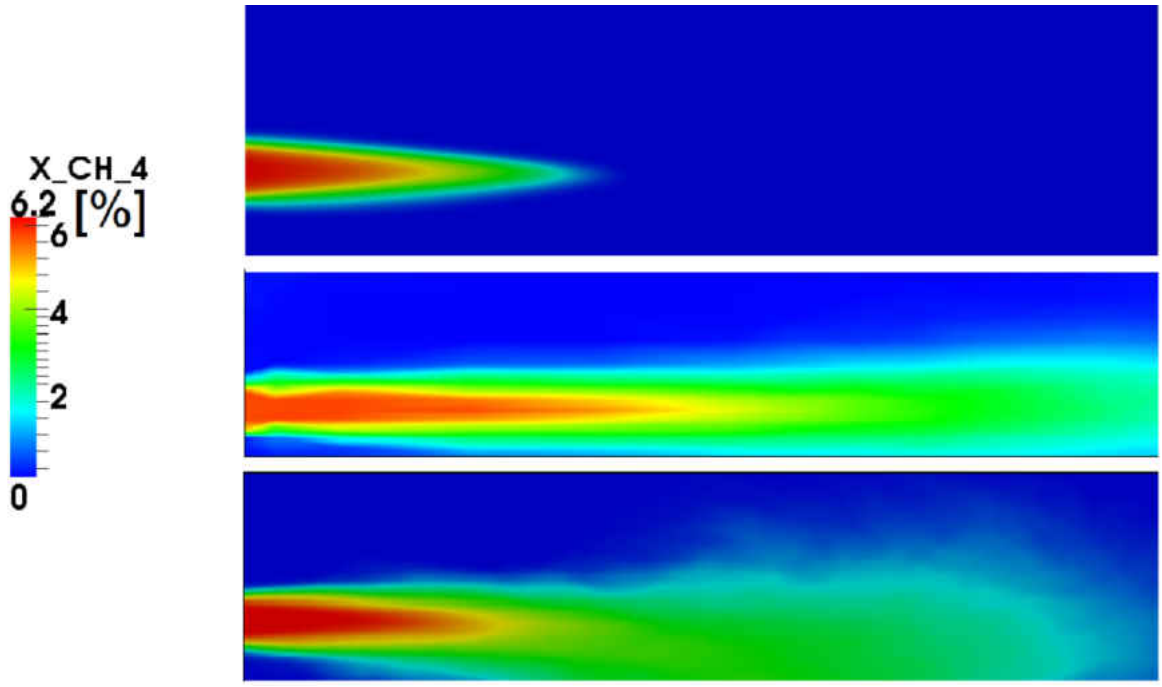

Figure 4.17: Dry CH_4 Mole Fraction [-]: Adiabatic T-PCMC (top), Measured (middle), Non-Adiabatic T-PCMC (bottom)

Figures 4.17 and 4.18 show a similar behavior and indicate that the RPV source term may still be over-predicted by the NA-T-PCMC model which would explain why the flame length is under-predicted when compared to the measured results.

To provide a quantitative comparison of the adiabatic, non-adiabatic and measured results, line plots are provided at three axial locations ($x = 2d, 7d, 10d$) downstream of the nozzle. Figure 4.19 shows the mean temperature (left) and RMS temperature (right) profiles at the three axial locations. Here it is evident the enhanced prediction of the temperature field, specifically at the downstream locations.

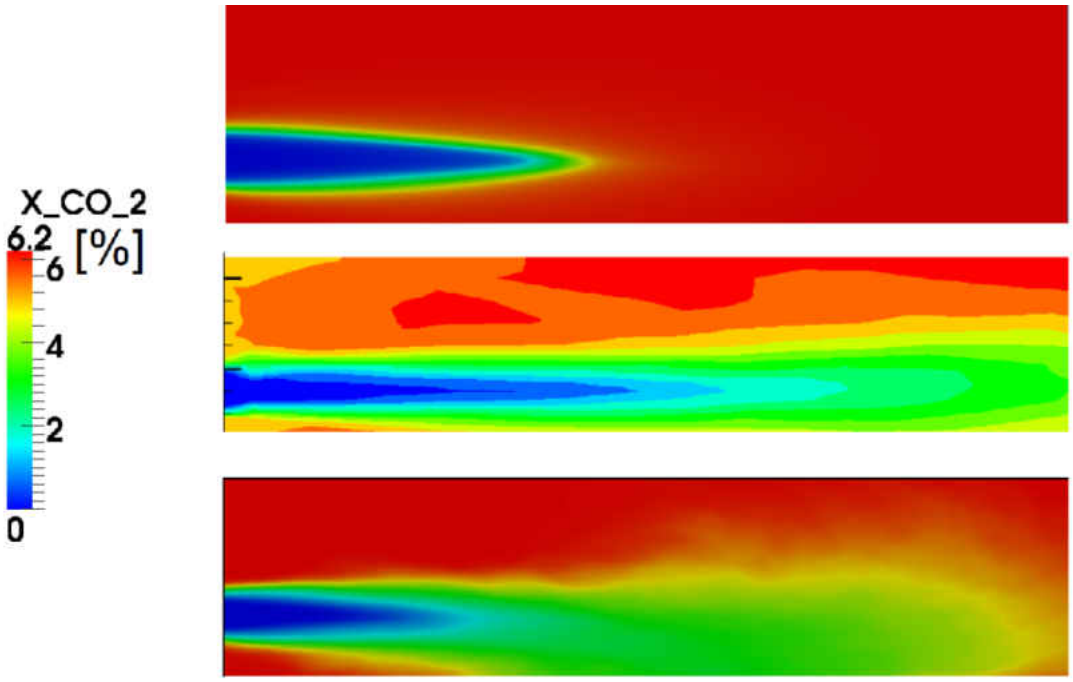

Figure 4.18: Dry CO_2 Mole Fraction [-]: Adiabatic T-PCMC (top), Measured (middle), Non-Adiabatic T-PCMC (bottom)

Where the adiabatic model has reach a near uniform temperature profile at the x=10d location, the non-adiabatic solution predicts the spatial dependence of temperature ranging several 100K. The temperature RMS, on the right of figure 4.19, shows more similarity between the two models, but again the NA-T-PCMC model better predicts the downstream values in comparison to the A-T-PCMC results.

Figure 4.20 shows line plots of the mean dry CH_4 (left) and CO_2 (right) mole fractions. The NA-T-PCMC model better predicts the extension of CH_4's downstream of the nozzle and shows the improved prediction of harmful emissions such as unburnt hydrocarbons when compared to the results from the A-T-PCMC simulation.

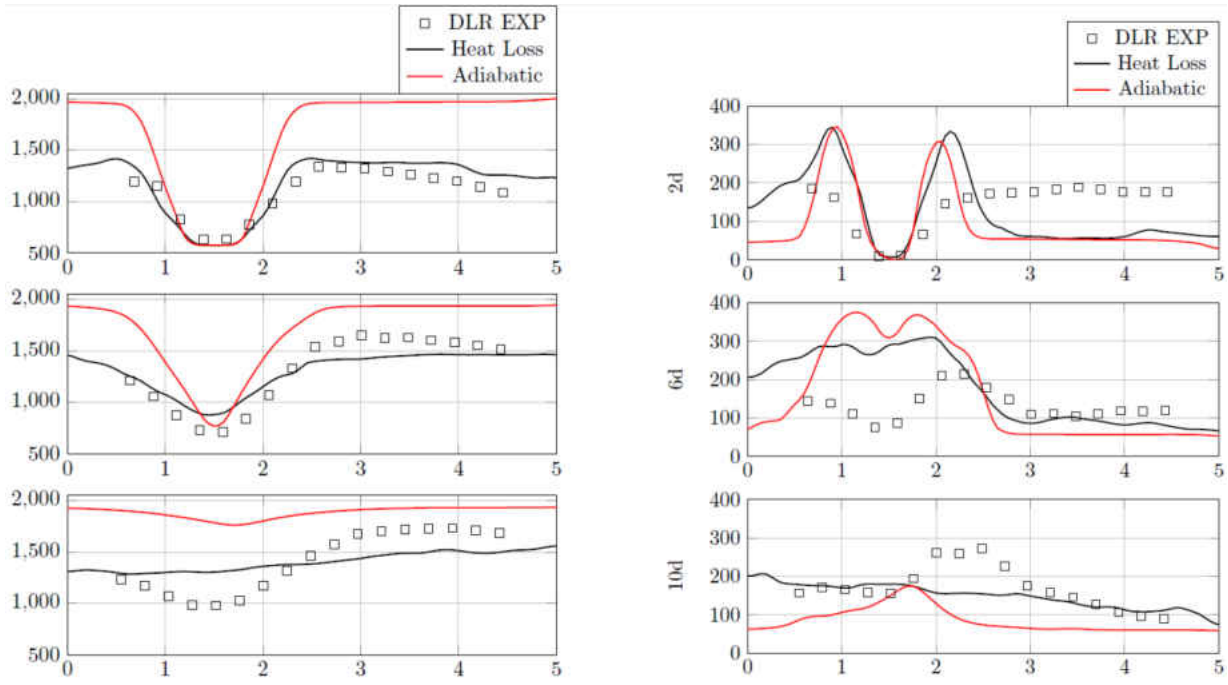

Figure 4.19: Mean Temperature [K] at three downstream locations ($x = 2d, 7d\&10d$)

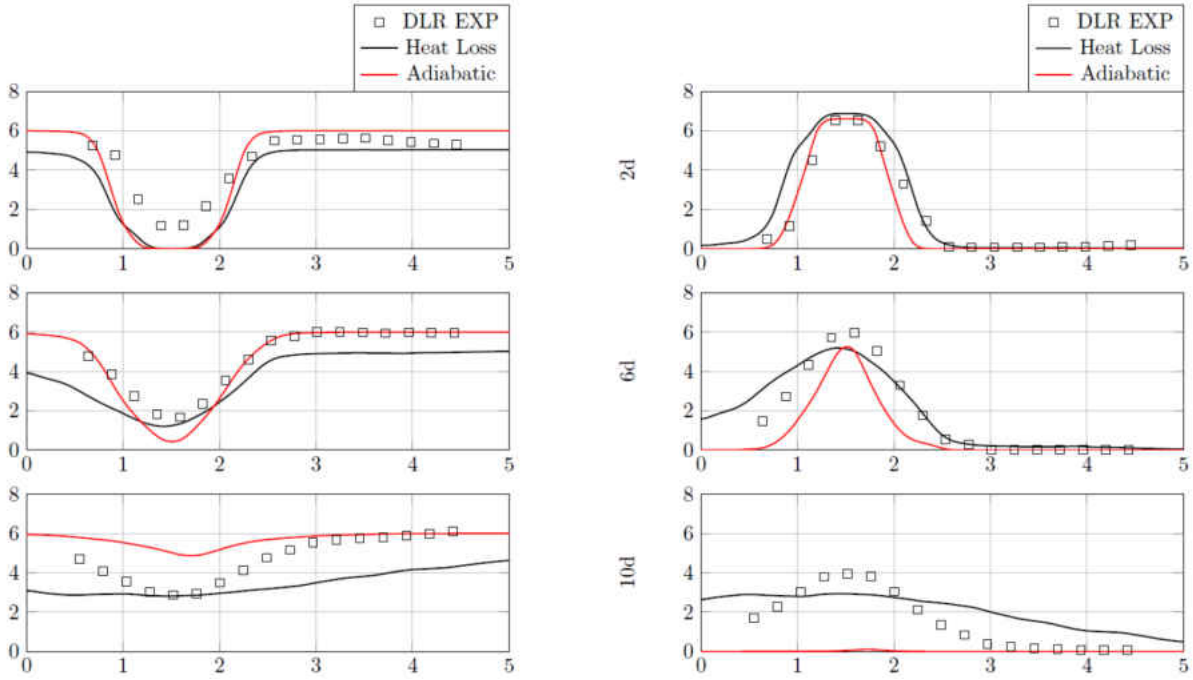

Figure 4.20: Mean Dry CH_4 (Left) & CO_2 (Right) Mass Fraction [-] at three downstream locations ($x = 2d, 7d\&10d$)

4.3.4 Results and Analysis: Hydrogen Flame

A similar experimental data set is provided by the DLR research group for a lean Hydrogen (H_2) flame. The H_2 flame has an equivalence ratio of 0.71. The flame is preheated to 573K at atmospheric pressure as in the Methane flame and has the same velocity boundary conditions and similar Reynolds numbers. Note that outside of changing the inlet species concentrations all model parameters, governing equations and assumptions are the same as in the Methane flame. This demonstrates the validity of the T-PCMC model assumptions non-unity Lewis # fuels. This H_2 mixture is expected to have a Lewis # of approximately 0.8.

Figure 4.21 shows the mean dry H_2 mole fraction contours for the measured and experimental results. Note that all contour plots are presented under identical ranges as the measured results. The H_2 predictions are in overall good agreement with the experimental data. Although the length of the flame and lowest H_2 concentrations are well predicted, the highest H_2 concentrations in the unburnt region are over predicted in the T-PCMC results. This indicates the T-PCMC model predicts a thinner flame which would be caused by an over-prediction of the RPV source term. Since the burnt conditions are well predicted, the sum of the source term must be well predicted since the lowest H_2 contours, at the tip of the flame, are in agreement with experimental results.

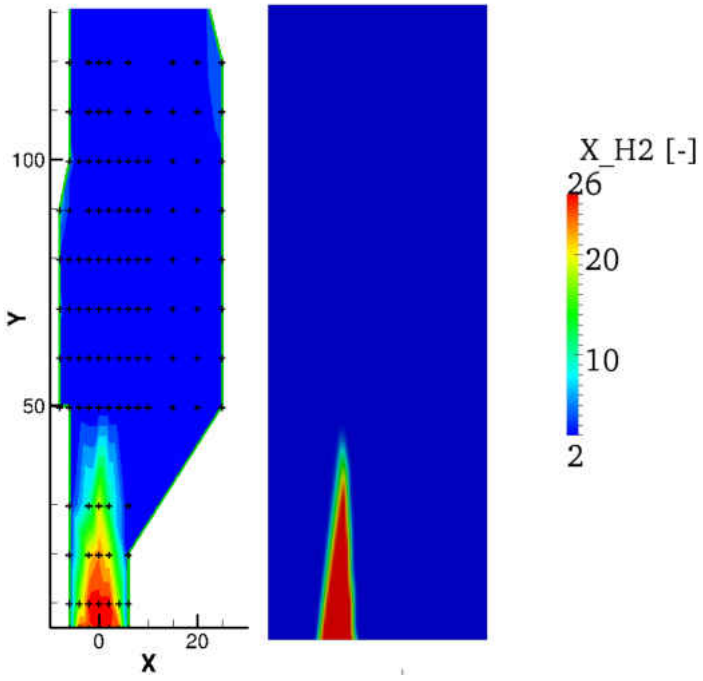

Figure 4.21: Mean Dry H_2 Mole Fraction [-] Contours: Experimental (Left) and T-PCMC (Right)

Comparing the line plots of the mean dry, H_2 mole fractions at distances 2d, 7d and 10d downstream from the nozzle, the over prediction of unburnt H_2 is more evident, as shown in Figure 4.22. The measured data may be too course at the $6d$ location to accurately capture the jet profile.

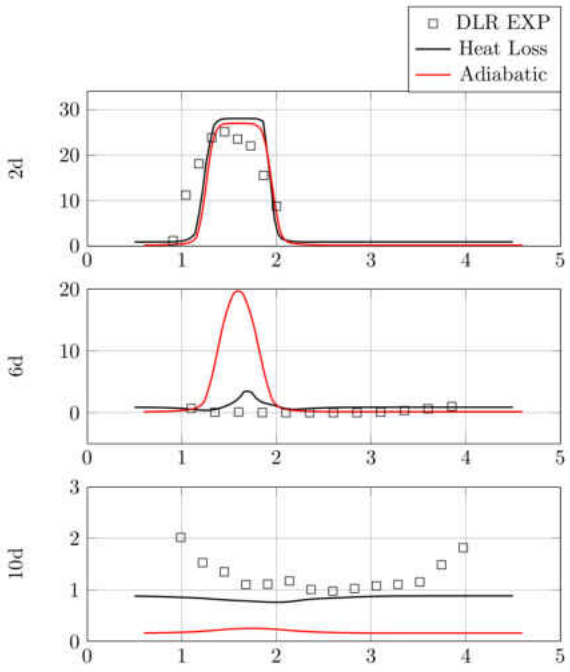

Figure 4.22: Mean Dry H_2 Mass Fraction [-] at three downstream locations ($x = 2d, 7d\&10d$)

To compare the transient predictive capability of the T-PCMC model, root mean square quantities are compared. Shown below in figure 4.23 is the RMS contour of the Dry H_2 mole fractions. The T-PCMC model over-predicts slightly the H_2 RMS profiles, but the location of the max variance is well predicted near the tip of the flame. The experimental results show a near symmetric distribution of the variance near the flame tip, where the T-PCMC model shows the bottom portion of the flame producing the majority of the variance.

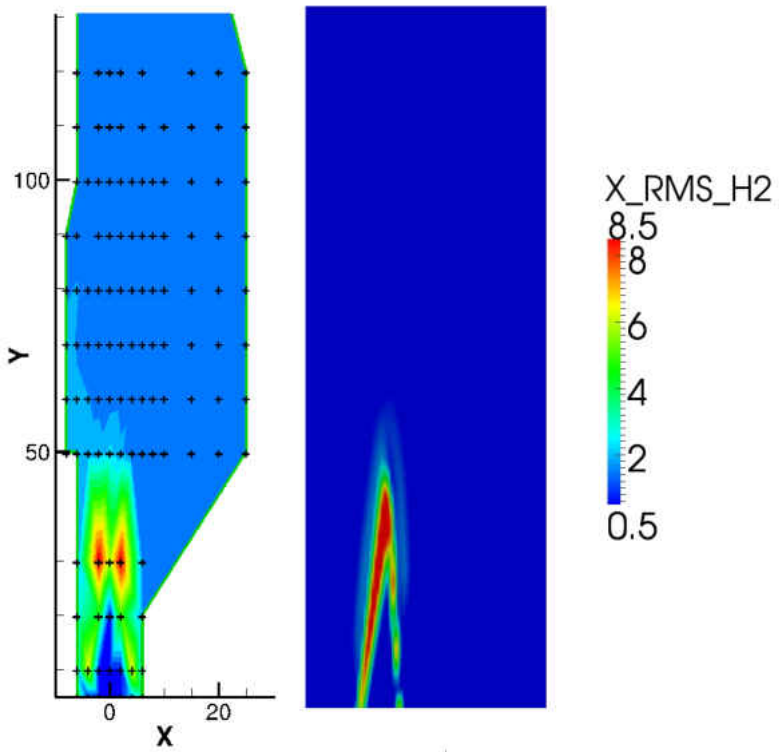

Figure 4.23: Root Mean Square Dry H_2 Mole Fraction [-] Contours: Experimental (Left) and T-PCMC (Right)

Almost identical discrepancies between RMS quantities are found when comparing the temperature RMS in figure 4.24. Predictions of the temperature RMS shows a good match in the reaction region and downstream of the reaction. Since the H_2 flame is stationary when compared to the CH_4 flame, it is expected that RMS quantities do not change significantly directly outside of the flame. Both experimental and predicted results indicate a reduction in the RMS directly after the flame, followed by an increase in the RMS due to changes in the total enthalpy, in the burnt products, past the reaction zone.

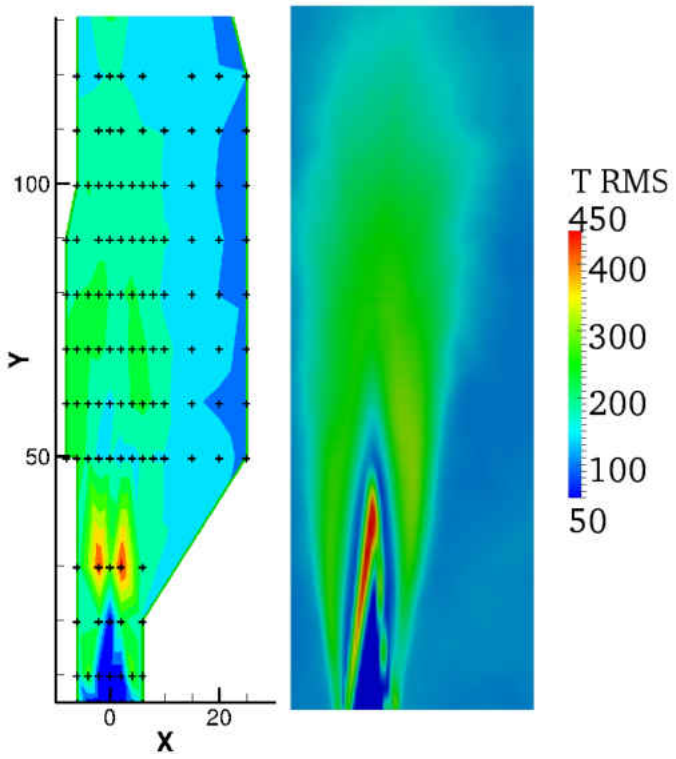

Figure 4.24: Root Mean Square Temperature [K] Contours: Experimental (Left) and T-PCMC (Right)

Mean temperature line plots at distances 2d, 6d and 10d downstream of the nozzle are provided below in figure 4.25. Though the measurement domain is small at the $x = 2d$ location it can be seen that the unburnt temperature is well predicted although the T-PCMC model predicts a thinner temperature profile which is agreement with the under-prediction of flame thickness seen in figure 4.22. Downstream predictions of the temperature field are fair, but the T-PCMC model predicts a more distributed temperature profile when compared to the experimental results which show large gradients in the mean temperature field at the downstream locations.

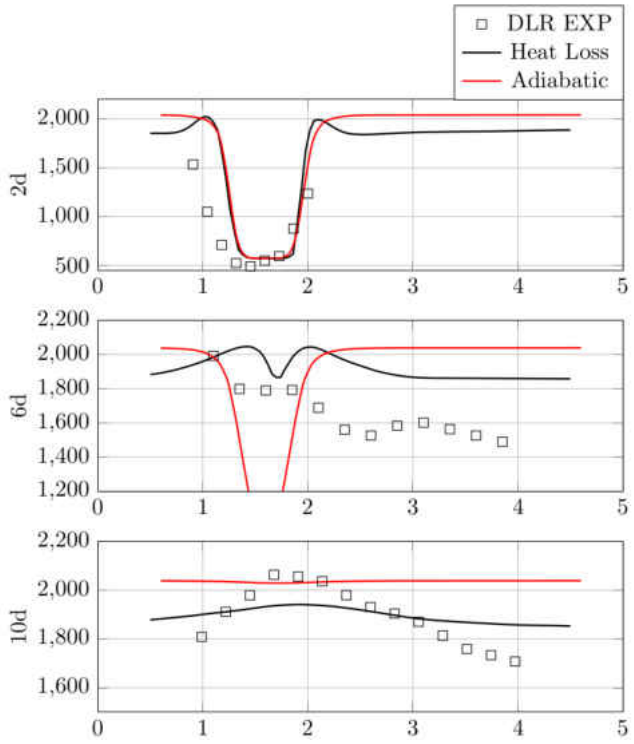

Figure 4.25: Mean Temperature [K] at three downstream locations ($x = 2d, 7d\&10d$)

CHAPTER 5: CONCLUSIONS

In this PhD dissertation a newly developed low run time premixed combustion model is proposed, developed and validated against experimental data sets.This combustion model uses detailed kinetics information from the GRI3.0 kinetic mechanism to give a detailed representation of the chemical state of the flame. The effect of large scale turbulence on the reaction rates is accounted for by using a presumed shape PDF, similar to other table lookup models. The effect of small scale turbulence is directly accounted for by the scalar dissipation in the T-PCMC governing equation. Additionally, a chemical and thermodynamic representation of the mean reaction rate term is obtained using a CMC first order closure for the mean chemical reaction rate. In addition, the T-PCMC model is derived in a Large Eddy Simulation framework and the effects of heat loss are accounted for inside and outside of the reaction zone. The proposed heat loss model has shown the ability to alter the mean reaction rate and species transport within the flame. The non-adiabatic T-PCMC model provides a better prediction of the mixture species concentrations, temperature field and over all flame shape when compared to the adiabatic T-PCMC results. The Tabulated Premixed Conditional Moment Closure (T-PCMC) turbulent combustion model was coupled to the open source CFD program OpenFOAM and used to model an enclosed, reacting jet from DLR experimental data [35] and a backward facing step reacting methane jet [24].

The results of this work show the promise of the tabulated premixed CMC model with Large Eddy Simulations to predict the velocity and scalar fields of an idealized LPM gas turbine combustor with detailed chemistry, heat loss and low run times which warrants further development.

Listed below are the completed research objectives.

1. The T-PCMC model has been extended to account for Large Eddy Simulations and the effect of heat loss on the reacting mixture.

2. The proposed LES and Heat loss implementation of the T-PCMC model has been compared against two enclosed, turbulent premixed flame experimental data sets with Methane ($Le\# = 1$) and Hydrogen reactions ($Le\# < 1$).

3. A Heat Loss model has been developed to account for the effects of heat loss in both RPV space and real space for the burnt mixture while maintaining a low run time.

4. The extended T-PCMC model has demonstrated the ability to predict major and minor species, with the inclusion of heat loss, which warrants further research and development.

Listed below are objectives for future research work and development of the T-PCMC model.

1. Tabulate the T-PCMC solution to the unsteady T-PCMC equation.

2. Add enthalpy as a fourth dimension for all conditioned species.

3. Add the conditional velocity to the T-PCMC equation to be solved offline.

4. Determine the range of applicability in using a conserved PDF on a reactive mean and variance.

5. Improve closure for conditioned scalar dissipation rate based on DNS data for the case of $c > 1$

Listed below is the presentations and publications from this dissertation work

1. Poster presentation of adiabatic LES results on DLR flame at the 35th International Combustion Symposium, San Francisco, CA- 2014. Description: LES of the Adiabatic T-PCMC of a CH_4 single jet flame from DLR.

2. Published and Presented at the 53rd Aerospace Sciences Meeting (AIAA SciTech 2015), Kissimmee, FL. Paper No: AIAA 2015-0419. Description: URANS of the Adiabatic T-PCMC of a CH_4 methane BFS from El-Benhawy.

3. Published and Presented at the ASME TurboExpo, Montreal 2015. Paper No: GT2015-43788 Description: LES of the Adiabatic T-PCMC of a CH_4 methane BFS from El-Benhawy.

Listed below are the submitted Adiabatic Journal Papers

1. Journal of Propulsion and Power (Revised Paper Under Review, 6/2015). Description: LES of the Adiabatic T-PCMC of a CH_4 methane BFS from El-Benhawy.

2. Combustion Theory and Modeling (Under Review, 7/2015). LES of the Adiabatic T-PCMC of a CH_4 single jet flame from DLR.

3. ASME Journal of Engineering for Gas Turbines and Power (Under Consideration, 7/2015). Description: URANS of the Adiabatic T-PCMC of a CH_4 methane BFS from El-Benhawy.

Listed below are the Non Adiabatic Journal Papers (planned submission- next two months)

1. Combustion and Flame: Tabulated Premixed CMC Predictions of a Turbulent Premixed Methane Flame with Heat Loss.

2. Combustion Symposium: Tabulated Premixed CMC Predictions of a Methane Three Jet Turbulent Premixed Hydrogen Flame with the inclusion of Heat Loss.

3. Journal of Hydrogen Technology: Tabulated Premixed CMC Predictions of a Turbulent Premixed Hydrogen Flame with Heat Loss.

LIST OF REFERENCES

[1] Environmental Protection Agency. The clean air act amendments of 1990, 1990.

[2] S. Amzin. *Conditional Moment Closure Method for Turbulent Premixed Flames*. PhD thesis, Cambridge University, 2012.

[3] S. Amzin, N. Swaminathan, J.W. Rogerson, and J.H. Kent. Conditional moment closure for turbulent premixed flames. *Combustion Science and Technology*, 184(10-11):1743–1767, 2012.

[4] G. Ashford. *An Unstructured Grid Generation and Adaptive Solution Technique for High Reynolds Number Compressible Flows*. PhD thesis, University of Michigan, 1996.

[5] R. W Bilger. Future progress in turbulent combustion research. *Progress in energy and combustion science*, 26.4:367–380, 2000.

[6] R. W. Bilger, S. B. Pope, K. N. Bray, and J.F. Driscoll. Paradigms in turbulent combustion research. *Proc. Combust. Inst*, 30:21–42, 2005.

[7] Michele Bolla, Y. Wright, K. Boulouchos, G. Borghesi, and E. Mastorakos. Soot formation modeling of n-heptane sprays under diesel engine conditions using the conditional moment closure approach. *Combustion Science and Technology*, 185:5:766–793, 2013.

[8] K. Bray. The interaction between turbulence and combustion. *Combust. Inst.*, 171:223–233, 1979.

[9] K. Bray. Turbulent transport in flames. *Math. Phys. Sci.*, 451:231–256, 1995.

[10] K. Bray, M. Champion, and P. Libby. Premixed flames in stagnating turbulence part iv: A new theory for the reynolds stresses and reynolds fluxes applied to impinging flows. *Combust. Flame*, 120:1–18, 2000.

[11] K. Bray, P. Libby, G. Masuya, and J. Moss. Turbulence production in premixed turbulent flames. *Combust. Sci. Tech.*, 25:127–140, 1981.

[12] K. Bray, P. A. Libby, and J. B. Moss. Flamelet crossing frequencies and mean reaction rates in premixed turbulent combustion. *Combust. Sci. Tech*, 41:143–172, 1984.

[13] K. Bray, D Veynante, A. Trouve, and T. Mantel. Gradient and counter-gradient scalar transport in turbulent premixed flames. *J. Fluid Mech.*, 332:263–293, 1997.

[14] KNC. Bray, PA. Libby, and JB. Moss. Unified modeling approach for premixed turbulent combustionpart i : General formulation. *Combustion and flame*, 61.1:87–102, 1985.

[15] S. Candel and T Poinsot. Flame stretch and the balance equation for the flame area. *Combust. Sci. Tech.*, 70:1–15, 1990.

[16] J. R. Cash and F. Mazzia. A new mesh selection algorithm, based on conditioning, for two-point boundary value codes. *Journal Comput. Appl. Math*, 184(2):362–381, 2005.

[17] R.K. Cheng and I.G. Sheperd. The influence of burner geometry on premixed turbulent flame propagation. *Combust. Flame*, 85:7–26, 1991.

[18] M. J. Cleary, J. H. Kent, and R. W. Bilger. Prediction of carbon monoxide in fires by conditional moment closure. *Proc. Combust. Inst.*, 29:273–279, 2002.

[19] E. De Villiers. *The Potential of Large Eddy Simulation for the Modeling of Wall Bounded Flows*. PhD thesis, Thermofluids Section Department of Mechanical Engineering Imperial College of Science, Technology and Medicine, 2006.

[20] C. B. Devaud, R.W. Bilger, and Liu T. A new method of modeling the conditional scalar dissipation rate. *Physics of Fluids*, 16(6), 2004.

[21] M. Di Domenico, C.H. Beck, O. Lammel, Krebs.W, and B.E. Noll. Experimental and numerical investigation of turbulent, lean, high-strained, confined, jet flames. In *49th AIAA Aerospace Sciences Meeting*, 2011.

[22] A. Donnini, S. Martin, R.J.M. Bastiaans, J.A. van Oijen, and L.P.H de Goey. Numerical simulations of a premixed turbulent confined jet flame using the flamelet generated manifold approach with heat loss inclusion. In *Proceedings of ASME TurboExpo 2013*, 2013.

[23] J Driscoll. Turbulent premixed combustion: Flamelet structure and its effect on turbulent burning velocities. *Progress in Energy and Combustion Science*, 34:91134, 2008.

[24] Y El Banhawy, S Sivasegaram, and J.H. Whitelaw. Premixed, turbulent combustion of a sudden-expansion flow. *Combustion and Flame*, 50, 1983.

[25] B. Fiorina, O. Gicquel, L. Vervisch, S. Carpentier, and N. Darabiha. Approximating the chemical structure of partially premixed and diffusion counterflow flames using fpi flamelet tabulation. *Combustion and flame*, 140(3):147–160, 2005.

[26] A. Gamory and E Mastorakos. Sensitivity analysis of les-cmc predictions of piloted jet flames. *Int. Journal of Heat and Fluid Flow*, 39:53–63, 2013.

[27] A. Garmory and E. Mastorakos. Capturing localised extinction in sandia flame f with lescmc. *Proceedings of the Combustion Institute,*, 33(1):1673–1680, 2011.

[28] H. Jasak, A. Jemcov, and Z. Tukovic. Openfoam: A c++ library for complex physics simulation. In *International Workshop on Coupled Methods in Numerical Dynamics*, 2007.

[29] C. Jimenex, F. Ducros, and B. Bedat. Subgrid scale variance and dissipation of a scalar field in large eddy simulations. *Phys. Fluids*, 13:1748, 2001.

[30] S. I. Kim and E. Mastorakos. Simulations of turbulent lifted jet flames with two-dimensional conditional moment closure. *Proc. Combust. Inst.*, 11:911–918, 2005.

[31] A. Klimenko. On the relation between the conditional moment closure and unsteady flamelets. *Combustion Theory and Modelling*, 5(3):275–294, 2001.

[32] A. Klimenko and R.W. Bilger. Conditional moment closure for turbulent combustion. *Progress in energy and combustion science*, 25.6:595–687, 1999.

[33] A.Y. Klimenko. Multicomponent diffusion of various admixtures in turbulent flow. *Fluid Dynamics*, 25:327–334, 1990.

[34] E Knudsen, E. S Richardson, E. M. Doran, H. Pitsch, and J. H. Chen. Modeling scalar dissipation and scalar variance in large eddy simulation: Algebraic and transport equation closures. *Physics of Fluids*, 24, 055103, 2012.

[35] O. Lammel, M. Stohr, P. Kutne, C. Dem, W. Meier, and M. Aigner. Experimental analysis of confined jet flames by laser measurement techniques. *Journal of Engineering for Gas Turbines and Power*, 134.4:041506, 2012.

[36] C.N. Lane. *Acid Rain: Overview and Abstracts*. Nova Science Publisher, New York USA, 2003.

[37] R. P. Lindstedt and E. M. Vaos. Transported pdf modeling of high- reynolds number premixed turbulent flames. *Combust. Flame*, 145:495–511, 2006.

[38] S. Martin. *The Conditional Moment Closure Method for Modeling Lean Premixed Turbulent Combustion*. PhD thesis, The University of Washington, 2003.

[39] S. Martin, A. Jemcov, and B. de Ruijter. Modeling an enclosed, turbulent reacting methane jet with the premixed conditional moment closure method. In *Proceedings of the ASME Turbo Expo*, number GT2013-95092, 2013.

[40] S. Martin, J. C. Kramlich, G. Kosaly, and J.J. Riley. The premixed conditional moment closure method. *Journal of Engineering for Gas Turbines and Power*, 125:895–900, 2003.

[41] S. M. Martin. *The Conditional Moment Closure Method for Modeling Lean Premixed Turbulent Combustion*. PhD thesis, The University of Washington, 2003.

[42] E. Mastorakos. *Turbulent Combustion Modeling: Advances, new trends, and perspectives*. Springer, New York, USA, 2010.

[43] E. Mastorakos and R.S. Cant. *An introduction to turbulent reacting flows*. Imperial College Press, London, UK, 2008.

[44] C. Meneveau and T. Lund. The dynamic smagorinsky model and scale-dependent coefficients in the viscous range of turbulence. *Physics of fluids*, 9:302–342, 1997.

[45] F. R. Menter. Improved two-equation k-omega turbulence models for aerodynamic flows . Technical report, NASA STI/Recon Technical Report N 93 :22809, 1992.

[46] S. Navarro-Martinez and A. Kronenburg. Lescmc simulations of a lifted methane flame. *Proceedings of Combustion Institute*, 32:1509–1516, 2009.

[47] H. Pitsch. Large-eddy simulation of turbulent combustion. *Annual Rev. Fluid. Mech.*, 38:453–482, 2006.

[48] T. Poinsot. *Theoretical and Numerical Combustion*. , West view Press, Philadelphi, USA, 2005.

[49] Thierry Poinsot and Denis Veynante. *Theoretical and numerical combustion*. 2005.

[50] S. B. Pope. Pdf methods for turbulent reactive flows. *Prog. Energy Com- bust. Sci.*, 112:119–192, 1985.

[51] S. B Pope. *Turbulent Flows*. Cambridge University Press, Cambridge, UK, 2000.

[52] F. Proch and A. M. Kempf. Modeling heat loss effects in the large eddy simulation of a model gas turbine combustor with premixed flamelet generated manifolds. *Proceedings of the Combustion Institute*, Unpublished Article, 2014.

[53] V. D. Sarli, A. D. Benedetto, and G. Russo. Sub-grid scale combustion models for large eddy simulation of unsteady premixed flame propagation around obstacles. *Jrnl. Hazardous Materials*, 180:71–78, 2010.

[54] G. Smith, D. Golder, M. Frenklach, N. Moriarty, B. Eiteneer, B. Goldenberg, C. Bowmann, R. Hanson, S. Song, and Z. Qin. Grimech 3.0 reaction mechanism.

[55] N. S. Smith. *Development of the Conditional Moment Closure Method for Modelling Turbulent Combustion*. PhD thesis, The University of Sydney, 1994.

[56] D. B. Spalding. Mixing and chemical reaction in steady confined turbulent flames. *Proc. Combust. Inst*, 13:649–657, 1970.

[57] I. Stankovic, A. Triantafyllidis, E. Mastorakos, C. Lacor, and B. Merci. Simulation of hydrogen auto-ignition in a turbulent co-flow of heated air with les and cmc approach. 86, 689710 (2011). *Flow Turb. Combust.*, 86:689–710, 2011.

[58] R. Steele. *NOx and N2O Formation in Lean Premixed Jet Stirred Reactors Operated from 1 to 7 atm*. PhD thesis, University of Washington., 1995.

[59] N. Swaminathan and R. W. Bilger. Analysis of conditional moment closure for turbulent premixed flames. *Combust. Theory modeling*, 5:241–260, 2001.

[60] N. Swaminathan, R. W. Bilger, and B. Cuenot. Relationship between turbulent scalar flux and conditional dilatation in premixed flames with complex chemistry. *Combust. Flame*, 1264:1764–1779, 2001.

[61] B Thornber, R. W Bilger, A. R. Masri, and E. R. Hawkes. An algorithm for les of premixed compressible flows using the conditional moment closure model. *Journal of Computational Physics*, 230(20):7687–7705, 2011.

[62] A. Triantafyllidis, E. Mastorakos, and R.L. Eggels. Large eddy simulations of forced ignition of a non-premixed bluff-body methane flame with cmc. *Combustion and Flame*, 156(12):2328–2345, 2009.

[63] A. Trouve and T. Poinsot. The evolution equation for the flame surface density. *J. Fluid Mech.*, 278:1–31, 1994.

[64] C. A. Velez, S. Martin, A. Jemcov, and S. Vasu. Les simulation of an enclosed turbulent reacting methane jet with the tabulated premixed cmc method. In *ASME TurboExpo*, 2015.

[65] J. Villermaux and F. Laurent. A generalized mixing model for initial contacting of reactive fluids. *Chemical Engineering Science*, 49.24:5127–5140., 1994.

[66] B. Vreman, B. Geurts, and H. Kuerten. Subgrid-modelling in les of compressible flow. *Applied scientific research*, 54(3):191–203, 1995.

[67] J. Warnatz, U. Maas, and R.W. Dibble. *Combustion physical and chemical fundamentals, modeling and simulation, experiments and pollutant formation*. Springer, New York, USA, 2006.

[68] H.G Weller, G. Tabor, H. Jasak, and C. Fureby. A tensorial approach to computational continuum mechanics using object oriented techniques. *Computers in Physics*, 12(6):620–631, 1998.

[69] F. A. Williams. *Turbulent combustion*. Society for Industrial and Applied Mathematics (SIAM), Philadelphia, USA, 1985.

[70] G. M. Woodwell, R. A. Houghton, and N. R. Tempel. Atmospheric co2 at brookhaven, long island, new york: Patterns of variation up to 125 meters. *Journal of Geophysical Research*, 78:932–940, 1973.

[71] K. Boulouchos Y. M. Wright, G. De Paola and E. Mastorakos. Simulations of spray autoignition and flame establishment with two-dimensional cmc. *Combust. Flame*, 1432:402 – 419, 2005.

[72] Y. Yunardi, R. M. Woolley, and M. Fairweather. Conditional moment closure prediction of soot formation in turbulent non-premixed ethylene flames. *Combust. Flame*, 152:360–376, 2008.

[73] V. Zimont, W. Polifke, M. Bettelini, and W. Weisenstein. An efficient computational model for lean premixed turbulent combustion at high reynolds number based on a turbulent flame speed closure. *Journal of Engineering for Gas Turbines and Power*, 120:526–532, 1998.